

POLITECNICO DI TORINO

Corso di Laurea Magistrale in Ingegneria Energetica e Nucleare

Tesi di Laurea Magistrale

SIMULATION ANALYSIS OF A GAS-TO-LIQUIDS PROCESS BASED ON CO₂/STEAM REFORMING OF NATURAL GAS



Relatore

Prof. Andrea Lanzini

Correlatore

Ing. Marco Marchese

Candidato

Francesco Masilla

MARZO 2019

Table of Contents

[1] INTRODUCTION	[1]
[2] FISCHER-TROPSCH PROCESS	[5]
<i>[2.1] Development</i>	<i>[5]</i>
<i>[2.2] FT feedstock</i>	<i>[7]</i>
[2.2.1] Solid/liquid carbon sources (CBL, BTL, WTL)	[8]
[2.2.2] Gas carbon sources (GTL)	[9]
<i>[2.3] FT products</i>	<i>[11]</i>
[2.3.1] Hydrocarbons	[12]
[2.3.2] Oxygenates	[13]
<i>[2.4] FT distilled products - fuels</i>	<i>[14]</i>
[2.4.1] Motor gasoline	[14]
[2.4.2] Jet fuel	[16]
[2.4.3] Diesel fuel	[18]
<i>[2.5] FT operating and design configurations</i>	<i>[20]</i>
[2.5.1] HTFT reactors	[22]
[2.5.1.1] CFB – Circulating Fluidized Bed reactor	[22]
[2.5.1.2] SAS – Sasol Advance Synthol reactor	[24]
[2.5.2] LTFT reactors	[25]
[2.5.2.1] MTFB – Multi-tubular Fixed Bed reactor	[26]

[2.5.2.2] SBC – Slurry Bubble Column reactor	[27]
[2.5.3] Micro-reactors	[29]
[3] FISCHER-TROPSCH SYNTHESIS	[33]
<i>[3.1] FT catalysts</i>	<i>[35]</i>
[3.1.1] Iron-based catalysts	[36]
[3.1.2] Cobalt-based catalysts	[40]
<i>[3.2] FT selectivity models</i>	<i>[46]</i>
[3.2.1] ASF model	[47]
[3.2.2] Double alpha model	[50]
[3.2.2] Secondary olefin re-adsorption models	[52]
[3.2.2.1] Inhibited-diffusion olefin re-adsorption	[52]
[3.2.2.2] Enhanced-solubility/physisorption olefin re-adsorption ...	[54]
[3.2.4] Chain length olefin desorption models	[57]
<i>[3.3] FT kinetic models</i>	<i>[59]</i>
[3.3.1] FT reaction mechanisms	[61]
[3.3.1.1] Alkyl mechanism	[62]
[3.3.1.2] Alkenyl mechanism	[63]
[3.3.1.3] Alkylidene mechanism	[64]
[3.3.1.4] Enol mechanism	[66]
[3.3.1.5] CO insertion mechanism	[67]
<i>[3.4] Effects of process conditions on selectivity</i>	<i>[69]</i>
[3.4.1] Temperature	[70]
[3.4.2] Pressure	[71]

[3.4.3] Reactant feed ratio	[73]
[3.4.4] Conversion level	[74]
[4] FT WAX HYDRO-CRACKING	[77]
[4.1] <i>Hydro-cracking catalysts and operating conditions</i>	[78]
[4.2] <i>Hydro-cracking reaction mechanisms</i>	[80]
[4.2.1] Kinetic model approaches	[82]
[5] GTL PLANT MODEL DESCRIPTION	[84]
[5.1] <i>Chemical components</i>	[85]
[5.2] <i>Property method</i>	[89]
[5.3] <i>Property constant estimation (PCES)</i>	[93]
[5.3.1] Pure component Constant properties	[95]
[5.3.2] Pure components Temperature-dependent properties	[97]
[5.4] <i>Property constant estimation (applied)</i>	[100]
[5.4.1] Alkanes (normal paraffin)	[100]
[5.4.1.1] Normal boiling temperature	[100]
[5.4.1.2] Critical temperature	[101]
[5.4.1.3] Critical pressure and acentric factor	[103]
[5.4.2] Methyl-alkanes (mono-branched paraffin)	[106]
[5.4.2.1] Critical properties and acentric factor	[106]
[5.4.3] Olefins	[107]
[5.4.3.1] Critical properties and acentric factor	[107]
[5.4.4] Mathias-Copenam alpha function	[109]

[5.4.5] Binary parameters (classical mixing rule)	[111]
<i>[5.5] Kinetic models</i>	<i>[112]</i>
[5.5.1] FT synthesis	[115]
[5.5.2] Hydro-cracking	[123]
[6] INTEGRATED GTL PROCESS	[127]
<i>[5.1] Syngas generation unit</i>	<i>[127]</i>
<i>[5.2] Syngas conversion unit</i>	<i>[130]</i>
<i>[5.3] Upgrading unit</i>	<i>[132]</i>
[7] RESULTS AND DISCUSSIONS	[135]
<i>[7.1] Effects of recycle</i>	<i>[136]</i>
[7.1.1] Effects of recycle on reactor sizes	[136]
[7.1.2] Effects of recycle on process efficiency	[139]
[7.1.3] Effects of recycle on GHG emissions	[143]
[7.1.4] Effects of recycle on plant selectivity	[144]
[APPENDIX] FORTRAN USER SUBROUTINE	[149]
<i>[A.1] Installation pathway</i>	<i>[149]</i>
<i>[A.2] Code development</i>	<i>[150]</i>
<i>[A.3] Compiling and linking</i>	<i>[153]</i>
<i>[A.4] FT Fortran code</i>	<i>[155]</i>
<i>[A.5] Hydro-cracking Fortran code</i>	<i>[159]</i>
[REFERENCES]	[166]

Acknowledgments

I would like to express my gratitude to prof. A. Lanzini and M. Marchese for their support and patience and to my parents for their encouragement and continuous efforts.

ABSTRACT

Gas-to-Liquids process refers to the technology for chemical conversion of natural gas into synthetic crude that can be upgraded and separated into different useful hydrocarbon cuts including liquid transportation fuels.

In this study, steam and CO₂ feed are used to reform natural gas and produce syngas. Syngas is converted to liquid hydrocarbons through a cobalt-based Fischer-Tropsch plug flow reactor. Heavy fractions are treated with hydrogen at high pressure in a hydro-cracking plug flow reactor to improve amounts and quality of the middle distillate fraction.

The process has been simulated in ASPEN Plus and the kinetics of Fischer-Tropsch and hydro-cracking reactions both are implemented by means of Fortran-based kinetics subroutines. Thermodynamic properties of heavier molecules are obtained by suitable correlative or iterative procedures from literature or by Aspen Property estimation tools.

Recycling of unconverted and light gases to such an extent has been investigated and optimized in terms of reactor sizes, process efficiency, product selectivity and green-house-gas emissions.

1. INTRODUCTION

Earth is close to the point of no return. We must act immediately to avoid that global warming have disastrous and irreversible consequences: it is the appeal that emerges from last report drawn up by the Intergovernmental Panel on Climate Change (IPCC), met last autumn in Copenhagen

There' s no doubt on the causes of climate change: the man-made massive injection of green-house-gases into the atmosphere, which largest contribution to comes from the enormous world energy needs, which are far away from being satisfied in a sustainable manner: more than 90 % of the energy technology installed is fossil-fuel based. Gas emissions from their use are known for increasing the average global temperature, which is disastrous for the environmental equilibrium of our planet.

Of all harmful gases coming from combustion of fossil fuels, carbon dioxide is that already present into the atmosphere and suitable concentrations are known to help sustaining a habitable temperature on the planet. Since the 18th century, however, carbon dioxide emission has never stopped increasing even more rapidly with years, disrupting natural carbon cycle and leading to a planetary warming impact.

Currently thermal, mechanical and electric energy are almost exclusively produced by oxidation of carbon-embedding molecules and many important processes involving chemical, physical or biological transformation result in carbon dioxide emission.

The IPCC data reveal that carbon dioxide emissions has been growing much faster during the last three decades compared to other green-house gases (Fig. 1.1) and several scenarios indicate that carbon dioxide emission has prospected to not going down in the next following decades [IPCC, 2018].

Quantitatively, carbon dioxide emission has reached 35 billion tons in 2015 (Fig. 1.1), rather high compared to methane (8 billion tons of CO₂-equivalent) and other GHG' s, among which nitrous oxide (N₂O) and the "F species" (PFC, HFC, SF₄) are most recognized for warming impact [IEA GHG, 2000].

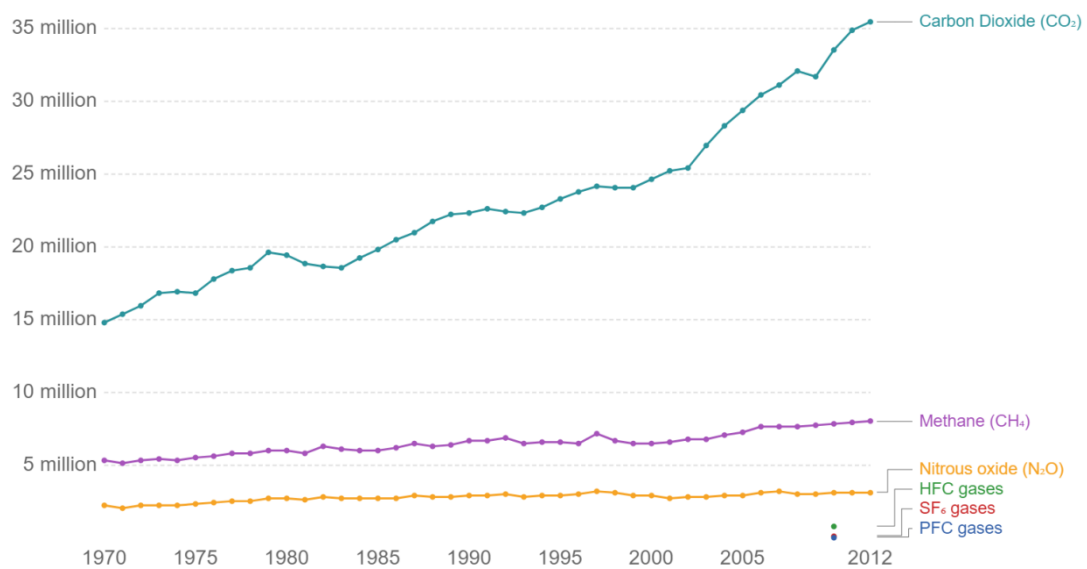


Figure 1.1: global green-house-gas emissions by gas source, measured in thousand tons of carbon dioxide equivalents (Kt CO₂eq). Gas emissions are converted to their CO₂e values based on their global warming potential factor (World Development Indicators, The World Bank).

Power and industry sectors combined dominate current global CO₂ emissions, accounting for about 60 % of the total injection.

The transport sector dominates the scattered and mobile source CO₂ emission cluster; however any direct implementation of carbon capture system into this sector would turn to be nullified by excess weight equipment and compression efficiency losses. Eventually, centralized production of carbon-free and more performant fuels (ethanol, methanol and hydrogen) could be economically viable and CO₂ sustainable [IPCC, 2004]; however, current fossil-fuel engine technologies and missing distribution networks limit the development. Exxon Mobile, one of the world' s oil and gas companies, projected that the world will continue to rely on oil for heavy vehicles, shipping and aviation for the next decades.

Projections for the future (up to 2050) indicate that the number of emission sources from the stationary sectors is likely to increase, mainly in Southern Asia (Indian sub-continent) and South-east Asia (eastern cost). The CO₂ emissions in these sectors are generated by boilers and furnaces burning fossil fuels and are typically emitted from large exhaust stacks [IEA GHG, 2000].

Hence, the volumes produced by these sources are usually large, as well as fixed and stationary, which are the reasons why they represent potential opportunities for the

addition of a carbon capture system. However, the attractiveness of a particular CO₂ source for capture depends, besides on its volume, also on concentration and partial pressure (Fig. 1.2), in turn on type of fossil fuel burned, plant size and energy and material stream processing features. For example, coal is currently the dominant fuel in power sector (Fig. 1.2), whilst in the refining and chemical sectors oil and gas are primary fuels [IPCC, 2000].

Process	CO ₂ concentration in gas stream (% vol.)	Number of sources	Emissions (MtCO ₂)	% of total CO ₂ emissions	Average emissions/so urce (MtCO ₂)
<i>Power</i>					
<i>Coal</i>	12 to 15	2025	7984	56.69	3.94
<i>Natural gas (1)</i>	7 to 10	743	752	5.62	1.01
<i>Natural gas (2)</i>	3	985	759	5.68	0.77
<i>Fuel oil (1)</i>	8	515	654	4.89	1.27
<i>Fuel oil (2)</i>	3	593	326	2.43	0.55
<i>Cement production</i>					
	20	1175	932	6.97	0.79
<i>Refineries</i>					
	3 to 13	638	798	5.97	1.25
<i>Iron and steel industry</i>					
	15	180	630	4.71	3.50

Figure 1.2: worldwide large CO₂ stationary sources emitting more than 0.1 Mt CO₂ per year (adapted from IEA GHG, 2002a).

Emissions from refineries account for about 6% of the total emissions (Fig. 1.2), almost reaching 1 billion tons of CO₂ per year; however, refining sector presents multiple sources in a large concentration range (3-13% in gas stream by volume), despite of each plant emits large amounts (1,25 million CO₂ tons on average). Globally, the refiner sector ranks third among stationary CO₂ producers, after the power production sector and the cement industry [IEA GHG, 1999]. Other larger producers are the iron and steel industry and the petrochemical industry [IEA GHG, 2000b]. In particular, integrated steel mill could take

advantage from larger volume sources (blast furnaces) and concentrations (from 15 to 27%), which are higher than in the flue gas from power stations (up to 15%).

In particular, emissions from refineries include not only carbon dioxide, which result from flue gas from energy/chemical acquirement, but also large amounts of natural gas, which is either co-produced with petroleum or sits on the top of petroleum reservoirs. A new report by General Electric estimates that 5 % of the world' s natural gas produced by refineries is wasted by 'flaring' (combusted and vented). This is a huge wasting of resources, which equals 30 % of natural consumption in European Union, but also a significant pollution source, involving yearly emissions of about 400 million metric tons of carbon dioxide, the same as 77 million cars. Since there' s no local market for this gas, refineries are forced to flare it, seriously threatening environmental safety. Alternatively, refineries can reinject it back into the reservoirs but reinjection process is well-known for seriously affecting the operative costs.

Carbon capture technology has been validated and proved but its widespread is still very limited, because cost and investment obstacles remain for any sector making it an expensive integrative process. Moreover, far and not suitable (metamorphic or igneous rather than sedimentary) storage basin could hide the technical and, even more, the economic potential of the entire process.

Recently, research started focusing on recycling CO₂ concentrated streams into liquid fuels through catalytic process (Fischer-Tropsch process) for reducing fuel-cycle-wide emissions and further re-valorizing the carbon embedded in the inert molecule.

Effectively, an energy-efficient catalytic CO₂ conversion could have major advantages in reducing both greenhouse gas emissions and dependence on fossil resources.

2. FISCHER-TROPSCH PROCESS

2.1 Development

The process of converting solid or gaseous feedstock into liquid transportation fuels and/or valuable chemicals through catalytic process is known as Fischer-Tropsch process, from the two German scientists that first converted gaseous mixture of carbon monoxide and hydrogen into liquid hydrocarbons over iron-based catalyst, at the Fuel Research Laboratories of the Kaiser Wilhelm Institute for Kohlenforschung in the 1920' s. After that, the Fischer-Tropsch synthesis has gone through periods of discovery and burying mainly on the wave of crude oil prices.

One decade after discovery German military scientists started the development of commercial FTS process, driven by the lack of crude oil reserves of its own. The first small plant was born in Mulheim in 1932, followed by a larger pilot plant in Oberhausen-Holten in 1934, with a capacity of 200 bbl/day.

The Second World War pushed the production of liquid fuels for naval and air forces through direct coal liquefaction (DCL) and coal-to-liquids (CTL) process, leading German FTS-derived fuel production to 12000 bbl/day.

On the other side of the world, US Bureau of Mines had gained the general keys of FTS technology too and its studies on FTS process, lasted forty years ever since, led to operation of the first GTL plant (Brownsville, Texas) in 1951, with the capacity of 7000 bbl/day.

The first commercial larger CTL plant constructed after the German plant decommissioning was in 1955, in Sasolburg, South Africa (120000 bbl/day in 2015) by SASOL (South Africa State Oil). However, at that time large oilfields were discovered in the Middle East, providing ample supply of oil that had to be distilled and upgraded only, letting crude-derived gasoline and gas oil prices down.

Therefore, all main FTS production plant began to be closed due to cheaper alternatives, except the Sasolburg plant that continued to sustain liquid fuel demand through coal-derived syn-fuels during the international trade embargos South Africa experienced for the Apartheid system. Until 1973, when OPAEC organization states the crude oil export lock, no new plant was commissioned.

By then, the black gold rush opens up new opportunities for FTS expansion and during these years interesting advances were made in the catalyst preparation and reactor design.

Further crude price declines didn't stop research and development of new syn-fuel plants anymore; in support of this, Sasol extended Sasolburg plant up to 120000 bbl/day production and, although further decrease in price of crude, two oil service company, Shell and PetroSA, commissioned two large scale plants, in Bintulu, Malaysia, and Mossel Bay, South Africa, respectively.

These plants use natural gas feedstock, which became really cheaper due to its intense use and related access network in residential and power sectors; and recently, discovery of large amounts of shale gas has made natural gas more abundant and cheaper, enlarging the profit margin of GTL plants world-wide.

Moreover, some of these gas reserves are too small or too remote from sizable population, hiding the economic potential for its exploiting by natural gas pipelines, and attempting alternative solutions for their exploitation like conversion to more handling and valuable liquid fuels could be. This could represent a potential for countries to monetize reservoirs that would not have any market otherwise.

Some of these so called 'stranded' reserves are discovered in Qatar where last large GTL plants started up: Oryx GTL plant by Sasol and Pearl GTL by Shell (as joined venture with Qatar Petroleum), with capacities of 34000 and 140000 bbl/day, respectively.

The process to convert liquid, solid or gas feedstock to liquid fuels or chemicals can be divided into three process steps:

1. Syngas generation;
2. Syngas conversion;
3. Hydro-processing.

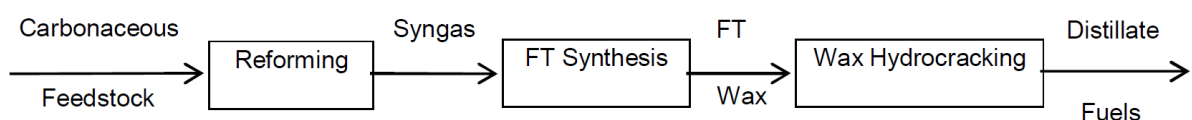


Figure 2.2: distillate production chain from [Dry et al., 2001]

Although all three of these technologies are well established, individually optimized and commercially proven, the combined use is not widely applied. This poses an interesting challenge to the designer in order to obtain most cost-effective combination of these technologies.

Generally, this sequence of process is referred as *indirect liquefaction*, because the feed is transformed first into syngas and then syngas is converted into products.

Once the feed has been converted to syngas, which is a mixture of carbon monoxide (CO) and hydrogen (H₂), the syngas can be conditioned to be applied as feed for any of the syngas conversion technology. Fischer-Tropsch synthesis is not the only possible technology for the conversion of the syngas into a synthetic fuel but together with syngas to methanol, Fischer-Tropsch synthesis is industrially the more relevant.

2.2 FT feedstock

Feed to syngas conversion is an extremely energy intensive process but it have many advantages related to the wide flexibility of the feed-to-syngas process. Actually, one of the major advantages of the indirect liquefaction process over direct liquefaction is the wide selection of feed materials that can be used.

However, industrial Fischer-Tropsch facilities are currently only used for coal-to-liquids (CTL) and gas-to-liquids (GTL) conversion only, due to availability and price motivations.

But the type of feed materials that can be converted is not only restricted to coal and natural gas: the conversion of biomass in a biomass-to-liquids (BTL) process and waste in a waste-to-liquids (WTL) process can likewise be taken into account. Biomass represents a renewable source of energy whereas waste conversion owns the beneficial reuse of discarded material. However, biomass derived feed is not concentrated at a single point of origin. Furthermore, biomass and waste have a low energy density and feed logistics involved in collecting and transporting either the biomass or waste from their point of origin to the indirect liquefaction facility adds to the cost and complexity of the process.

Collectively, all these processes can be referred to as feed-to-liquids or XTL (i.e. 'anything-to-liquid') conversion process, where X represents the carbon source for syngas [Selvatico et al., 2016].

2.2.1 Solid/liquid carbon sources (CTL, BTL, WTL)

Solid and liquids (such as coal, biomass and liquid waste) are converted into syngas by means of a gasification process. Gasification takes place in the range 800-1800 °C (depending of the gasifier technology) in the presence of sub-stoichiometric amount of oxidant (O₂) and a moderator (typically H₂O). The process consist of two major simultaneous reactions of carbon in air/oxygen and water, namely partial oxidation with oxygen (exothermic) and water-shift reaction with water (endothermic).

The carbon sources that are typically considered as solid sources are coal, petroleum coke, biomass and waste. These different solid raw materials differ widely in composition, and even within each type there is much variation. Moreover there are several issues arising from both mineral matter and amount of water inevitably contained in any of the aforementioned solid carbon sources. All of the mineral matter will ultimately be rejected as ash or slag from the bottom of the gasifier and the inevitably creation of solid waste requires complex handling and disposal procedures.

The mineral matter also reduces the thermal efficiency of the process, since it has to be heated up to gasification temperatures, but heat recovery from mineral matter is difficult. Meanwhile the water trapped into the solid raw material reduces the heat calorific value.

Handling of solids is normally more expensive than liquid or gas handling. The transportation of the solid raw material from its point of origin to the gasifier and its subsequent pre-treatment has a great impact on economics of the process. Also cleaning and conditioning are very intensive and thus costly for solid/liquid if compared to gas carbon sources. The raw syngas produced by gasification of solid raw materials may contain significant quantities of steam, pyrolysis products, light hydrocarbons, methane, Sulphur and nitrogen-containing gases (mainly H₂S, COS and NH₃) and CO₂. Therefore the solid/liquid derived syngas naturally requires more intensive cleaning.

The preparation of syngas as feed material for Fischer-Tropsch synthesis is by far the most expensive process irrespective of the feedstock considered [de Klerk, 2011a]. However, when the raw material is a solid, such as coal, the delivery of clean and conditioned syngas to the FT reactor can easily account for more than 70 % of the capital cost of the whole plant.

2.2.2 Gas carbon sources (GTL)

During the last decade there has been a renewed interest in the use of Fischer-Tropsch technology for the conversion of natural gas to liquids. The reasons that could explain such interest lie in the willingness to capitalize reservoirs with no local market or recent discovery of large reservoirs, as aforementioned. More recently, stringent safety and environmental concern have pushed towards the utilization of the natural gas co-produced with petroleum, which mostly is flared or vented.

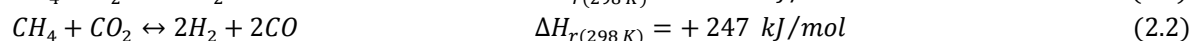
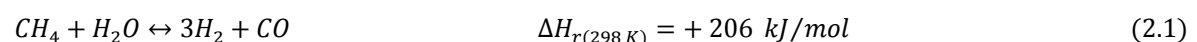
Moreover the relative capital cost for natural gas conversion to syngas is less than that for solid/liquid feedstock, and natural gas to syngas conversion is less challenging from a technology point of view.

Natural gas is converted into syngas by gas reforming. There are currently three well established reforming technologies:

- i) Steam reforming;
- ii) Partial oxidation (POX and CPO);
- iii) Auto-thermal reforming (ATR).

The choice of the reformer will have an influence on the thermal efficiency of the plant as a whole and on the capital cost of the reformer, oxygen plant (In the case of POX reformer) and the Fischer-Tropsch section. Thermodynamically, high temperatures, low pressures and high steam to methane ratio favor methane conversion into syngas.

Steam reforming is a catalytic process in which natural gas (mainly methane) and steam, with or without CO₂, are converted by endothermic reforming reactions into CO and H₂ (eq. (2.1) and (2.2)) over a nickel-based catalyst (Ni-Al₂O₃) and heat is supplied externally (by combustion of part of the fuel in air):

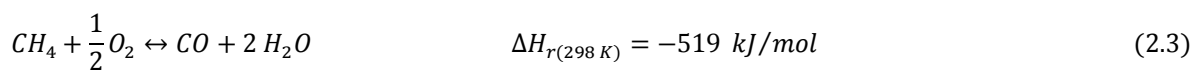


The outlet temperature of steam reformer ranges between 820 and 880 °C. Generally, temperatures below 900 [°C] are associated to lower methane conversion. The steam to methane ration is usually 2.5 – 5.0 [Bourbonneux, 1998]. High steam to methane ratios lower the risk of carbon deposition and increase methane conversion but also increase

the H₂/CO ratio of the syngas over that needed by the Fischer-Tropsch syngas conversion stoichiometry. Typical values are well above 5:1. Moreover such a high usage of water makes unsuitable for arid regions.

The hydrogen to carbon monoxide ratio can be reduced by co-feeding CO₂ (eq. (2.2)), as well as by using a lower steam to methane ratio in the feed. However low steam pressures can favor formation and deposition of carbon on un-promoted nickel-based catalysts.

Adiabatic oxidative reforming (eq. 2.3) usually is a non-catalytic process but, irrespective of whether it employs a catalyst (CPO) or not (POX), takes place by exothermic partial combustion of the natural gas to produce CO while supplying heat for the endothermic reactions (eq. (2.1) and eq. (2.2)):



An oxidant (typically pure oxygen) is mixed with natural gas and, as there is no catalyst, the mixture is subjected to high temperatures, typically in the order of 1300-1400 °C. The POX process is followed by a section to recover heat from the raw synthesis gas, as well as a section to remove carbon (soot) and ammonia and HCN produced in high amounts during POX (it necessitates of a scrubber to clean gas). The H₂/CO ratio is typically on the range 1.6-1.9, close to the optimum needed by the Fischer-Tropsch section.

Auto-thermal reforming foresees that the oxidant and steam are mixed with the gaseous feed, like for POX, but unlike POX, auto-thermal reforming uses a catalyst to reform natural gas to syngas. Due to the milder operating conditions (exit temperature of 1000 °C) and the use of steam (steam to methane ratio more than 1.3), the syngas is soot free and less ammonia and HCN are produced.

However, at steam to methane ratio of 1.3 the syngas produced will have H₂/CO ratio of 2.5, still above than the ratio needed by the FT section. The H₂/CO ratio can be controlled lowering the steam to methane ratio or recycling the CO₂ from the FT section to the reformer.

2.3 FT products

With the term *syncrude* one refers to the rich variety of products obtained from FT process train. The term highlights the synthetic nature of a crude oil-like mixture. Indeed, like crude oil, also syncrude composition is extremely variable but mostly composed by hydrocarbons. While for crude oil properties of each blend are determined by the geomorphology of the basin, syncrude characteristics depend on the synthetic process that syngas undergoes, which means mainly on both FT catalyst type and operating conditions.

In particular, syncrude derived from low temperature applications (LTFT) is a liquid mixture of saturated hydrocarbon molecules, mainly n-paraffins, whereas high temperature modes of operation (HTFT) yield gas mixture of lighter linear hydrocarbons with higher amounts of unsaturated species (olefins). If iron based catalysts are generally preferred at high temperature synthesis, low temperature reactors may be charged with either cobalt or iron catalysts. The typical composition for syncrude from the aforementioned operation modes are displayed in the table below:

Table 2.1: syncrude composition in terms of hydrocarbon classes and oxygenates that are typical for the three main different applications (Fe-HTFT, Fe-LTFT and Co-LTFT)

Product fraction	Carbon range	Compound class	Syncrude composition ^a (mass%)		
			Fe-HTFT	Fe-LTFT	Co-LTFT
Tail gas	C ₁	Alkane	12.7	4.3	5.6
		Alkene	5.6	1.0	0.1
		Alkane	4.5	1.0	1.0
LPG	C ₃ -C ₄	Alkene	21.2	6.0	3.4
		Alkane	3.0	1.8	1.8
Naphtha	C ₅ -C ₁₀	Alkene	25.8	7.7	7.8
		Alkane	4.3	3.3	12.0
		Aromatic	1.7	0	0
		Oxygenate	1.6	1.3	0.2
Distillate	C ₁₁ -C ₂₂	Alkene	4.8	5.7	1.1
		Alkane	0.9	13.5	20.8
		Aromatic	0.8	0	0
		Oxygenate	0.5	0.3	0
Residue/wax	C ₂₂ +	Alkene	1.6	0.7	0
		Alkane	0.4	49.2	44.6
		Aromatic	0.7	0	0
		Oxygenate	0.2	0	0
Aqueous product	C ₁ -C ₅	Alcohol	4.5	3.9	1.4
		Carbonyl	3.9	0	0
		Carboxylic acid	1.3	0.3	0.2

Source: (A. De Klerk, 2011)

The values from (Table 2.1) are representative of the three ways of FT application, but within each syncrude type considerable variations can be found, due to various types of reactor technology, catalyst preparation, catalyst deactivation and operating conditions apart from temperature, such as pressure, relative amount of hydrogen to carbon monoxide in the syngas and gas space velocity (level of conversion) [de Klerk, 2011].

A relevant difference between syncrude and crude oil lies in the presence of a not negligible amount of oxygenate products in the former that are mostly missing in crude oil. Generally low temperature FT applications bring to higher amount of oxygenated products, such as carboxylic acid, alcohol and aldehydes, even up to 15 wt. % .

Thus hydrocarbons and then oxygenates are the two main classes of compounds obtainable from FT synthesis.

2.3.1 Hydrocarbons

The hydrogenation of carbon monoxide theoretically could bring to all classes of hydrocarbon compounds, but typical syncrude shows a net presence of the following hydrocarbon classes:

- n-alkanes: the saturated hydrocarbons are mostly linear alkanes (n-paraffins), especially long chain molecules (waxes) because branching typically decreases with increasing chain length. Branched alkanes are also present to a minor extent; mainly methyl branched with a single branch per chain (mono-methyl alkanes) are formed together with little amounts of cycle-alkanes (or naphthenes) prevalently in HTFT rather than LTFT operative mode.
- n-alkenes: the unsaturated hydrocarbons are dominated by alkene class, that is mainly composed of linear olefins. The double bond generally is located in α position due to the termination step impressed to the growing chain by FT catalysts. Branched and cycle-alkenes are even present but at low concentrations and the same location for the double bond has been found for these species.

- aromatics: a little amount of hydrocarbon compounds derived from benzene have been usually identified in the product spectrum of HTFT operating reactors, but most of these are mono-nuclear aromatics with an alkyl chain as side chain, such as toluene. Di-nuclear and poly-nuclear aromatics may be present but in negligible amounts. Syncrude derived from low temperature applications is almost devoid of aromatics.

2.3.2 Oxygenates

Fischer-Tropsch products are not only hydrocarbons, but also include different classes of oxygenated compounds. Like the alkenes, the relative concentration of oxygenates in each carbon number fraction decreases with chain length. Different classes of oxygenates formed within FT reactors are alcohols, aldehydes and carboxylic acids. It is thought that oxygenates and hydrocarbons share the same propagation network up to termination, thus being mainly formed upon desorption and not by hydrogenation. [de Klerk, 2011].

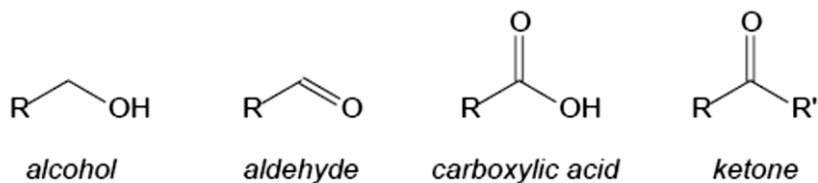


Figure 2.3: different classes of organic oxygenates in FT syncrude

Furthermore D. Gall et al. found that n-primary alcohols constituted 40 % in weight of the organic liquid products and 92.4 % of the oxygenated products over Cobalt catalyst at very low temperatures (160-175 °C) [Gall et al., 1952]. Such amounts of alcohols lead to evidence in favor of the view that n-alcohols are the precursor of hydrocarbons in the synthesis.

The oxygen content of these molecules may polarize the entire mixture but actually molecule polarity decreases with increasing chain length, due to ever greater portion of the chain occupied by the nonpolar fraction (aliphatic portion). Polar compounds are found in the aqueous phase and solubility of organic oxygenates into water decreases

with increasing chain length, so that lighter oxygenates are mostly separated from the oil fraction.

Ketones may be found, especially at more severe operating conditions (HTFT), but generally they are recognized as secondary products originated after decomposition of carboxylic.

The carboxylic acids are seriously deleterious for FT process due to catalyst deactivation promoting effect and for being corrosive towards vessel and piping material.

Alcohols, aldehydes and carboxylic acids are mainly linear and the degree of branching (methyl branching) typically reduces with increasing chain length.

2.4 FT distilled products - fuels

The product stream from a standard FTS reactor can also be defined as various fuel types: LPG ($C_3 - C_4$), gasoline/naphtha ($C_5 - C_{10}$), kerosene or jet fuel ($C_{11} - C_{13}$) and diesel fuel ($C_{14} - C_{22}$). The definitions and conventions for the composition and the name of different fuel types are obtained from crude oil refining technology.

The products from FTS are higher value because diesel fuel, jet fuel and gasoline are generally sulphur (removed by pretreatment step before FT processing) and nitrogen free and low in concentration or absent of aromatics.

Moreover the FT products could be also suitable as precursor for more valuable chemical production for food application, cosmetics and medicine [de Klerk, 2013]. For example olefins from C_9 to C_{15} may be suitable for synthesizing biodegradable detergents whereas higher weight waxes for use as lubricants.

Basically the molecular properties of a fuel have a significant impact on engine performance and emissions. These properties are governed on a regional basis by fuel specifications despite the global nature of the automotive industry. The fuel specifications are commonly legislated and determine the minimum fuel quality standards of a certain country (e.g. EN:228 for motor gasoline and EN:590 for diesel in European Union) or

could be just guidelines (not legislated), such as those of World-Wide Fuel Charter (WWFC) developed by associations of automobile manufacturers [de Klerk, 2013].

Properties of major types of Fischer Tropsch derived fuels and how they meet fuel specifications are described in the following paragraphs.

2.4.1 Motor Gasoline

Motor gasoline is the most demanding of the transportation fuels in terms of its refining requirements due to the stringent technical specifications imposed by engine design (efficient combustion) and emission performance of a vehicle.

Highest efficiency for a spark-ignition engine can be achieved properly timing the spark and the fuel must not ignite before then. When a fuel auto-ignites, the combustion rate and associate pressure increase is much higher, giving rise to a knocking and to structural stress that over extended period will destroy the engine. The ability of a fuel to resist auto-ignition during engine operation is a key motor-gasoline quality parameter and it is quantitatively measured by its octane number (RON – Research Octane Number and MON – Motor Octane Number).

The octane number of the alkanes in motor gasoline decreases with increasing carbon number and decreasing degree of branching. In particular linear alkanes (n-alkanes) are highly susceptible to autoxidation (first step of auto-ignition reaction), the reason why they are inherently the lowest octane number compounds in motor gasoline.

However n-alkanes are main products from FT synthesis and they are the only compound class that is not restricted by motor gasoline specifications (Tab. 2.2); hence it would be better to convert n-alkanes to higher octane number species (methyl branched alkanes or aromatics) through hydro-isomerization or reforming.

Aromatics are good octane components with high energy density. The negative attributes of aromatics in motor gasoline are mainly related to its benzene content, known for carcinogenic effect on humans. By that motor gasoline specifications limit the total aromatic content, as well as the benzene content specifically (Tab. 2.2). Fortunately the

limitation of aromatic content is not an inherent issue for syncrude especially for that derived from LTFT due to low or no content of aromatics.

Table 2.2: selected requirements for motor gasoline properties in Europe (EN:228) together with auto-manufacturer's recommendations (WWFC)

Property	European 2009/30/EC	WWFC:2013 Category 4
RON	≥ 95	≥ 95
MON	≥ 85	≥ 85
Density at 15 °C (kg/m ³)	720 – 755	715 – 770
Hydrocarbon content (vol%)		
Olefins	≤ 18	≤ 18
Aromatics	≤ 35	≤ 35
Benzene	≤ 1	≤ 1
Sulphur content, mg/kg	≤ 10	≤ 10

(source: IEA-Advanced Motor Fuels)

For what concerns alkenes, they are generally absent in crude oil refineries and the olefin produced throughout high temperatures conversion units have greater value for motor gasoline production after aliphatic alkylation, etherification and olefin oligomerization. In a HTFT derived syncrude refinery, the olefins are abundant and olefin content in synthetic motor gasoline could approach 30% (as reported for FT motor gasoline at Sasol Synfuels plant) [de Klerk, 2013]. Although the alkenes have generally high octane numbers than the corresponding alkanes, the short-chain alkenes are known to increase ozone-forming emissions and at high concentrations they could create serious problem for existing refineries. Therefore they are limited by fuel specifications (for Euro IV the olefin content is maximum 18%) (Tab. 2.2).

2.4.2 Jet Fuel

Jet fuel belongs to the kerosene cut, mostly lying in the 190-230 °C boiling range. Since the II World War, when the power source changed from spark-ignition engines to turbine engines, jet fuel displaced aviation-gasoline as main fuel for most of civilian and military aircrafts. Since turbine engine has to bear more severe operative conditions and deal with the risks related to high altitudes, the specification for a jet fuel are quite stringent and of international nature, without local variations in legislation neither influence from politics as occurs for motor gasoline and diesel fuel.

The DEF STAN 91-91 is widely recognized as the international standard to specify the civil jet fuel Jet A-1 (Tab. 2.3), whereas fuel for military use is not subjected to the same need for international specifications as civilian aircraft.

Differently to road transportation fuels, jet fuel is combusted in an open chamber and the hot gases are used to drive the turbine blades. Poor combustion will lead to both energy losses and high hydrocarbon emissions, but also to generation of particulate matter that can damage the blades.

Therefore the energy content and combustion quality turn out to be most important performance property for a jet fuel. In this sense aviation fuel specification A-1 (Tab. 2.3) places a lower limit for the *net heat of combustion*, which is the energy released when the fuel is completely oxidized to form carbon dioxide and water. In particular the specification for civilian aircraft sets a minimum for the gravimetric energy content (MJ/Kg), while the volumetric energy (MJ/m³) content is usually regulated for military aircrafts.

The low density and high content of alkanes, meaning high gravimetric energy content, render the Fischer Tropsch derived jet fuel suitable to meet civilian jet fuel requirements [de Klerk, 2013].

As mentioned before, any specification for jet fuels foresees a parameter accounting for the quality of fuel combustion. It is the *smoke point*, which measures the tendency of a fuel to form carbonaceous particles (black smoke) during combustion. These solid particles can cause hot spots on the chamber wall that may lead to cracks and premature

engine failure. Moreover they can block the holes that supply air to combustion chamber and can hit the turbine blades leading to erosion of the turbine section [de Klerk, 2013]. Aromatics and especially naphthalenic compounds are responsible for the formation of such particles due to their high molecular ratio between carbon and hydrogen atoms. For this purpose a maximum value for both total aromatics and naphthalenic content has been fixed for meeting A-1 jet fuel requirements (Tab. 2.3) [de Klerk, 2013]. In FT derived jet fuel the aromatic content is very low or absent (especially in LTFT operating mode) and even in HTFT derived jet fuel the naphthalenic content is very limited. Furthermore hydrogen content is usually higher for FT syncrude than for most crude-oil derived jet fuel. Therefore, a high smoke point and a clean combustion (high quality combustion) should be expected for Fischer Tropsch derived jet fuel [de Klerk, 2013].

Table 2.3: selected specification for aviation turbine fuel properties for civilian aircrafts (international standards)

Property	Jet A-1
Net Heat of Combustion (MJ/kg)	\geq 42.8
Smoke Point (mm)	\geq 25
Density at 15 °C (kg/m³)	775 - 840
Composition, (vol %)	
Aromatics	\leq 25
Naphtalene	\leq 3
Sulphur content, (wt %)	\leq 0.3
Freezing Point, (°C)	\leq - 47
Viscosity at -20 °C, (cSt)	\leq 8

(source: IEA-Advanced Motor Fuels)

Another important property of aviation turbine fuel being regulated by specification is the viscosity.

Viscosity greatly influences the performance of a turbine engine in many ways: larger values of viscosity affect the droplet size distribution, increasing the risk of engine flameout, increase the pressure drop along the fuel lines and reduce the cooling efficiency of the jet fuel (used as heat exchange mean for the cooling of engine oil and hydraulic fluid). The jet fuel requirement for viscosity places a limit to the inclusion of material that has a boiling point higher than 260 °C.

Last property to consider is *the freezing point* (Tab. 2.3), which becomes paramount for engine operation at high altitude where temperature can lower down to -40 °C. At this regard FT syncrude is rich in linear materials, which have high freezing point.

2.4.3 Diesel Fuel

Diesel fuel refers to the fuel that is used in compression-ignition engines. The requirements for diesel fuel are diametrically opposed to those for motor gasoline. The fuel charged in spark-ignition engine, as just said, must not auto-ignite before the spark in order to control the combustion and thus ensure a correct engine and emission performance. For a diesel fuel, on the contrary, it is important that the fuel auto-ignites and the delay between fuel injection and start of combustion is short. If the ignition delay is too long, it leads to noisy combustion, very high pressures in the combustion chamber and increased NO_x emissions.

The *cetane number* (CN) is a measure of the compression-ignition delay of a fuel. For good compression-ignition engine performance, a diesel fuel should have a CN higher than a minimum value, which places an upper value on the ignition delay. The ideal fuel for a compression-ignition engine, one having a higher CN, would consist of essentially linear alkanes (CN for n-hexadecane is 100) [de Klerk, 2013].

Since the distillate refined from Fischer Tropsch syncrude is composed of mostly linear paraffins and lower amount of olefins, oxygenates and aromatics, the minimum CN is not an issue to FT syncrude refining. When FTS is carried out at lower temperatures (LTFT) the products from iron and cobalt catalysts are essentially linear and after hydro-treatment

the straight run (stream after atmospheric distillation column) diesel fuel cuts have CN of up to 75 [Calemma, 2009]. The market, often moved by country-specific fuel specifications, requires a cetane number of about 45-50.

Table 2.4: selected requirements for diesel fuel properties in Europe (EN:590) together with automanufacturer's recommendations (WWFC) (source: IEA-Advanced Motor Fuels)

Property	European 2009/30/EC	WWFC:2013 Category 4
Cetane number	≥ 51	≥ 55
CFPP, (°C)	≥ 85	≥ 85
Density at 15 °C (kg/m ³)	≤ 845	820 – 840
Total Aromatics, (wt %)	_ a	≤ 15
Polycyclic Aromatic Hydrocarbons (PAH di+), (wt %)	≤ 8	≤ 2
Sulphur content, (mg/kg)	≤ 10	≤ 10

^a not regulated by specification.

(source: IEA-Advanced Motor Fuels)

On the other hand, as the temperature of diesel is lowered, the highest cetane number components, that are n-alkanes, tend to crystallize out of solution as a wax. The wax may block the fuel filters and fuel lines, rendering engine operation difficult or impossible.

The properties of a fuel at low temperatures are recognized as cold flow properties and defined by wax-related tests, such as the *cloud point* (CP) and the *cold filter plugging point* (CFPP).

CP is the temperature at which the diesel fuel becomes cloudy due to the formation of small wax crystals in the fuel although it could remain filterable and no operation issues are necessary related to higher value of CP. Operational problems for a compression-ignition engine starts when the diesel fuel cannot be easily pumped and filtered anymore. These issues start when temperature lowers just below the temperature established by

CFPP value. This is the reason why generally CFPP value is lower than CP. Suppes and coworkers [Suppes et al., 1998] reported that cold flow properties is the largest development obstacle to direct blending of straight-run FT distillate.

2.5 FT operating and design configurations

There are two different technologies to produce liquid hydrocarbon from synthesis gas through FT process, currently: a high-temperature (HTFT) and a low-temperature (LTFT) based technology. Temperature generally used in HTFT ranges from 320 to 350 °C, while LTFT reactor temperature ranges from 200 – 240 °C.

Main difference between them concerns the number of phases present during normal operation: HTFT reactor configuration foresees two phases (gas-solid), whereas LTFT application shows a liquid (i.e. wax) phase in between the gas and solid (catalyst) means.

HTFT is the reactor of choice when alkenes and/or straight run fuels are desired products [Steynberg et al., 2004] and it is usually performed in fluidized bed reactors, where fluidizing agent act as to avoid localized overheating and condensation of products (liquid phase) in the catalyst. Actually, formation of a liquid phase in the HTFT fluidized bed reactors could lead to serious problems due to particle agglomeration and loss of fluidization [Baird et al., 1980]. At this aim catalyst and operating conditions are selected to obtain lower α (chain-growth-probability) values (Fig. 2.4). This implies that the heaviest HTFT products lie in the gasoline/diesel fuel fraction (up to C20) [Todic et al., 2013].

If the main objective is the production of long chain waxes then the LTFT process configuration is used together with iron or cobalt as active metal phase. Two commercial types of reactors are currently operated for the handling of the liquid phase present in the case of high α values (Fig. 2.4), which are typically involved at low temperatures: a SBC (slurry-bubble-column) reactor type for ideally approaching the perfect mixing of ideal CST (continuous-stirred-tank) reactors and MTFB (multi-tubular-fixed-bed) reactors following the PFR (plug-flow-reactor) differential reactor notion.

Both of the LT reactors are operated with the aim to produce especially diesel fuel, waxes and lubricants.

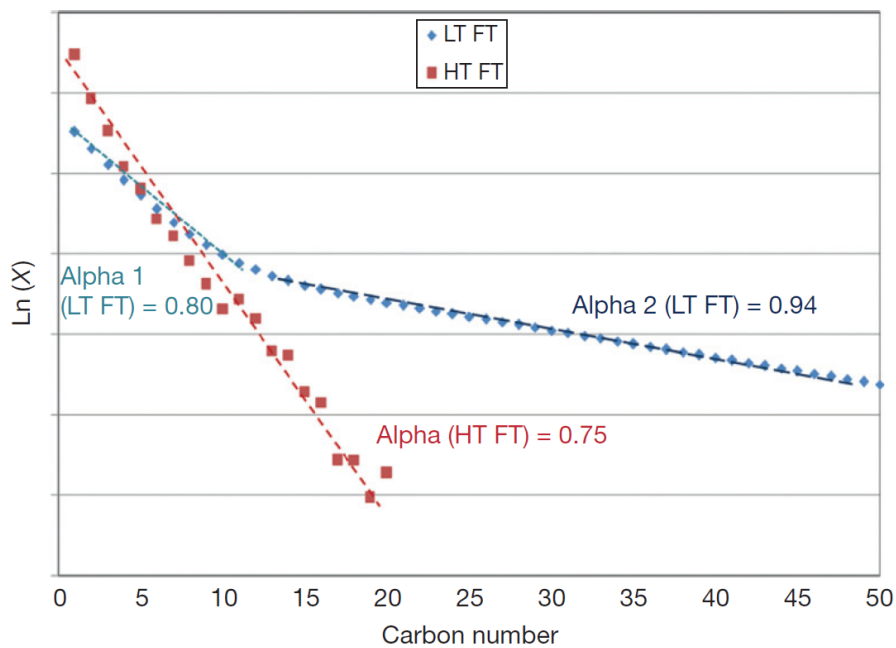


Figure 2.4: logarithmic distribution of FT hydrocarbon products formed over an HTFT catalyst and a LTFT catalyst [Loosdrecht et al., 2013].

There are many scenarios that must be considered when deciding on which type of reactor to use for a certain process.

For high temperature FTS application, heat transfer limitations should be minimized in order not to promote catalyst deactivation or/and carbon deposition due to temperature increase. For lower temperature application, mass transfer coefficients are likely to be improved due to presence of three phases that makes bulk-to-substrate transfer difficult. However, heat transfer rates are substantially higher for fluidized bed and slurry (SBCR) reactors compared to fixed-bed.

Moreover, since the FT reaction is highly exothermic (165 kJ/mol CO converted) both HTFT and LTFT reactors are designed with a view to avoid overheating of the catalyst particles. Any increase in the operating temperature of FT synthesis will result in undesirable increase in the production of methane and may result in catalyst damage [Steynberg et al., 2004].

2.5.1 HTFT reactors

There are essentially two types of commercially used fluidized bed reactors for industrial HTFT application:

- CFB (circulating fluidized bed) reactors;
- FFB (fixed fluidized bed) or turbulent reactors.

2.5.1.1 CFB - Circulating Fluidized Bed reactor

The circulating fluidized bed (CFB) reactor is the older between the two: it was the choice of Sasol for the HTFT Sasol plant at Sasolburg in the 1950' s. Since then the Sasolburg reactor technology was intensively optimized and it was later renamed Synthol (Fig. 2.5).

In a CFB reactor the aerated catalyst (dense fluidized phase) flows down the standpipe through the slide valve, which controls the rate. The catalyst mixes up with the fresh feed and recycle gas (Fig. 2.5) and rises up towards the reaction section (lean fluidized phase). The boiler feed water removes about 40 % of the heat of reaction whereas the rest is adsorbed by the feed gas and products [Dry et al., 1981]. The catalyst and gas separate at the catalyst setting hopper and the aerated catalyst drops down into the standpipe [Steynberg et al., 2004]. Then the gas goes up through the cyclones that removed any fines with 99 % efficiency.

A common operative problem for CFB reactors is the limitation to low conversion and productivity. Actually, it is necessary to have a high catalyst loading in the reaction zone to achieve higher conversion rate. However higher the loading higher the pressure drops over the reaction zone will be. And the pressure drops must never exceed the pressure drop over the standpipe. Actually, if the differential pressure over the standpipe exceeds that over the reaction section it should happen that the feed gas will pass up the standpipe; thus the cyclones will become choked with catalyst and massive losses of catalyst will occur [Steynber et al., 2004].

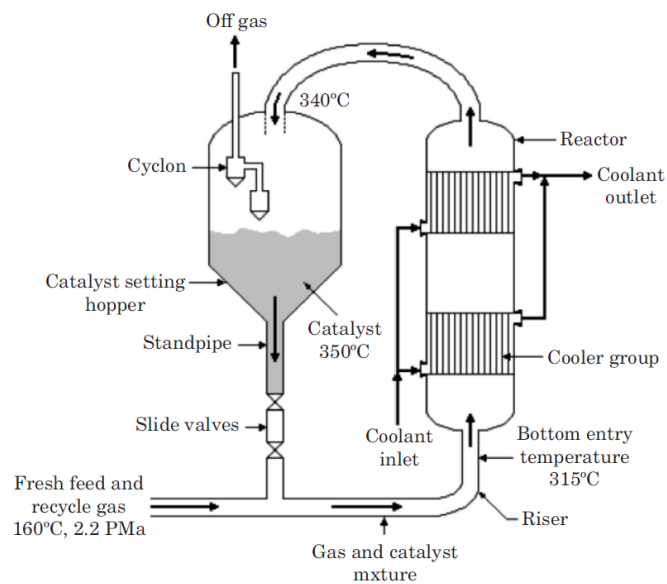


Figure 2.5: Synthol CFB (circulating fluidized bed) reactor [Nawaz et al., 2015].

Moreover, since no heat exchange takes place in the standpipe, there will be a temperature runaway there and the catalyst will risk to be seriously damaged. Therefore catalyst loading turns to be a delicate issue if high productivities (conversion rates) are the target.

Another issue lies in the fact that iron at HTFT operating conditions (320-350 °C and high pressures) is susceptible to carbon deposition. The amount of carbon that is continuously deposited within the catalyst pores leads to a decrease in the density of particles. Lower density means that more rapidly they will be transported upwards by the gas and less catalyst back-mixing will occur, at fixed gas linear velocities [Steynberg et al., 2014]. This causes a decrease in catalyst loading and thus lower conversion rate. Furtherly, also differential pressure over the standpipe decreases as well so that further increase in catalyst loading becomes impossible [Dry et al., 1996]. To counter this on-line catalyst removal and addition of fresh catalyst is applied.

The issues concerning catalyst loading in the circulating fluidized bed reactors are main reasons for the replacement of eight Sasol CFB reactors in Secunda with fixed fluidized bed reactor (FFB), better known as SAS (Sasol Advance Synthol) reactors.

2.5.1.2 SAS - Sasol Advance Synthol reactor

The turbulent or fluidized-fixed-bed reactors (FFB) have been largely optimized by Sasol in its FT plants since 1950' s to nowadays. The fixed fluidized bed reactor first developed by Sasol exhibited very high rates of heat exchange due to the high degree of turbulence achieved. This means that this type of reactors could cope with large amounts of heat released at high conversions. Moreover turbulent flow regime leads to uniformity of the temperature across the reactor.

Main issue concerning the operation of such type of reactors lies in the limit of the selectivity that can be obtained: the process conditions must be such that the selectivity of long chain hydrocarbons is limited to ensure that excessive condensation of liquid within the catalyst pores does not cause agglomeration of the particles and subsequent bed de-fluidization.

Since the first SAS reactor came online in 1984 there was an intensive replacement of older CFB reactors with SAS reactors. There are many reasons that explain that:

- The construction cost of SAS technology is 40 % lower, mainly because the reactor volumes are smaller: the SAS reactor volume is of the same order of the settling hopper of CFB reactors; moreover, the support structure for SAS reactors only cost about 5 % of the support structure for CFB. This makes it possible to increase the reaction volume [Steynberg et al., 2004].
- Wider reaction volumes make it possible to install more cooling coils and thus increase their capacity. Therefore more syngas can be fed or pressure can be increased at fixed linear velocities.
- All of the catalyst charge participates to the FT synthesis during SAS operation, while half of charge is involved at any time in CFB reactors.
- Since there is no standpipe for catalyst injection there is any limitation on catalyst loading (i.e. upper limits for conversion) with time on stream for SAS reactors.
- The gas and catalyst linear velocities are much lower for SAS reactors than for CFB, thus the operating costs linked to gas compression are sensibly lower. Moreover, lower gas velocities don' t allow abrasion mechanism to occur along the reactor section wall, a typical issue for CFB reactors. Because of this CFB reactor section walls are ceramic lined and a regular maintenance is mandatory.

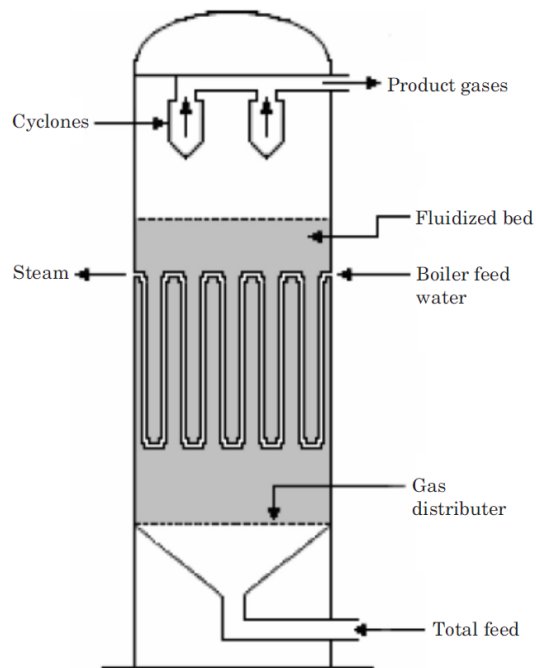


Figure 2.6: Sasol Advanced Synthol (SAS) reactor [Nawaz et al., 2015].

2.5.2 LTFT reactors

Low-temperature FT mode of operation results very different from HTFT applications due to different production targets. Actually the presence of a liquid phase within the mass and heat exchange zone results in a different hydrodynamic and heat transfer behavior and require different features to LTFT reactors compared to HTFT ones for optimal performance. The major classes of reactors commercially used at industrial scale for LTFT applications are represented in (Fig. 2.5).

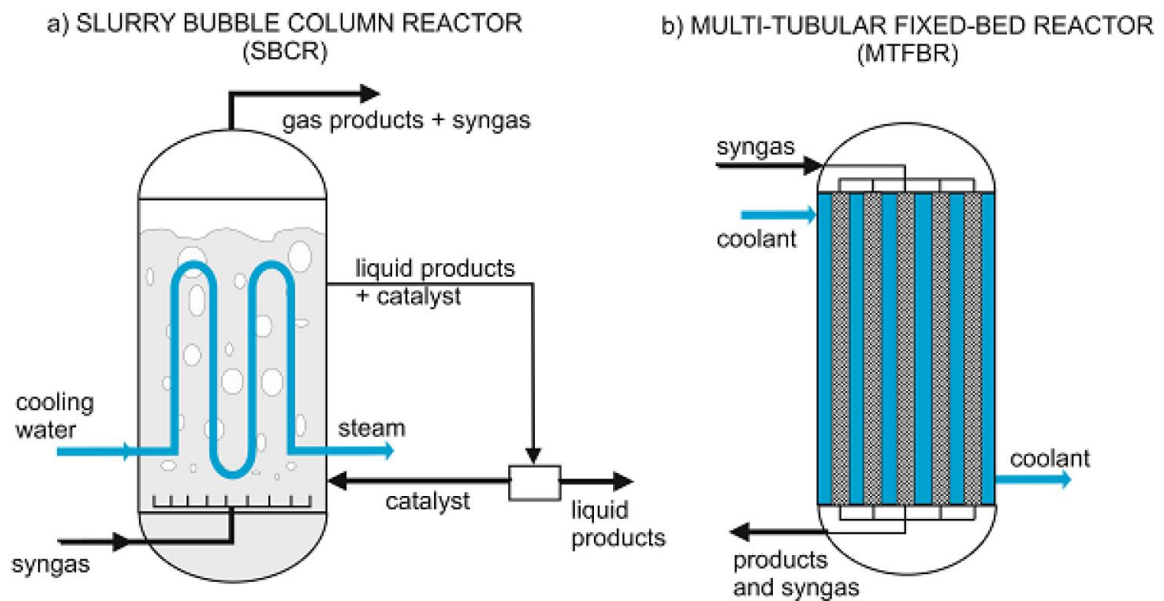


Figure 2.7: commercially used industrial reactor types for LTFT modes of operation: a) slurry-bubble-column reactor; b) multi-tubular-fixed-bed reactor [Todic et al., 2013].

2.5.2.1 MTFB - Multi-tubular-fixed-bed reactor

Multi-tubular-fixed-bed (MTFB) reactors are the most often used as commercial FTS reactors. These reactors consist of several hundred to well over ten thousand tubes, with 2 to 5 cm diameters. The tubes are wall-coated with catalyst particles which are not allowed to move from the wall (fixed-bed). The use of such narrow tubes, coupled with turbulent fluid flow, allows for high transfer coefficients [Steynberg et al., 2004].

Either iron or cobalt can be used but size for iron-based MTFB tubes can be increased up to 5 cm diameter, since iron is less active and then produce less heat than cobalt; instead, narrower tubes are necessary when more active cobalt is used at the aim to ensure good heat transfer between the packed bed and the cooling fluid.

Moreover high linear gas velocities are generally applied to generate a turbulent flow regime improving the heat transfer rate. At this aim a part of unreacted gases and light products (tail gas) is usually recycled into the reactor [Todic et al., 2013].

However simultaneous application of narrow tubes, high linear gas velocities and small particles (for enhancing mass transfer coefficients) inevitably result in unacceptable pressure drops over the reactor which heavily influence the compression cost.

This implies that catalyst particles used in such a reactor are larger than for slurry reactors, ranging from 1 to 3 mm. It is generally known that particles larger than 0.2 mm exhibit mass transfer difficulties [Khodakov et al., 2007]. The use of large particles means that a part of the catalyst activity is sacrificed in order to maintain acceptable pressure drops across the reactor [Todic et al., 2013].

In a MTFB reactor the syngas enters from the top and reacts along the reactor within the pores of the catalyst pack which is fixed to the wall of the tube. The liquid phase produced (i.e. wax) easily runs down the tube walls and it is collected at the bottom [Dry et al., 2010]. The hydrodynamic feature of the flow generate notable gradients along the reactor (axial gradient), especially when iron catalyst is used. The rate of FT reactions decrease more rapidly along the reactor length than in the case of cobalt since iron is much less active so that only a portion of reactor operate at optimal temperature, the other sections being at higher or lower temperatures.

The main drawback for this type of reactors is their cost. Indeed, such a complex assembling of many narrow tubes has a great impact on the capital cost for a MTFB FT plant [de Klerk, 2013].

However it has many key advantages that justify its adoption:

- Robustness and reliability: it is the reactor type with the longest proven history of stable and reliable FT operation [Selvatico et al., 2016].
- Easy to scale-up: MTFB reactors can be studied actually as multiple single-tube stage in parallel without any reasonable loss of similarity of the hydrodynamic and temperature profile.
- Higher conversion due to the plug flow tendency.
- No catalyst loss due to attrition.
- Longer catalyst life due to lower susceptibility to poison.

The multi-tubular-fixed-bed is largely employed by Shell in SMDS (Shell-Middle-Distillate-Synthesis) process technology at Pearl GTL plant facility (Las Raffan, Qatar) and in smaller FT plants in Bintulu (Malaysia) [de Klerk, 2013].

2.5.2.2 SBC - Slurry bubble column reactor

The SBCR consists of a vertical column filled up to a certain level of liquid hydrocarbons (i.e. wax) in which a finely divided catalyst is suspended by gas bubbling up through the slurry at a rapid rate leading to turbulent flow behavior with effective mixing of the liquid phase and small bubbles, and plug flow of large, fast rising bubbles [de Swart et al.,1997]. Reactant gas enters from the bottom at high flow rate so that buoyancy-enhanced mixing effect made unnecessary mechanical mixing. The product gas exits at the top, whereas the catalyst/wax mixture is drawn out from aside of the reactor.

Catalyst is continuously removed from the liquid outlet stream, separated from products and recycled back to the inlet of the reactor.

Clearly catalyst is not stationary during operation and collision between particles and the cooling coil walls are frequent. This implies that catalyst must be resistant to attrition and thus must own good mechanical features.

Moreover catalyst particle size doesn't affect the differential pressure profile over the slurry reaction zone as in the case of MTFB reactors. Pressure drops across the reactor are determined only by the hydrostatic height (i.e. density and height) of the slurry phase and not the particle size.

Particle size is crucial rather when designing the catalyst-product separation system. Actually catalyst-product separation is a key challenge in slurry-bubble-column reactor design for industrial applications [de Klerk, 2013]. The catalyst size turns to be a compromise between activity and ease of suspension, which benefits from smaller particles, and catalyst-product separation system, which benefits from larger particles [de Klerk, 2013].

The main advantage of slurry bubble column reactor lies in the intrinsic better temperature control because of closeness to CSTR (Continuous-Flow-Stirred-Tank reactor) model essential.

But there are other nice features coming from Sasol experience which makes propending for SBCR over MTFBR:

- (i) capital cost are notably lower because construction is simpler;
- (i) better heat transfer coefficient and easier temperature control;
- (ii) lower mass transfer resistance;
- (iii) higher productivity, due to more catalyst loading per reactor volume and thus higher reaction rate per volume;

- (ii) pressure drops are lower;
- (iii) maintenance cost are reduced;
- (iv) replacement of the catalyst occurs on-line (without shutdown) while MTFB reactors shows inability to replace catalyst without shutdown the system.

The first studies on the slurry phase reactor technology was conducted by Fischer in 1932 but optimization and intensive scale-up were not applied because of the critical catalyst-wax separation issue. It was only in the 90' s that Sasol succeeded to find a suitable separation system for catalyst-wax mixtures promoting the scale-up of slurry bubble reactor. The innovative reactor came online in 1993. The technology was named SSPD (Sasol-Slurry-Phase-Distillate reactor) and showed much better productivity and capacity features than the MTFB ARGE (Sasol fixed-bed-reactors).

The technology was then re-adapted to the use with supported Cobalt-base catalyst and the process was recognized as Cobalt Sasol Slurry Bubble Process (Co-SSBP). Actually Co-SSBP is the base reactor technology for FT synthesis in the Orix GTL plant (Ras Laffan, Qatar).

2.5.3 Micro-reactors

As early as 90' s, different strategies have been proposed to overcome the main issues concerning the operation of the conventional FT reactors seen before (i.e. mass and heat transfer).

Paturzo et al. proposed the development of innovative reactors, also known as micro-reactors [Paturzo et al., 2002]. Micro-reactors represent the reactors with characteristic dimension (diameter of channel tubes) 1 to 2 orders of magnitude smaller than conventional FT reactors. This feature greatly improves heat and mass transfer, allowing for a correct temperature control within the catalyst bed, which leads to lower methane selectivity and higher productivity per reactor volume.

There are different types of micro-reactors available:

- Micro-structured reactors (or monolith reactors);
- Micro-channel reactors;
- Micro- and milli-fixed-bed reactors.

All of the aforementioned classes of micro-reactors present two common features: first they show enhanced heat transfer compared to conventional reactors, so that more active catalyst with higher productivity can be used. Besides, they present regular spatial structures, allowing for a simplification of fluid behaviour and therefore a better control of heat, mass and momentum transport phenomena [Todic et al., 2013; Moulijn et al., 2011].

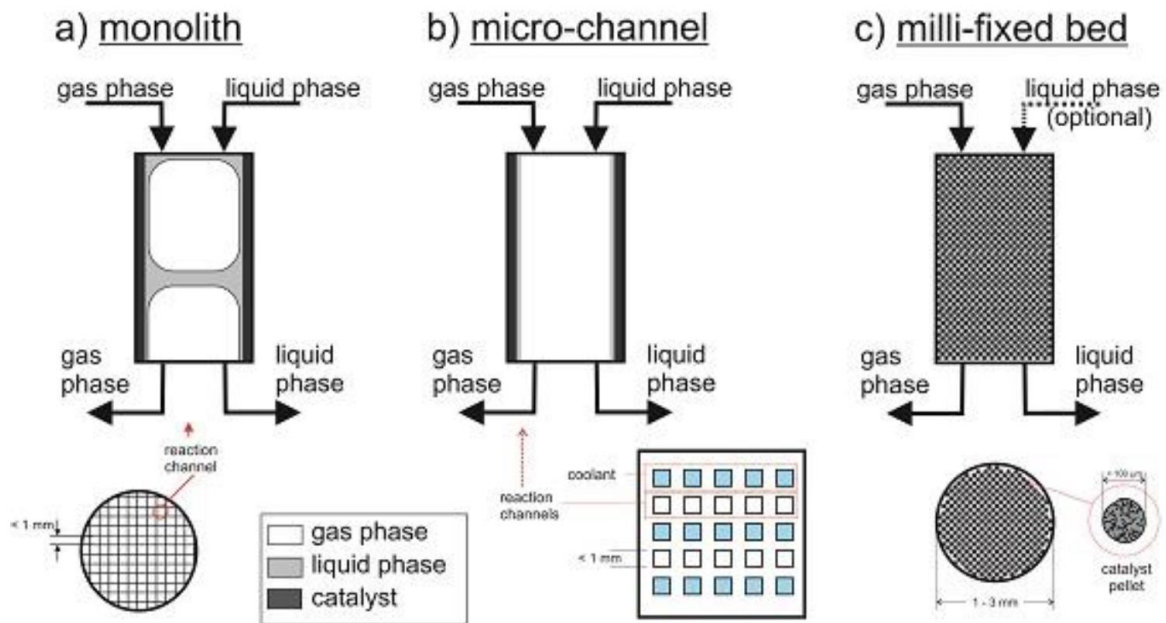


Figure 3.8: micro-reactors for FT synthesis applications (longitudinal section and flow pattern); a) micro-structured catalyst (i.e. monolith) reactor; b) micro-channel reactor; c) micro- or milli-fixed-bed reactor. [Todic et al., 2013]

Main difference between them concern the way in which catalyst is placed inside the reactor.

Monolith reactors consist of a structured support, such as a honeycomb monolith, coated with a thin layer (40-50 μm) of active catalyst (Fig. 2.8a). Efficient mass and heat transfer phenomena within such a type of reactor are achieved by means of particular fluid flow behaviour, also known as Taylor flow [Kreutzer et al., 2005]. It consists of elongated gas bubbles, whose typical equivalent diameter is significantly larger than that of channel diameter separated from thin layer of liquid, which separates gas from the catalyst layer also. This ensures mass transfer resistance between reactants and catalyst pores of the same order of that for slurry reactors but requires high liquid flow rates, making high

recycle ratios mandatory. For the same reason the heat transfer coefficients result very high, several order higher than that for conventional fixed-bed configurations.

In particular, according to Guettel and Turek, monolith reactors appear to perform better than slurry-bubble-column reactors because catalyst show the same productivity per reactor volume without requiring on-line catalyst separation from the liquid that is still a challenge for SBC reactors [Guettel et al., 2009]. On the contrary, a monolith reactor still is not industrially attractive because the thin layer of catalyst applied to the reactor wall does not allow for enough catalyst mass per reactor volume (i.e. activity per reactor volume), seriously affecting the volumetric yield of the reactor [Saeidi et al., 2015].

Micro-channel reactor design is very similar to that of monolith reactors: they consist of many parallel rectangular channels, which are coated with a thin layer of active catalyst, except that the cooling fluid flows through uncoated channel rows (Fig. 2.8b). This attribute allows for sorting them into blocks, leading to a modularity approach with all related benefits, such as the possibility to realize economies of scale at much smaller size (500 bpd) than conventional reactors (10000bpd) [Saeidi et al., 2015] and to minimize downtime due to catalyst replacement (replacing only few modules at the time).

Like the monolith reactors, they offer high surface area-to-volume ratio that allows for high mass and heat transfer coefficients. However, also in this case, the very low catalyst mass-to-reactor volume ratio leads to lower value of productivity for industrial scale. In that respect Oxford Catalyst Group [Wang et al., 2003] and Velocys [Jarosch et al., 2011] have developed a new generation of highly active catalyst that could be applied efficiently in micro-channel configurations for improving volumetric productivity. Moreover, Jarosch et al. reported methane selectivity for these reactors at about 9 %, which is similar to that for slurry bubble column reactors and better than micro-structured (monolith) reactors.

In order to overcome the monolith and micro-channel disadvantages, related to low productivities and complex and expensive catalyst manufacture and loading (i.e. coating), some researchers have studied the possibility of using milli- and micro-fixed-bed reactors. In this type of reactors sufficiently small catalyst particles are loaded into the packed bed, allowing for micro-scale flow characteristics (Fig. 2.8c). This allows for holding all the benefits of micro-reactors, such as mass and heat transfer efficiency and achieving, at the same time, high catalyst mass per cubic meter of reactor as in the case of conventional fixed-bed reactors [Chambrey et al., 2011]. Moreover, micro- and milli-fixed-bed reactors

allow for simplifying the catalyst loading and replacement procedures, which can represent a serious issue for monolith and micro-channel reactors. Unlike the micro-channel reactors, this type of reactors can be loaded with tried and proven catalyst, without the need for specially designed catalysts for coating [Chambrey et al., 2011].

The main issue concerning milli- and micro-fixed-bed configuration is predictable: the very high pressure drop along the reactors due to the loading with small particles. However, it has been demonstrated that using catalyst pellets as small as 100 μm [Knochen et al., 2010; Todici et al., 2013] helps to achieve acceptable pressure drops, while keeping high the catalyst activity. Moreover, the diameter of tubes can be in the order of millimetres, simplifying the construction and loading (or replacement) procedures of the catalyst.

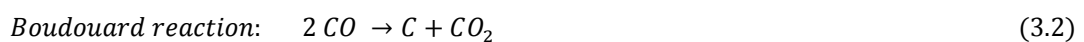
3. FISCHER TROPSCH SYNTHESIS

The Fischer-Tropsch collectively refers to processes for the conversion of synthetic gas to synthetic crude oil (syncrude), whose composition and quality are greatly influenced by catalyst type and synthesis conditions.

The Fischer-Tropsch synthesis can be oversimplified representing the conversion of syngas mixture into the basic monomer constituting the long chain of the FT products [Sie et al., 1999]:

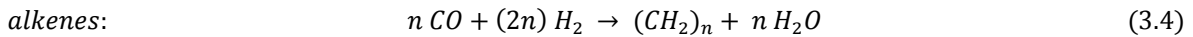
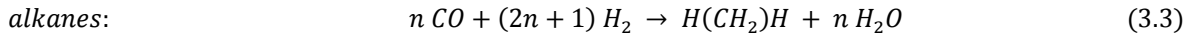


As can be noted, FT synthesis is a high exothermic process and the above value may give a first idea of how much heat is released during the synthesis. It is reported that an amount of 20-25 % of the calorific values of syngas would be lost during conversion [de Klerk, 2013]. Therefore, the heat generated by the reaction needs to be rapidly removed in order to avoid temperature increases which would result in the undesired formation of high levels of unwanted methane and light hydrocarbons. And in extreme cases, high temperatures can lead to catalyst deactivation due to sintering and coking and catalyst disintegration due to Boudouard carbon deposition (equation (3.2)) over active metal site [Dry, 1982].



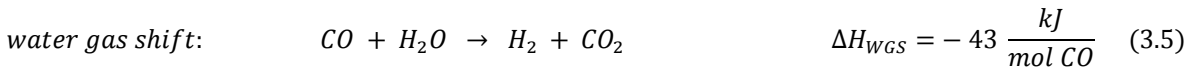
The high exothermicity of the process poses a serious challenge to the development of nearly-isotherm reactors. This is not followed by similar process in the crude oil refining industry where the heat released in catalyzed process is about one magnitude lower [Steynberg et al., 2004]. Another important aspect relates to water formation: about one half of the converted hydrogen comes to bind to the oxygen molecule brought from carbon monoxide, producing large amount of water.

Actually the Fischer-Tropsch product spectrum consists of a multicomponent mixture of aliphatic (mostly linear) hydrocarbons together with oxygenated products from side reactions. Main products are linear paraffins and α -olefins. In its simplest form, the main reactions during FT-synthesis are represented in the following equations:



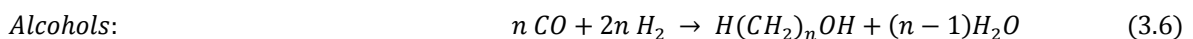
Reaction (3.3) and (3.4) are related to the production of primary FT products: linear paraffins and linear olefins.

The reactions of FT synthesis on iron catalyst can be described as a combination of the above equations plus the water gas shift (WGS) reaction:

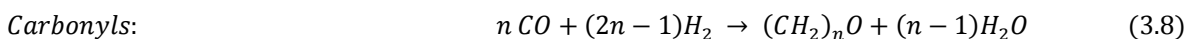
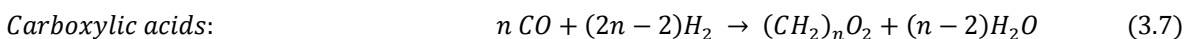


The WGS activity depends on catalyst properties and reaction conditions. It can result much higher over potassium-promoted iron catalyst compared to cobalt catalyst. The WGS reaction has profound effect on the reaction stoichiometry. For instance Fe based catalysts should use H_2/CO ratios smaller than 2 and WGS can balance the reactant stoichiometric requirements for FT synthesis. However the actual rate of water gas shift depends also on operating conditions, in particular on temperature. For high temperature (300-350 °C) operation mode (HTFT) using Fe based catalysts, WGS proceeds to equilibrium and can contribute to the formation of hydrocarbons. In this case, about 30 % of CO is converted to CO₂ due to WGS reaction [Feimer et al., 1981]. At lower temperature (180-250 °C), i.e. in LTFT operation mode, WGS proceeds below equilibrium but significant CO₂ formation can also occur.

During FT synthesis alcohols can also be formed either as by-products or as main products depending on the catalytically active metals and pressure:



Among organic oxygenates produced during FT synthesis, alcohols content, especially low carbon number alcohols, is considerably higher than that of carboxylic acids or carbonyls (aldehydes and ketones), so formed:



Alcohols and oxygenates are mainly formed at low temperatures in the presence of cobalt as active metal, whereas carbonyls are formed at more severe operating conditions and are mainly found during HTFT synthesis.

Anyway, besides the influence of temperature and thus of the operating mode, the product stream from FT reactors depends primarily on the catalyst selected. Therefore following are described the differences between catalysts commonly selected for FT synthesis drawing attention to their properties (selectivity, activity, stability and mechanical robustness) and on how the preparation pathway plays a fundamental role for their determination.

3.1 FT catalysts

Metals known to have sufficient activity to be considered for commercial application in the FT synthesis mainly include iron, cobalt, ruthenium and nickel.

The availability of Ruthenium, the most active of them, is limited and thus it is very expensive. Also Nickel is very active but being a more powerful hydrogenating catalyst it produces too much methane. Moreover at high pressures commonly involved in FT synthesis Nickel forms volatile carbonyls and thus it is slowly lost from the reactors [Dry, 2008]. This leaves only Fe- and Co- based catalysts as the only practical catalysts. On a metal basis the approximate relative cost of Fe:Co:Ni:Ru is 1:250-1000:150:50000-138000 (Fig. 3.1).

Fe	Co	Ni	Ru
M ¹ : 55.847	M ¹ : 58.9332	M ¹ : 58.69	M ¹ : 101.07
Rp ² : 1	Rp ² : 235	Rp ² : 140	Rp ² : 76 000
A ³ : 1	A ³ : 250	A ³ : 150	A ³ : 138 000

1. Molar mass [g/mol].
2. Retail price (2007) compared to iron.
3. Activity per unit surface over the lifetime in relation to iron.

Figure 3.1: active metals commercially available for FT synthesis applications [Dry, 2001].

Iron generally produces more olefins and oxygenates than cobalt (i.e. a less hydrogenated product spectrum) which may be related to the lower hydrogenating ability of iron. Moreover, there are identified various active phases for iron catalysts, which, under FT conditions transforms into a complex mixture of iron carbides (Fe_xC_y) and oxides [Dry et al., 1990; de Smith et al., 2008]. While cobalt-based catalysts only have an active phase, which matches the metallic phase.

By-products of FT synthesis are generated by the way in which oxygen from CO is removed and an important distinction between cobalt and iron catalysts is related to the formation of oxygenates. Actually with cobalt catalysts oxygen is almost entirely removed under the form of water, whereas the high activity of iron for WGS leads to the remove of oxygen also as CO_2 . Iron is known for being considerably active towards WGS and that is the reason why it is preferred in the case of syngas feed with a low H_2/CO ratio, such as that generally obtained from coal derived syngas. Instead, the low propensity of cobalt catalysts for WGS makes them the preferred catalysts for GTL applications, since the H_2/CO ratio of syngas derived from natural gas is already close or above the usage ratio. The usage ratio (UR) is the net amount of hydrogen converted divided by the carbon monoxide converted. At one extreme, where no WGS reaction takes place, the usage ratio is only determined by the FT reaction and assumes a value of around 2. In the other extreme, where almost all water is converted to CO_2 , the usage ratio tends to a value of 0.5 [Loosdrecht et al., 2013]. First value (UR=2) is encountered when measuring the usage ratio for cobalt based synthesis whereas usage ratio obtained from iron based processes reaches very low values (down to 0.5).

3.1.1 Iron-based catalyst

Iron-based catalysts were first commercially applied by Sasol since the 1950 [Steynberg et al., 2004]. There are several reasons for which iron is more advantageous than cobalt for certain modes of operating FT synthesis:

- iron is cheaper than cobalt by a factor of 200-250;
- iron is known to be more tolerant to poison than cobalt, especially for the Sulphur and Sulphur compounds (H_2S) in the synthesis gas;
- iron is much more versatile than cobalt, in the sense that its selectivity can be manipulated either by addition of promoters (more responsive) or by varying

operating parameters, such as temperature, pressure and H₂/CO ratio (less responsive).

Iron-based catalysts are usually prepared in the 'bulk' form and there are several techniques for its preparation. Besides activity, stability, selectivity (low for methane and higher for longer chain hydrocarbons) and life-cycle also the operating mode (HTFT or LTFT) and the type of reactor employed require a suitable preparation procedure [Loosdrecht et al., 2013].

In particular, whenever the catalyst is used in HTFT processes, it is prepared by *fusion* of magnetite (Fe₃O₄) with small amounts of promoters. While LTFT iron catalyst is made by *precipitation* and the high area oxide is tied with silica gel and promoted with alkali [Dry, 1981].

During fusion or precipitation, iron oxides (e.g. hematite (Fe₂O₃) and magnetite (Fe₃O₄)) are produced and these are then activated forming α-Fe or iron carbides (activation process) [Loosdrecht et al., 2013].

Fusion produces iron oxide particles of low surface area, high density, and high strength, which are ideally suited for application in circulating fluidized bed reactors [Davis, 2003]. Iron-based catalyst from fusion results an intimate mix of fused iron oxides and promoters, with high mechanical qualities.

<i>Reactor</i>	<i>Important catalyst properties</i>	<i>Raw material</i>	<i>Synthesis method</i>
HTFT Circulating or fixed fluidized bed reactors, 320–350 °C	Low surface area (<10 g m ⁻²), high density, high strength	Mill scale	Fusion followed by crushing and milling
LTFT Tubular fixed bed reactor, 220–250 °C	High surface area, sufficient strength	Fe(NO ₃) ₃ and silica source	Precipitation followed by extrusion/shaping
Slurry bed reactors, 220–250 °C	High surface area, small particles (50–250 μm)	Fe(NO ₃) ₃ and silica source	Precipitation followed by spray drying and calcination

Figure 3.2: different preparation procedure for low-temperature and high-temperature based Fischer-Tropsch processes [Loosdrecht et al., 2013].

In the precipitation procedure, commonly applied for LTFT iron-based catalysts, the iron-based catalyst result from precipitation of iron hydroxide from an iron-nitrate salt and successive impregnation with structural promoters.

Structural promoters, such as Si, Al, and Mg, are necessary to suppress sintering, stabilize the active phase and also improve mechanical strength [Loosdrecht et al., 2013]. However they make reduction (activation) of the catalyst more difficult due to the formation of iron silicates and aluminates.

Fortunately chemical promoters, such as Cu or Ag, can be added to increase the rate of reduction, compensating for the adverse effect of the structural promoters. Chemical promoters are primarily added for several reasons, among them (i) for improving nucleation of iron intermediates which leads to higher surface areas, (ii) for increasing the number/types of CO adsorption sites, (iii) for stabilizing the active phase and (iv) for reducing the rate of secondary reactions [Loosdrecht et al., 2013].

In particular the addition of alkali-metals, such as potassium, is known for enhancing the chain growth probability (improving C₅₊ selectivity), reducing the selectivity for methane and inhibit the secondary hydrogenation of the olefins, leading to higher olefin to paraffin ratios [Loosdrecht et al., 2013].

After catalyst precursors has been prepared and shaped, activation is the next step. Activation is a necessary step to transform (by reduction) iron oxides and (oxy) hydroxide, which are inactive for FTS, into active phases for FTS. Depending on the operating mode – HTFT or LTFT – and iron oxide precursor (for example magnetite or hematite), activation is carried out under hydrogen, carbon monoxide or synthesis gas atmospheres.

Activation in hydrogen typically leads to the formation of reduced iron oxides (FeO) and of a metallic phase (α -Fe). In particular the magnetite from fusion preparation (for HTFT applications) is typically reduced with hydrogen. This also leads to an increase in surface area from $< 1 \text{ m}^2/\text{g}$ to $5\text{-}8 \text{ m}^2/\text{g}$ [Dry, 1981].

Instead activation with CO leads to a mixture of metallic iron (α -Fe), iron carbides (Fe_xC_y) and magnetite (Fe_3O_4) and it is preferred for precipitated iron to be used in LTFT applications, because treatment of precursors with carbon monoxide gives the best syngas conversion and lowest methane selectivity compared to catalysts activated with hydrogen [Loosdrecht et al., 2013].

Iron is less preferred from an activity and life-cycle point of view, due to its propensity to quickly deactivate (activity or selectivity loss). Actually, iron catalysts show a considerable loss of performance over time.

The following main reasons have been identified for the deactivation of iron-based catalysts [Loosdrecht et al., 2013]:

- buildup of 'free' carbon, due to Boudouard reaction, improved at high temperature and pressure;
- activity loss caused by transformation of the phase, i.e. from carbides to oxides;
- mechanical break-up of the bulk phase;
- deposition of poisons on the surface of catalyst;
- sintering (agglomeration of finer particles).

In particular iron employed for HTFT application is subjected to the formation of 'free' carbon on its surface, making catalyst particles less dense and strength and results in catalyst bed expansion, particle break-up and carry-over of finer particles into the downstream process [Loosdrecht et al., 2013]. Sasol has developed a suitable approach to face deactivation, adding chromium as chemical promoter that also reduces the 'free' carbon formation during FT synthesis [Bromfield et al., 2005; Loosdrecht et al., 2013].

The formation of 'free' carbon is less likely onto precipitated iron surface typically used in LTFT synthesis. Effectively, low temperature FTS conditions inhibit carbon formation. Main proponents for deactivation issues for LTFT iron-based catalyst are sintering and oxidation of the active phase. The highly dispersed iron particles (average size of 2nm) in the form of magnetite, typical of low-temperature FT synthesis, can either react in syngas to the required iron carbide or sinter into larger inactive particles, which can further agglomerate to large inactive globules (of about 400 nm size) [van Steen et al., 2008; Loosdrecht et al. 2013].

3.1.2 Cobalt-based catalyst

Cobalt catalysts are exclusively used for low-temperature synthesis or into LTFT reactors because cobalt would only produce methane at the high temperatures (300-350 °C) commonly applied in HTFT processes.

Cobalt FTS catalysts are currently commercially operated in slurry-bed reactors by Sasol/QP in the Oryx GTL plant in Qatar whereas fixed-bed reactor solution has been

employed by Shell in the SMDS plant in Malaysia (Bintulu) and in the Pearl GTL plant in Qatar [Loosdrecht et al. 2013].

Cobalt catalysts utilized by many companies, such as BP, Conoco Philips, Gulf, Exxon Mobile generally show about similar composition [Loosdrecht et al., 2013] and a schematic composition of a typical Co-based catalyst is depicted in (Fig. 3.1):

1. *metallic cobalt* phase as FTS active metal (typically 10-30 %); metallic cobalt is considered the only active phase for FTS and, being costly, its use has to be maximized; hence it is mandatory that there is a large number of metal sites available for unit catalyst surface area. At this purpose cobalt is well milled and dispersed on a strength and large surface (porous) material, namely working as a structural support. Typically, cobalt particle size is limited to just above 8-10 nm because particles below those have shown to have a lower turn-over-frequency (TOF), i.e. the FT reaction rate per unit surface area [Bezemer et al., 2006; Loosdrecht et al., 2013]. Moreover very small particles (4-6 nm) are more likely to experience sintering and can also form strictly bonded metallic-support compounds which are very difficult to reduce and result inactive for FTS [Loosdrecht et al., 2013]. At the aim to face this issue cobalt catalyst are promoted with a second metal.
2. A *second metal* (usually noble), such as Pt, Re, or Ru at low concentrations (0.05 - 1 %); as just mentioned the use of a second metal close to the cobalt particle favors the hydrogenation of the cobalt catalyst precursor (cobalt oxide), also when it is chemically bonded to the support, facilitating the reduction step. Moreover a metal promoter can improve catalyst activity because it is believed to enable nucleation, which leads to a small average size of either cobalt oxide or cobalt metal particles [Diehl et al., 2009; Loosdrecht et al., 2013].
3. A *structural (oxidic) promoter* (e.g. Zr, Si and La) (1 - 10 %); structural promoters affect the formation of the metallic (FT active) phase of the cobalt catalyst in a way that favors catalyst activity. At this regard promotion of Co/Si or Co/Al catalysts with Zr has been shown to decrease the cobalt-support interactions, which further make reduction simpler and increase in the number of metallic phases on the surface [Feller et al., 1999; Khodakov et al., 2007]. Moreover incorporation of B and Ni as structural promoters has been proved to inhibit carbon deposition, thus increasing the stability of the active phase of the catalyst. [Tan et al., 2011; Rytter et al., 2010].
4. A stable refractory (oxidized) *support* (e.g. Al₂O₃, TiO₂, SiO₂, ZnO) for the remainder amount; the properties of the support are an important factor helping to increase the

stability in different ways, while facilitate high cobalt dispersion (increasing the activity).

The support is more robust than the metallic phase and this surely improves the mechanical strength of the catalyst under harsh FTS operating conditions, such as at high conversion operation when water partial pressure can reach several bars. Actually un-protected catalysts were found to be susceptible to hydrothermal attack during realistic FTS conditions, which leads to a decrease of stability but mainly results in contamination of products with ultra-fine, cobalt rich particles. At this regards TiO_2 supports have been proved to have higher hydrothermal stability and resistance to high water partial pressures [Loosdrecht et al., 2013].

Obviously the support material should have high surface area for promoting high dispersion of nanometer cobalt particles. For alumina (Al_2O_3) surface area of about 150 – 250 m^2/g is required [Beuther et al., 1986].

Lastly, especially when applied into slurry-bubble column reactors, the catalyst should prove to be resistant to attrition. At this purpose, cobalt-alumina catalysts have shown to have more capacity than silica and titanium supported.

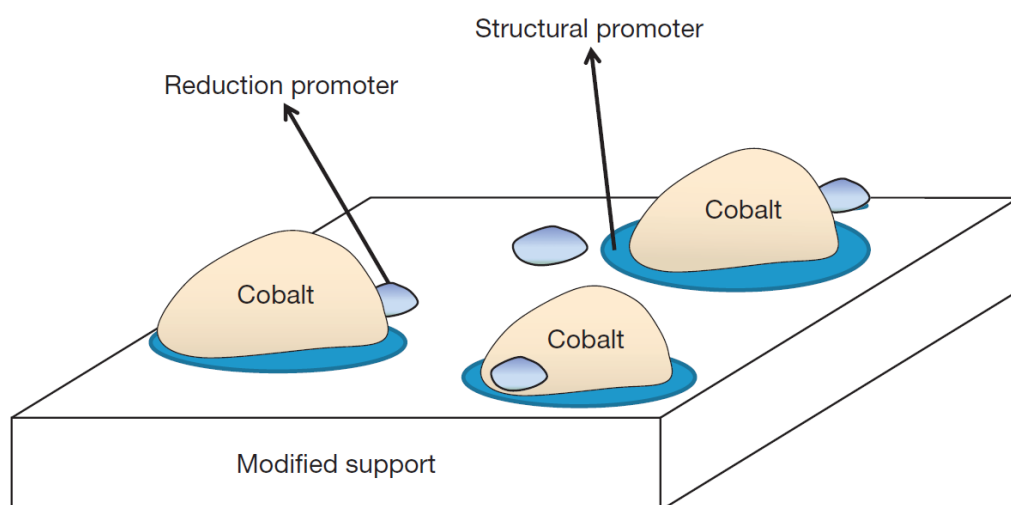


Figure 3.2: schematic representation of typical Cobalt based catalyst composition [Loosdrecht et al., 2013].

The optimal crystallite size distribution of cobalt particles is achieved through a specific preparation process.

The optimal size of cobalt-catalyst precursor is greatly dependent on the type of reactors used. In particular fixed-bed reactors require larger particles due to a pressure duty

constrain. Instead both slurry-bubble column and micro-channel reactors accept smaller catalyst particles but each of them foresees a different shaping. Therefore, depending on type of reactor, various methods of preparation exist.

Anyway, irrespective of the type of reactor within catalyst is applied the method of preparation should guarantee the minimization of the poisons, such as S, Na and Cl.

The principal procedures for preparing cobalt-based FT catalyst precursors are:

- *co-precipitation* of cobalt, promoters and supports, followed by catalyst particle shaping;
- *impregnation* of cobalt (oxide or metal) and promoters onto pre-shaped support particles.

However, there is little understanding regarding the influence of particle-size effect on both activity and selectivity. As aforementioned, it is well accepted that for catalysts with cobalt crystals above 10 nm the TOF (turn-over-frequency), that is the common unit for measuring activity of heterogeneous catalysts, is structure insensitive. Instead there is a sharp decrease in activity for particles smaller than 8-10 nm [Xiong et al., 2011].

With regards to the impact of particle-size of the cobalt crystals on selectivity, it seems more gradual and does not level off above 10 nm. Most studies have shown a gradual increase of chain growth probability (and better C5+ selectivity) increasing the cobalt crystal diameter from very low values (4-5 nm) to up 15-20 nm [Xiong et al., 2011]. Thereafter selectivity seems not to vary no more increasing the particle size up to 200 nm (the limit value for intra-particle mass resistance for cobalt catalysts). However, it is well-known that selectivity for higher hydrocarbons depends strongly on FTS conditions (temperature, pressure and reactant feed ratio) rather than particle-size of the cobalt particles.

After shaping and drying, the catalyst needs to be activated, or in other words the oxygen or hydroxyl group has to be removed from the precursor. At this scope cobalt catalysts are reduced in hydrogen or a dilute hydrogen atmosphere. Usually CO is not used due to the related risk of carbon formation at the temperatures involved during reduction. Reduction of cobalt oxide to cobalt metals occur in two exothermic steps:



The maximum temperature required for reduction of cobalt catalysts strictly depends on the level of reduction promoter (Pt, Ru, Re, Pd), but also on the presence of other promoters (e.g. alkali metals makes reduction more difficult) and the support used for the preparation step [Loosdrecht et al., 2013]. Not enough amounts of reduction promoters or certain type of supports (e.g. silica) could favor high reduction temperatures that are deleterious for catalyst activity and stability due to sintering promoting effect and loss of metal surface area.

Activity and selectivity of cobalt catalyst not only depends on the catalyst itself but both are greatly affected by operating conditions applied. For example high water partial pressures typical of high conversion level can induce modifications of the atom surface layer of the cobalt crystals, reducing the activity of the active surface; also sintering and carbon deposition are favored by high water partial pressures and this adverse the stability of the catalyst.

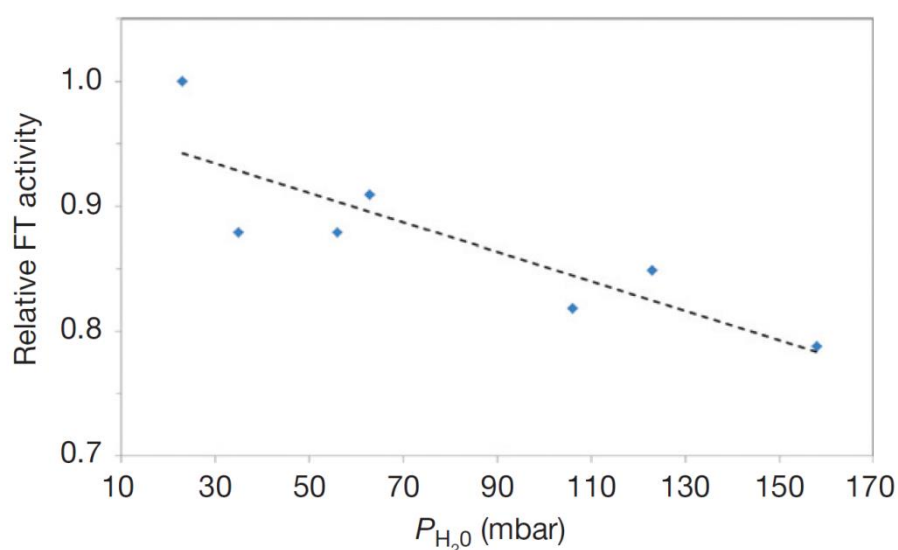


Figure 3.3: impact of water partial pressure of a cobalt-alumina based catalyst during FT performance [Loosdrecht et al., 2013]

Catalyst stability represents a fundamental issue for the economics of cobalt-based FT process. The loss of activity under commercially relevant FTS conditions (i.e. deactivation) typical of cobalt catalyst is initially stronger, after which it starts levelling off [Saib et al.,

2006]. Currently it is believed that only the so-called B5 sites on metallic cobalt play the role of active sites for FT synthesis. Hence, changes to the number or nature of these sites could favor deactivation [Loosdrecht et al., 2013].

The main deactivation mechanisms of cobalt FTS catalysts and its active sites are listed following:

- oxidation; in particular oxidation of cobalt surface by the product water was seen as the major deactivation mechanism in the open literature over the last 20 years. However, more recently, in-depth studies of molecular modelling combined with real catalyst studies under industrial FT conditions have proved that Co crystallites with a diameter above 2 nm do not withstand oxidation and in fact they are further reduced during FT synthesis [Saib et al., 2006; Loosdrecht et al., 2013];
- mixed metal-support interaction; although thermodynamically favored at FTS conditions, this deactivation mechanism has been gradually ruled out since the metal-support reaction needs CoO formation as intermediate, which does not take place during the FT synthesis [Loosdrecht et al., 2013];
- carbon deposition; deleterious carbon arising from CO (i.e. Boudouard reactions) and FT products (long chain hydrocarbons, i.e. wax) can cause the blockage of pores, resulting in mass transfer limitations, formation of bulk and surface carbides and blockage or alteration of active sites (B5 sites) [Loosdrecht et al., 2013]. Differently from the aforementioned deactivation mechanisms, pore blockage is generally accepted as deactivation mechanism. Fortunately it has also been proved that carbon deposition can be decreased by adding promoters, such as ruthenium [Iglesia et al., 1993] and boron [Tan et al., 2011];
- sintering; as the previously mentioned mechanism, also sintering is a thermodynamically driven process and it has a major role in the FT synthesis catalyst deactivation. According to this mechanism smaller, more unstable particles grow to form larger, more stable particles which have lower surface energy [Loosdrecht et al., 2013]. Crucial factors starting this deleterious mechanism are temperature and water partial pressure, i.e. an increase in either of them can boost sintering. Also the choice of support plays a key role; in particular alumina supports are much less affected by metal-support interactions than silica-supports: lower metal-support interactions mean less migration and probability of coalescence between cobalt particles [Loosdrecht et al., 2013];
- poisoning by S, NH₃, HCN, Hg and Cl; among the various poisons Sulphur is stronger and its reaction with cobalt particles is considered irreversible due to its large

adsorption energy. Furthermore Sulphur can also poison adjacent particles due to its size and electronegativity. Sulphur poisoning can be only avoided by cleaning of the synthesis gas feed properly; using zinc-oxide or lead-oxide guard beds is the preferred solution nowadays [Loosdrecht et al., 2013]. Consequences of the presence of nitrogen compounds are less severe than that of Sulphur compounds and mainly consist in competitive adsorption with respect to syngas molecules [Leviness et al., 1998]. Moreover the reactions involving nitrogen compounds and cobalt particles are reversible and can be regenerated by mild hydrogen treatment;

- surface reconstruction; the modification of the surface layer of cobalt catalysts is a thermodynamically driven process which can lead to a lowering of the surface energy. Typically, reconstructed surfaces are less active for FT synthesis, which is the reason why this mechanism could contribute to deactivation. Practices for avoiding surface reconstruction

Practices for reversing deactivation and regenerate deactivated Co FTS catalysts are almost only based on reversing the effects of the major deactivation mechanisms, i.e. sintering and carbon deposition. The most common method consists of treatment in hydrogen (reduction) and steam (oxidation), applying oxidation-reduction cycles and combination of these. Actually, by careful control of the oxidation step, deleterious carbon is removed as oxide at temperatures higher than 250 °C. Furthermore oxidation step is also a key step for improving the re-dispersion of the cobalt particles, first producing large oxide particles and then, through enhanced nucleation, generating smaller particles [Saib et al., 2006].

3.2 FT selectivity models

FT reaction mechanism is truly complex and for over 70 years the finer detail of the elementary chemical steps occurring onto the surface of the catalysts has been a matter of controversy; what is agreed is that a stepwise chain growth process is involved, similar to the polymerization of monomers. Besides its polymerization nature, FTS is also a catalytic driven process and thus include adsorption of reactants and monomer formation, as following:

1. *Reactant adsorption* – CO and H₂ adsorb to the active surface.

2. *Chain initiation* – Adsorbed reactants produce a C1 intermediate, which is the chain initiator.
3. *Chain propagation* – Carbon containing species is inserted into the growing chain, increasing its carbon number by one.
4. *Chain termination and desorption* – Product molecule is formed and desorbed from the surface.
5. *Secondary reactions of formed products* – Product molecules can re-adsorb onto the surface and participate in secondary reactions.

With the cursory analysis of the chromatograph, an exponential trend has been identified in describing the product distribution of FTS spectrum with carbon number. Also this behavior is typical of polymerization reactions; hence, FTS is generally described by a series of surface polymerization reactions which proceed by stepwise addition of a carbon monomer species and a termination step that leads to products upon desorption. Since the founding, industrial production of synthetic fuels has required developing as much predictive as possible models able to explain such a wide spectrum of products.

3.2.1 ASF model

Empirical model first at describing the FTS product distribution was derived from considering FTS an *ideal* polymerization reaction, with no dependence of product molar fractions on carbon number of the growing chain. This simple representation is known as “Anderson-Schulz-Flory” (ASF) distribution law, which can be mathematically written in an elegant form as:

$$y_n = (1 - \alpha) \alpha^{n-1} \quad (3.11)$$

Where n is the number of carbon atoms in the product molecule, y_n is the mole fraction of a hydrocarbon with chain length n and α is the ASF chain growth probability defined by:

$$\alpha = \frac{R_p}{R_p + R_t} \quad (3.12)$$

Where R_p and R_t are the rate of propagation and termination, respectively. If the reaction environment is kept constant, a relative comparison of α value would be a direct measure of the likelihood that a FT catalyst would catalyze chain propagation, rather than chain termination.

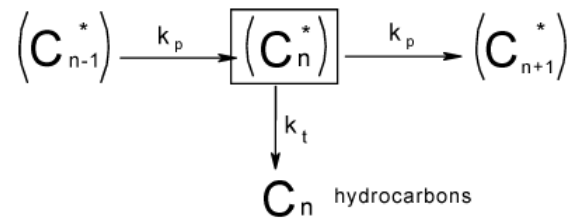


Figure 3.1: reaction growth scheme for ASF model (G.P. Vander Laan, 1999)

The value of α determines the total carbon number distribution of the FT products and it basically depends on the reaction conditions and catalyst type. For practical applications, the ASF formula is written in logarithmic form:

$$\log(y_n) = \log\left(\frac{1-\alpha}{\alpha}\right) + n * \log(\alpha) \tag{3.13}$$

By which it' s possible to observe that the semi-logarithmic ASF plot produce a straight line, i.e. a constant slope of the product mole fraction as a function of carbon number. The chain growth probability can be easily obtained from that value (fig. 3.2).

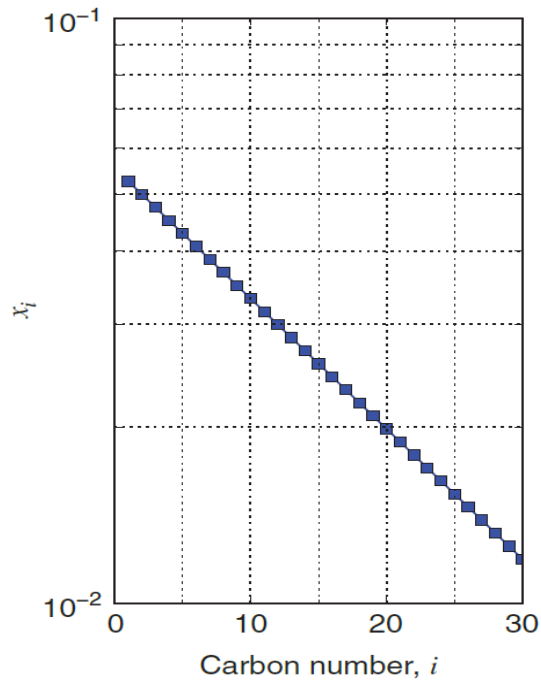


Figure 3.2: ASF distribution for all products (x_i is the logarithm of the mass fraction, i is the carbon number)

As can be deduced from the simple reaction network proposed by Anderson (fig. 3.1) and further can be seen in (fig. 3.3), ASF model considers only one termination constant for all products, thus it would be unable to distinguish between different product types (olefins, paraffins, oxygenates).

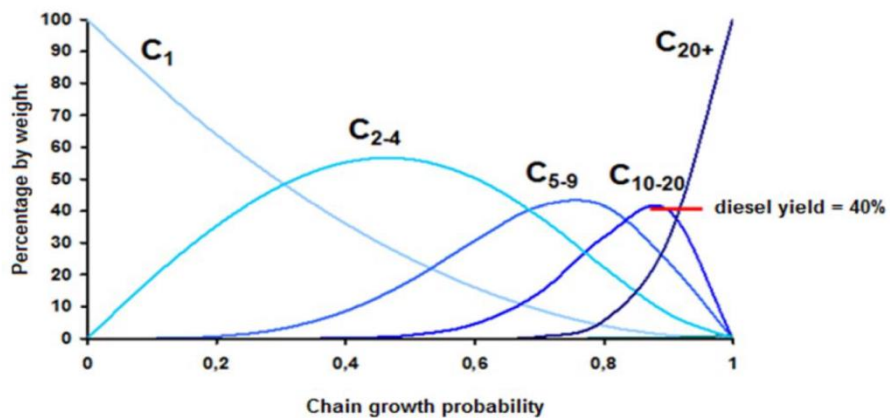


Figure 3.3: FT product carbon number distribution as a function of chain growth probability (from Ndimande, 2004).

Apart from that, the product spectrum over iron, cobalt and ruthenium catalyst very seldom follows the classical ASF distribution and usually reports the following deviations:

- High methane molar content than predicted by ASF;
- Lower C₂ hydrocarbon yield than in ASF diagram and lower olefin contents in the C₂ fraction;
- A positive bend in the ASF plot at high carbon numbers, due to an increase in chain growth probability with carbon number reaching an asymptote at higher carbon number;
- Chain length dependency of olefin contents, so that the olefin-to-paraffin ratio has an exponential decrease with chain length.

These deviations, generally known as “non-ASF behavior” , are attributed to many reasons, such as the occurrence of secondary reactions (hydrogenation, isomerization, α -olefin re-adsorption and hydrogenolysis) or two parallel FTS mechanisms (including two types of active sites, pathways or growth monomers), experimental VLE artifacts, accumulation of heavy products in the reactors (hold-up) and intra-particle and inter-reactor concentration and temperature gradients. The results from isotopic tracing technic over product spectrum was interpreted by van Dijk [van Dijk, 2001] as an evidence that FTS reaction is not an ideal polymerization reaction as ASF model predicts; van Dijk points out that FTS differs from an ideal polymerization reaction because of the following reasons: the monomer has to be formed *in situ* on the catalyst surface from the reactants; moreover, the rates of intermediate surface reactions are chain length dependent and the primary products can undergo secondary reactions. For all these reasons FT synthesis should not be viewed as a polymerization type reaction sequence, so that a product distribution like ASF' s should not be expected.

Moreover, some researchers start focusing on the fact that erroneous product analysis can introduce systematic deviations that may be mistaken by mechanistic phenomena, especially in non-steady state operations. In particular negative deviations from ASF plot were attributed to experimental errors in gas chromatography (GC), whereas positive deviations were thought to be caused by unsteady-state slurry operations. These reactor artifacts was considered likely to have a common root, the accumulation of heavy products, which spend considerably more time in the slurry phase compared to the light gas phase one.

However, even though the effect of product accumulation is surely to occur in a large and heavy product spectrum, it cannot be regarded as major cause for non ASF behavior in FTS reactor. This is justified by the fact that also lower-weight products (below C₁₀), which exist mainly in gas phase inside the reactor, show positive bend as the higher ones.

The ASF plot describes the entire product spectrum by a single value of α , the chain growth probability; however, the assumption that chain growth is independent on carbon number is not sufficient to explain FTS distribution.

3.2.2 Double alpha models

The first attempt to describe product distribution in a different way than ASF approach considered two values of chain growth probability, α_1 and α_2 , based on the notion that there are two different mechanistic pathways followed by reactants to synthesize hydrocarbon chains, two different growth monomers, or two different active sites, as explained with the well-known fact that two types of iron carbides are active in FTS. Latest explanation was discarded by the fact that cobalt and ruthenium based catalyst also display non-ASF behavior even though only the metallic phase of both of them was accepted to be active in FTS.

The double α model is a weighted sum of two ideal product distributions as follows:

$$y_n = (1 - \alpha_1) \alpha_1^{n-1} + (1 - \alpha_2) \alpha_2^{n-1} \quad (3.14)$$

The model is characterized by three independent parameters, the two values of chain growth probability, α_1 , α_2 and μ .

$$\mu = \frac{w_1}{w_1 + w_2} \quad (3.15)$$

w_1 and w_2 are the total mass or mole of products from chain growth α_1 and α_2 .

Last parameter requires accuracy of mass balance for the characterization of product spectrum and less accurate prediction of μ would influence the estimation of the other two model parameters, since these are not really statistically independent. Indeed, Botes [Botes, 2007] reported high values of covariance between all of three parameters, inducing low repeatability of double- α model results.

Recent advances in analytical techniques and procedures, as the two-dimensional gas chromatography GC x GC, allowed gaining more insights into the causes of non-ASF behavior, showing that deviations are probably function of reaction conditions and catalyst properties, instead of more than one chain growth mechanism as assumed by double- α model.

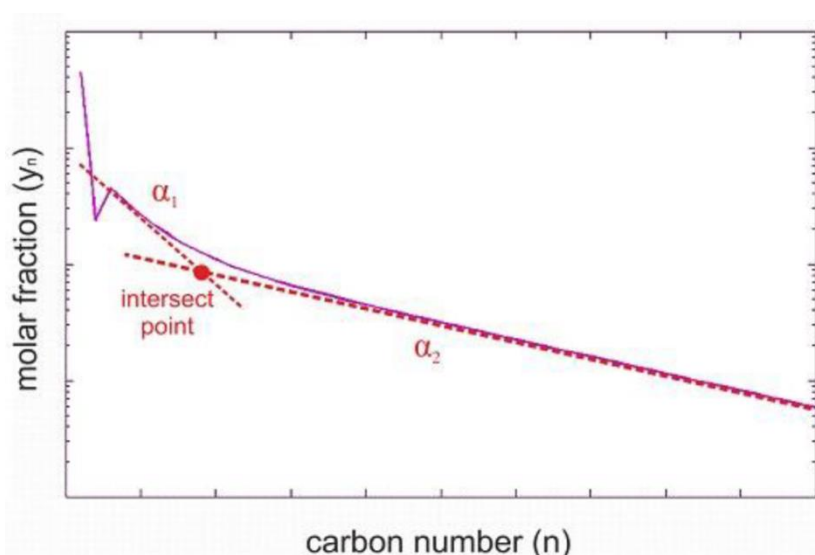


Figure 3.4: double-alpha explanation of the experimentally observed product distribution (on mole basis) [Todic et al., 2013]

Moreover, J. Gaube and H.F. Klein [Gaube et al., 2010] pose the evidence of two incompatible chain growth mechanisms from applied studies on FTS-active catalysts. Nevertheless, further issues of double- α models are their inability to separate between various product types (olefins, paraffins and oxygenates), so that OPR dependency on carbon number cannot be predicted, and not to account for the other aspects of deviations from ASF law at lower carbon numbers (C_1 and C_2 fractions).

3.2.3 Secondary olefin adsorption models

In order to explain the asymptotic behavior of product spectrum at high carbon numbers and the exponential trend of OPR with chain length, some authors proposed secondary reactions of initially formed olefins. Premise of these models are that olefins are the main primary product of FTS reactions and their main secondary reactions are hydrogenation to n-paraffin, re-adsorption into chain growth stream and isomerization to 2-olefins.

Generally, re-adsorption reaction of olefins takes place over primary FTS active site, while hydrogenation and isomerization occur over sites not active towards FTS.

The first mathematical model involving re-adsorption concept for FTS product description were developed by Novak et al., that showed as whether the majority of olefins re-adsorb or isomerize then the results would approach a curvature away from the ASF distribution at high carbon numbers that would account for the chain length dependency of olefin selectivity.

In order to study the reactivity and selectivity of 1-olefins for secondary reactions, usually co-feeding studies are needed. Typically, syngas is co-fed with C¹³-labeled olefins at the aim to discriminate between re-adsorbed, isomerized or hydrogenated 1-olefins out of the reactor. However, majority of co-feeding studies conducted over Fe or Co catalyst report that prevailing secondary reactions are hydrogenation, followed by isomerization and re-adsorption. For example, Kuipers et al. [Kuipers et al., 1996] also showed that co-fed 1-hexene did not re-adsorb to catalyst site to continue chain growth but rather hydrogenate or isomerize.

The re-insertion mechanism of 1-olefins was attributed to several physical phenomena, properly: diffusivity, solubility and physisorption.

3.2.3.1 Inhibited-diffusion olefin re-adsorption

Iglesia and co-workers [Iglesia et al., 1991] were first to advance an inhibited-diffusion enhanced re-adsorption distribution model (Exxon model) to explaining non-ASF behavior at high carbon numbers (Fig. 3.5).

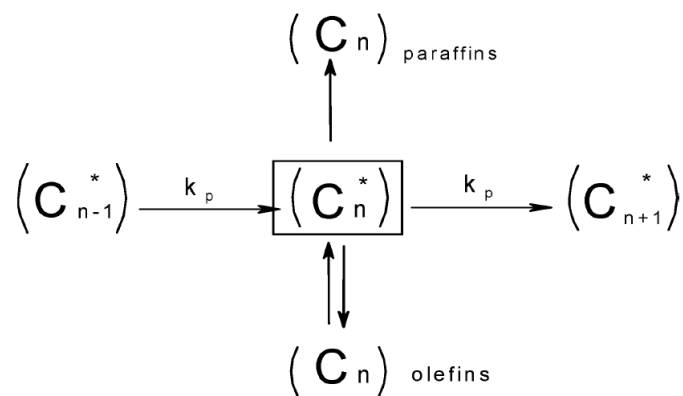


Figure 3.5: diffusion-enhanced olefin re-adsorption model network [Iglesia et al., 1993]

They suggested that re-adsorption rates for olefins increase the slower it diffuses away from the catalyst surface, due to increase in residence time. Since Graham' s law states that diffusivity of the products in the particle pores is a function of molecular size or carbon number (Fig. 3.6), this should explain the increase in chain growth probability with increasing carbon number until a constant asymptotic value is reached for large carbon numbers.

Deviations from the ASF distribution was justified introducing a carbon number dependent diffusion parameter, called Thiele modulus Φ , also accounting for the influence of reaction conditions and catalyst properties on re-adsorption of 1-olefins:

$$\phi_n = \frac{k_{r,n}}{D_n} \left(\frac{L^2 \cdot \varepsilon \cdot \theta_{MC}}{R_p} \right) = \psi_n \cdot \chi \quad (3.16)$$

Where $k_{r,n}$ is the first-order rate constant for the olefin re-adsorption reaction, D_n is the effective diffusivity, L is the average radius of the catalyst pellets, ε is the void fraction, θ_{MC} is the active site density and R_p is the average pore radius of the metal oxide support. The influence of catalyst is clearly shown through the catalyst design parameter χ , whereas the parameter ψ_n reflects the molecular properties of olefins with n carbon number. Iglesia et al. showed that C_{5+} selectivity increased by varying the structural parameter χ between a restricted range (10^{17} and 10^{19} m^{-1}) due to an increase in the rate of olefin re-adsorption, while at values higher than that range the C_{5+} selectivity decreased due to CO mass transfer limitations into catalyst pores. Main critics moved against the Exxon model focused on the experimental fact that a different carbon number dependency is found for olefin diffusivity. Effectively, Iglesia et al. assumed an exponentially decrease with chain length of olefin diffusivity ($D_n \sim e^{-0.3n}$ for Exxon model) [Todic et al., 2013]; however, report of Shi and Davis [Davis et al., 2012] highlighted that molecular diffusivity of hydrocarbons displayed much lower dependency with the chain length and further experiments by Davis inferred that inhibited-diffusion enhanced re-adsorption reactions is only significant for products with carbon number greater than 17 [Todic et al., 2013].

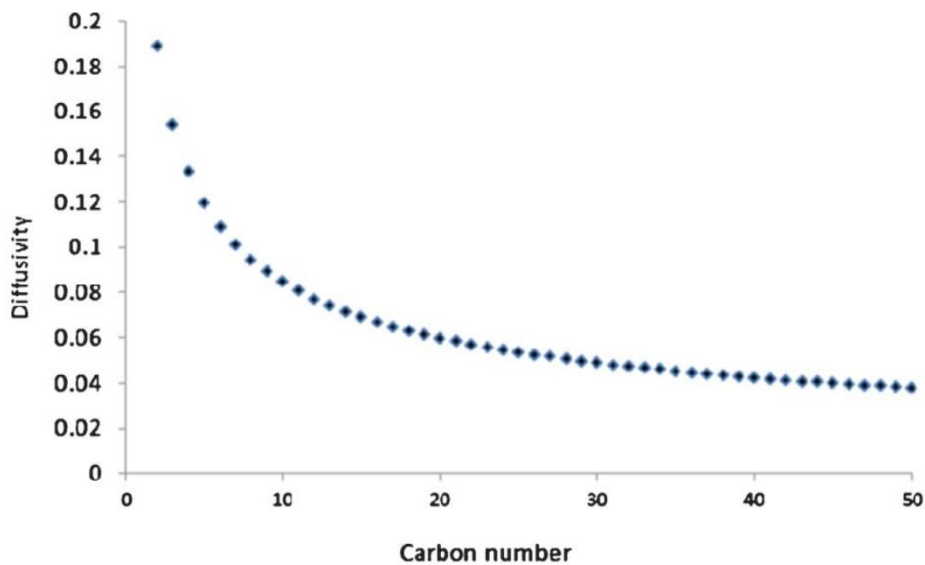


Figure 3.6: Graham's law diffusion for n-olefins with different carbon number [James et al., 2012]

3.2.3.2 Enhanced-solubility/physisorption olefin re-adsorption

Davis et al. [Davis et al., 2012], as well as others, have opined that the carbon number dependency for residence time of α -olefins is caused by their solubility in the liquid reaction product (wax) at the reactor or catalyst pore level. Effectively, experimental results state the carbon number dependency of solubility is much stronger than diffusivity and its trend appears exponential with chain length.

According to enhanced solubility re-adsorption models, re-adsorption rate increases with the concentration of activated complex of olefin and surface species, which also depends on solubility in the liquid phase (wax). When activation complex is more solvated than the reactants, then re-adsorption rate constant is higher than the gas phase rate constant. This implies that solubility enhances re-adsorption of olefins and continued chain growth [James et al., 2012] but what is more relevant lies in considering re-adsorption as kinetically controlled rather than by thermodynamics.

However, results from experimental vapor-liquid equilibria showed the same olefin re-adsorption tendency with chain length, challenging the assumptions by a thermodynamic point of view. Actually, at equilibrium the activity/chemical potential of a substance is identical in liquid/gas phases. This implies that the reactivity of re-adsorption reactions

(re-adsorption rate constant) is independent on concentration/solubility in the liquid phase.

Since the influence of chain length over adsorption enthalpies is experimentally well-known, physisorption has been considered as one of the main factors in explaining the carbon number dependency of olefin re-adsorption rate; generally, a linear relationship has been observed between adsorption enthalpies and carbon number, so that the re-adsorption rate constant trend with carbon number could approach an exponential behavior [Todic et al., 2013].

Several authors have shown the importance of physisorption for the increase of re-adsorption rate with carbon number, accounting also for solubility effect at the wax layer. One of these models, properly the olefin re-adsorption product distribution model (ORPDM) by Van der Laan and Benackers (Fig. 3.7), became very popular [Van der Laan et al., 1999]. The authors relate solubility and physisorption effect on olefin re-adsorption rate through a single constant 'c' at the exponent:

$$\frac{C_{C_nH_{2n}}}{P_{C_nH_{2n}}/RT} \sim e^{c \cdot n} \quad (3.17)$$

ORPDM model has been derived based on the carbide mechanism, being the first model to describe product distribution through a mechanistic approach: adsorption, chain initiation, propagation, termination and monomer formation were taken into account.

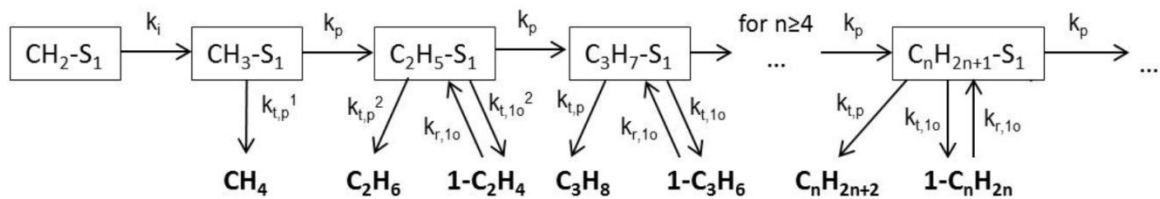


Figure 3.7: reaction network of Van der Laan and Benackers model (ORPDM) (van der Laan et al., 1999).

However, the authors of the model did not mention anything about the occurrence of other type of secondary reactions, such as hydrogenation and isomerization, for which co-feeding experiments showed are as major secondary reactions.

Kuipers et al. [Kuipers et al., 1995] developed a solubility-physisorption enhanced re-adsorption model accounting for all of the secondary reactions, but they did not calculate

the probability for each of them to occur, i.e. selectivity. However, they differentiate between primary FTS sites (propagation and re-adsorption sites) and secondary reaction sites (hydrogenation and isomerization sites). Their studies were conducted over Co foil and Co-based catalyst and results showed that OPR dependency on chain length was pronounced over the free-wax layer also, displaying neither solubility or diffusion are major reason for the deviations from ASF and OPR behavior at higher carbon numbers. Moreover, physisorption concept was justified by the small probability for olefin to be re-adsorbed over metal surface after desorbing, as an olefin has to compete with high-adsorptivity molecules like H₂ and CO for its surface occupation [Todic et al., 2013].

3.2.4 Chain length olefin desorption models

In contrast to the assumptions of the olefin re-adsorption models, Kuiper et al. opined that the deviations from ASF behavior at high carbon numbers are likely due to chemical behavior of surface intermediates prior to leaving the active site or the catalyst surface [Kuiper et al., 1996]. Assumptions from their model are that paraffin and 1-olefin are primary products, each having a common propagation rate, but a different rate of termination.

Also Botes was highly critical of olefin re-adsorption concept, due to the high deviations from ASF of product distribution over iron catalyst [Botes, 2007], even though there is very poor evidence of high re-adsorption rates over these catalysts. These authors suggest that the chain length dependency of desorption rate to 1-olefin could be at the origin of the deviation of product distribution at high carbon numbers. Therefore, the deviation was attributed to chemical behavior of surface intermediates at the termination step: hydrogenation to paraffin and chain growth are considered as independent on chain length, while chain desorption to 1-olefin is a function of carbon number. Botes proposed an empirical formula to justify the increasing interaction between surface intermediate and metal surface with carbon number [Botes, 2008]:

$$E_d = C \cdot n \quad (3.18)$$

where C is an empirical value. Therefore, energy required for desorption E_d is linearly decreasing with carbon number. Chain growth probability as a function of carbon number α_n is described in terms of rate constants, k , of the three generic reactions as follows:

$$\alpha_n = \frac{k_g}{k_g + k_h + k_d e^{-k'n}} \quad n \geq 3 \quad (3.19)$$

Where k_g , k_h , k_d are the reaction rate constants for chain growth, hydrogenation and desorption, respectively, dependent on catalyst and reaction conditions (temperature and reactant feed ratio), while k' is the exponential dependency of olefin desorption rate on chain length ($k' = \frac{c}{RT}$).

The equation above explains the increasing trend of chain growth probability with carbon number, due to exponential dependency of olefin desorption rate on chain length. Also the asymptotic behavior of product distribution at higher carbon numbers has been solved as desorption term become negligible for long chain hydrocarbons until chain growth probability approaches a constant value.

The chain length OPR dependency was simultaneously proved by using the same parameters:

$$OPR = \frac{k_d}{k_h} e^{-k'n} \quad n \geq 3 \quad (3.20)$$

The desorption model treated the C_1 precursor like an higher C_n surface species, due to its lower chain growth probability, and can terminate via hydrogenation or desorption, without considering the mechanistic implication of desorption. Thus, the rate of formation of methane was predicted fairly well using the same parameters as higher carbon number fraction. The negative deviation for total C_2 hydrocarbons and the lower than expected ethylene/ethane ratio was explained by the assumption [Dry at al., 2001] that C_2 surface species can grow on two different active positions. This was accounted for dividing the ratio of desorption and hydrogenation over growth rate for two:

$$\alpha_n = \frac{k_g}{k_g + 0.5 k_h + 0.5 k_d e^{-k'n}} \quad n = 2 \quad (3.21)$$

This way the C_1 and C_2 hydrocarbon selectivity was predicted without adding further parameters.

However, drawbacks of the desorption model were that it didn't consider any of the olefin secondary reactions in the model, neglecting the residence time effect on product formation rate, and that it was not derived from a mechanistic approach, so the physical meaningfulness cannot be verified.

Each of the product selectivity models encountered so far shares a poor understanding of the mechanism of the FTS chemical reactions: they only included generic steps of chain growth and termination to 1-olefin and n-paraffin, neglecting steps that precede monomer formation (adsorption and chain initiation). This way the reactant (H₂ and CO) disappearance and inorganic and/or oxygenated species (H₂O) formation cannot be predicted. Moreover, the kinetic constant used in selectivity models are pseudo-kinetic parameter, so depending on reaction conditions (pressure, reactant feed ratio, conversion level); therefore, they could be quite precise for the conditions they are optimized for, but not for all relevant ranges of industrial conditions.

3.3 FT kinetics

First kinetic model including adsorption and chain initiation besides propagation and termination steps in the FTS reaction sequence appeared in the 90s. Such models were derived based on macro-kinetic studies, in order to gain insight into mechanistic sequence of FTS complex reaction system.

Basically these studies followed two kinds of approach: either deductive or inductive [James et al., 2012]. The former was based on extrapolating the mathematical behavior of FTS product formation rate from experimental kinetic results, fitting data with empirical or polynomial functions. This approach doesn't give a comprehensive and clear understanding of the full FTS sequence, due to many fitting parameters that could not have physical meaningfulness. Instead, inductive approach provides a series of different mechanistic sequences to be assessed: rate equations are derived based on the proposed mechanism and the equation that best fits the kinetic data is considered more reliable in representing the actual reaction mechanism.

Each of these kinetic models takes into account reactant adsorption and intermediate species formation and the derived rate equations could be generalized to the following form:

$$rate = A \frac{k_i \prod C_i^{\alpha_i} - \frac{k_{-i} C_i^{\beta_i}}{\prod K_j \dots}}{(1 + \sum K_i C_i^{\eta_i})^n} \quad (3.22)$$

Where $i, j, k..$ are sequential elementary steps, k_i and k_{-i} are rate constants for backward and reverse elementary step i , K_i are equilibrium constants for elementary step i , C_i are concentration of the species involved in the elementary step i . The equation above was derived based on the Langmuir-Hinshelwood-Hougen-Watson methodology and has been accepted as general form for the representation of multi-step heterogeneous catalytic reaction [Susu,1997].

FTS kinetic model are very useful for a comprehensive understanding of actual reaction sequence and large scale applications need a model capable to predict accurately formation and consumption rates for a wide range of conditions. In that respect, LHHW methodology allows obtaining a detailed model in which all parameters are intrinsic kinetic constants, which result independent on reaction conditions. However, an accepted and reliable detail kinetic model able to accurately describe all of the reaction steps is still missing, mainly due to controversial opinions about monomer formation and C-C coupling pathway during propagation step.

3.3.1 FTS reaction mechanisms

What made FT synthesis different from a simple polymerization reaction, where feed reactants are monomers, is that monomer has to be formed *in situ* (after surface reaction between reactants) before entering the propagation (coupling) cycle. Therefore, a detail description of FTS mechanism sequence not asks only for a deep understanding of chain initiator generation, chain propagation and termination or desorption step but it also requires to completely unraveling the monomer formation pathway.

In the past, theoretical studies focused on the preferable pathway CO molecule followed up to activation and the identity of the propagation monomer. Only recently mechanistic discussion about CO activation has been resolved, while questions such as identity of the monomer species and chain-monomer coupling for propagation are still matter of debate.

More generally, proposed main rival mechanism tends to be divided on the basis of whether growing chain include or not oxygen in its structure or, alternatively, CO molecule dissociates before or after it enters the propagation cycle, respectively.

Mechanisms that consider de-oxygenated surface species as growing chain are based on carbide theory, first introduced by Fischer, which presume that CO is activated as surface carbides followed by sequential hydrogenation to some CH_x species. There are three main mechanisms that are based on carbide intermediates: alkyl, alkenyl and alkylidene mechanism.

3.3.1.1 Alkyl mechanism

The carbide mechanism enjoyed wide acceptance in the first fourteen years after the discovery of FTS. Since then it has been widely revised and alternative forms have been proposed. Experiments over iron catalyst by Bred and Petit indicated CH_2 (methylene) as more likely monomer or intermediate in hydrocarbon chain growth, stating alkyl-methylene as main couple in C-C coupling pathway. The carbide mechanism was then renamed 'alkyl' mechanism.

The most common used form of alkyl mechanism is displayed in (Fig. 3.8-3.9), which shows CO molecule adsorbs to active site surface as metal carbide and dissociates readily from oxygen. At this time, it is hydrogenated to methylene monomer species and/or successively to the methyl chain initiator ($-\text{CH}_3$). Chain propagation proceeds by successive insertion of CH_2 monomer into growing alkyl chain and termination occurs by hydrogenation to either n-paraffin or desorption to 1-olefin or hydroxylation to n-alcohol. However, alkyl hydroxylation to alcohols has never been validated since the role of hydroxylate group into oxygenated formation hasn't been never proved experimentally. Hence, an important lack of alkyl mechanism was its inability to explain oxygenated product formation in FTS.

Moreover, experiments with labelled carbon in surface carbides showed as only a small amount of products originated from carbides intermediates, definitively encouraging researchers to explore alternative pathways.

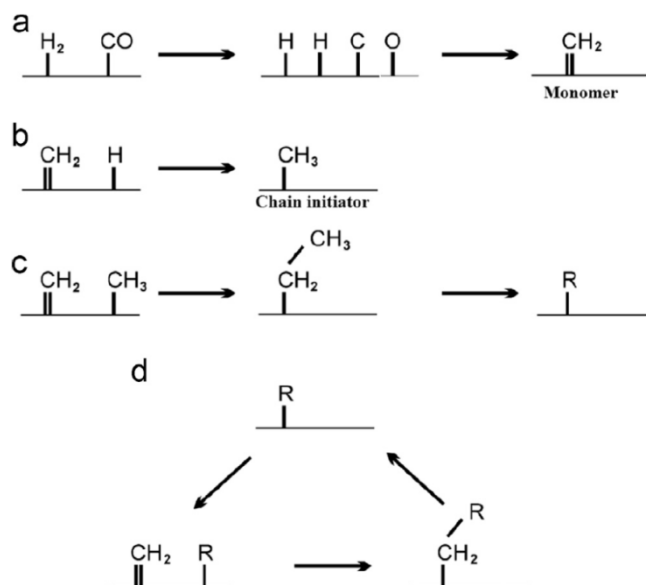


Figure 3.8: alkyl (carbide) mechanism: a) monomer formation; b) chain initiation; c-d) chain growth and propagation [Fontenelle et al., 2011].

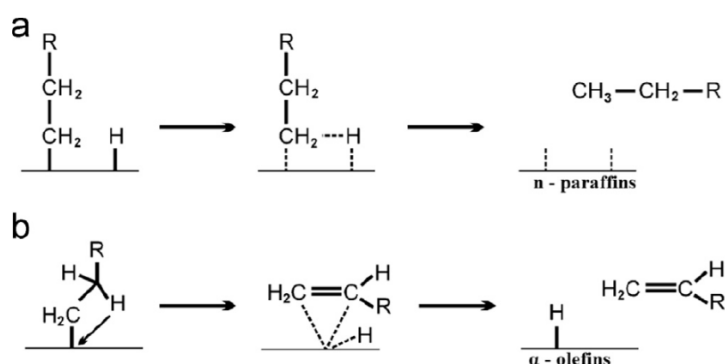


Figure 3.9: alkyl (carbide) mechanism termination: a) surface hydride termination yielding n-paraffins; b) β -elimination mechanism yielding α -olefins [Fontenelle et al., 2011].

3.3.1.2 Alkenyl mechanism

According to analysis of products from FT reactor fed with C^{13} labelled alkenes and experiments on different C-C coupling pathways, Maitlis *et al.* advanced that alkenyl-methylene coupling was more energetically favorable than that between alkyl-methylene species as C-C coupling pathway [Maitlis et al., 1999]. In what is called "alkenyl" mechanism, chain initiator originates from carbon coupling reaction between adsorbed

methylene (CH_2) and methylidyne (CH) species. The resulting vinyl (i.e. alkenyl) intermediate ($\text{CH}=\text{CH}_2$) starts propagation with insertion of methylene monomer and successive vinyl-allyl re-arrangement step. The surface allyl intermediate ($\text{CH}=\text{CHR}$) terminates chain growth by hydrogenation to form 1-olefin. Indeed, the mechanism considered 1-olefin as only major products, paraffin likely formed by secondary olefin hydrogenation.

However, this mechanism obtained only a short period of acceptance. Assumption of a vinyl species as chain initiator was challenged by Shi and Davis based on the validity of interpretation of results from C^{13} isotopic tracer experiments, while allyl-vinyl isomerization/re-arrangement step was found to be not replicable under Fischer-Tropsch synthesis conditions. (Fig. 3.10) shows main steps for alkenyl mechanism:

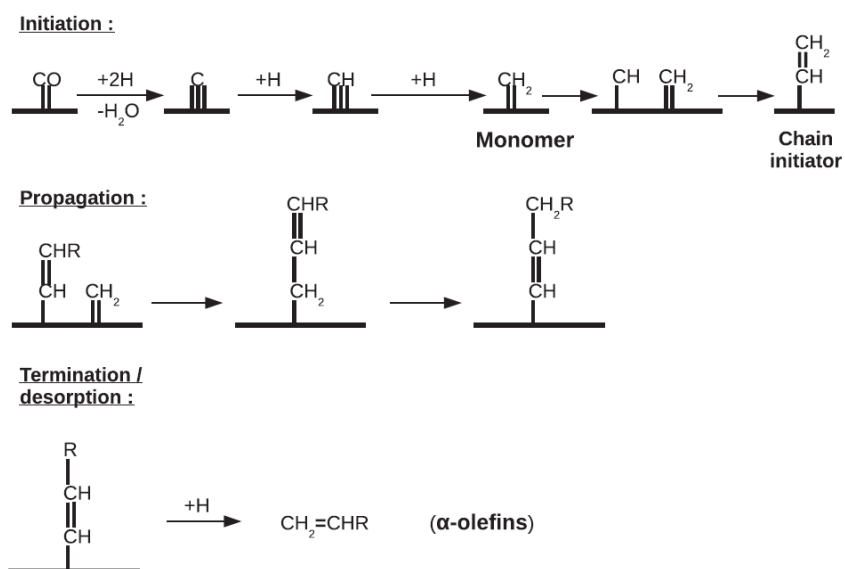


Figure 3.10: alkenyl mechanism (Claeys et al., 2004).

3.3.1.1 Alkylidene mechanism

Experiments and theoretical calculations from Ciobica et al. showed that adsorbed methylene (CH_2) is kinetically unstable: it readily decompose to methylidyne (CH) species [Ciobica et al., 2002]. Therefore, they started investigating the role of a CH monomer in chain propagation. According to Ciobica et al. CH could play a dominant role in chain growth in what had known as "alkylidene" mechanism (Fig. 3.11).

The reaction sequence starts as soon as CO molecule dissociates and hydrogenated to methylidyne CH. Therefore, it can be inserted into alkylidene ($=\text{CH}-\text{R}$) or alkyl ($-\text{CH}_3$ $-\text{CH}_2$ $-\text{R}$) intermediate and suddenly H is added. The sequence terminates when growing chain undergoes β elimination of hydrogen to give 1-alkenes. As for alkenyl mechanism, majority of primary products are 1-olefin and paraffin are formed by secondary olefin reactions.

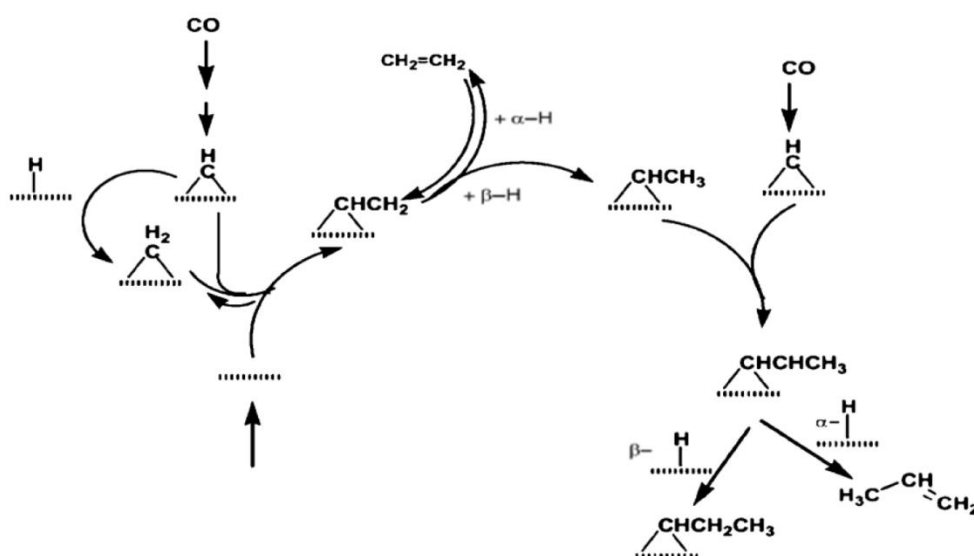


Figure 3.11: alkyldiene mechanism [Maitlis et al.,2009].

Nowadays, computational chemist offers an effective tool to explore micro-kinetic side of FTS and give mechanistic insight into complex networks of reactions without use of experiments. For example, simulating different elementary reactions and calculating activation energy for each of them, DFT (Density-Function-Theory) made it possible to discriminate between rival elementary steps and identify the actual reaction sequence [Todic et al., 2013].

A major success for computational chemist in FTS has been to determine a sort of hydrogen-assisted CO dissociation path as favorable chain initiation scheme for carbide mechanism (CO activation). Also simulation-based results from different authors, such as Zhuo and Storsæter, converged to retain that CO adsorbed is hydrogenated before C-O bond is split [Storsæter et al., 2006]. However different interpretations were provided on which of the activation steps would be rate-limiting (hydrogenation of CHO or of CH₂O).

The hydrogen-assisted CO dissociation path has been the base for the suggestion of two FT synthesis mechanisms: enol and, much more recently, CO insertion mechanism (Fig. 3.12 and 3.13).

3.3.1.4 Enol mechanism

Main drawback of carbide mechanisms was recognized as not to account for oxygenated intermediates in chain propagation, so that they were difficult at explaining oxygenated product formation, such as alcohols, aldehydes and ketones.

Already few years after FTS discovery, in 1940, analysis of products from isotopic studies detected the presence of oxygenated intermediates on iron catalyst under mild conditions (high pressure and relatively low temperature). Also, many years after that a series of isotopic studies from Davis et al. [Davis et al., 2001] suggested the role of oxygenated intermediate to the hydrocarbon formation over iron catalyst, based on high tendency of co-fed alcohol to re-incorporate and initiate chain growth. First mechanism to consider oxygenated intermediate as playing a major role in FTS propagation was enol mechanism, introduced by Storch et al in the 50' s [Storch et al., 1951].

According to it, chain initiates from hydrogenation of adsorbed CO to hydroxyl-carbine CHOH (i.e. enol). Successively, hydrogen drives propagation through condensation of two enol species with followed elimination of water, as depicted below (Fig. 3.12). The termination step consists of dehydration of n-alcohol to n-alkene or desorption to n-alcohol and other oxygenated products [Storch et al., 1951]. As for alkenyl and alkylidene, enol mechanism treats olefins as major products, ruling out paraffin from primary FTS interaction route.

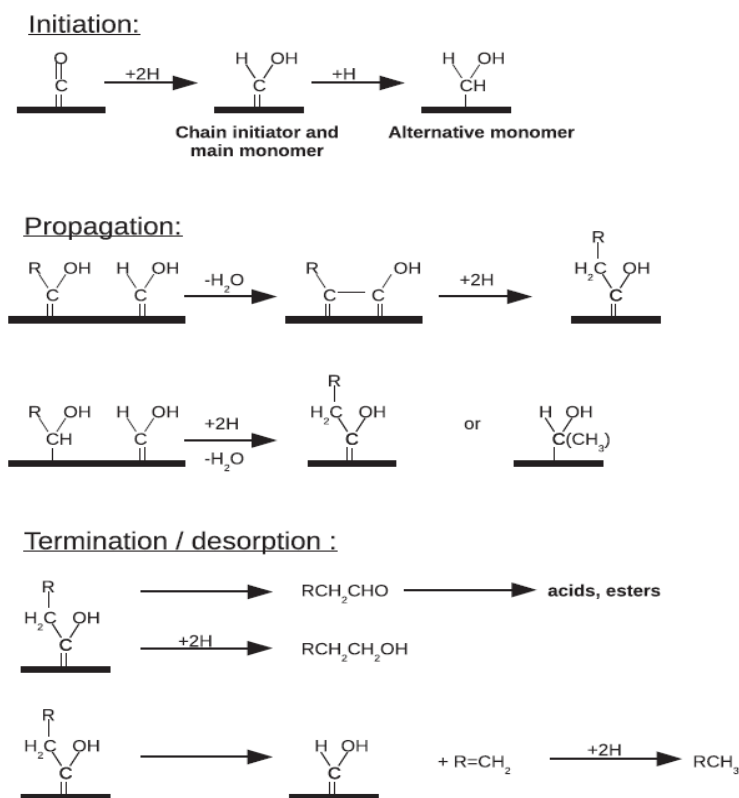


Figure 3.12: enol mechanism [Claeys et al.,2004].

3.3.1.5 CO-insertion mechanism

Besides isotopic tracer studies, also more advanced IR and DRIFT (diffuse-reflectance-infrared-Fourier-transform) spectroscopy-based technology devices were useful to researchers for detecting stable oxygenated intermediates on iron and cobalt catalyst. Hence, many experimental results motivated theoretical studies revisiting FTS mechanism and accounting for oxygenated intermediates in the formation pathway to alcohols and aldehydes.

Also the acquired knowledge about iso-synthesis and other chemical sequences involving similar C-C coupling reactions of CO helped route the scientific compliance towards CO-insertion mechanism.

This mechanism was developed by Pitchler and Schulz during the 70' s and was the first to account for oxygenated products together with paraffin and olefin as primary products in FTS [Pitchler et al., 1970].

CO-insertion mechanism starts with CO adsorption (Fig. 3.13) and hydrogenation to $\text{CH}_2(\text{OH})$, after which it is further hydrogenated and water is eliminated, leaving an alkyl species (CH_3) as chain initiator (as in alkyl mechanism). Propagation proceeds by direct insertion of CO into the alkyl-metal bond and successive hydrogenation to form an acyl species $\text{CH}(\text{OH})\text{R}$. At this point, the acyl intermediate can leave out or take up hydrogen to form aldehyde or alcohol, respectively. Or it could be hydrogenated and consequently dehydrated to give an alkyl intermediate which could propagate or terminate to form olefin or paraffin by hydrogenation or hydrogen elimination, respectively.

Recently, several theoretical studies using computational tools such as DFT (density function theory) by Cheng et al. and Zhuo et al. showed that micro-kinetic simulations via direct reaction surface CH_x and CO is thermodynamically and kinetically favored compared to CO dissociation and successive chain initiation involving CO hydrogenation [Cheng et al., 2008; Zhuo et al., 2009]. Hence, theoretical and experimental studies converged to look at the CO-insertion mechanism as more probable C-C coupling mechanism on iron and cobalt catalysts.

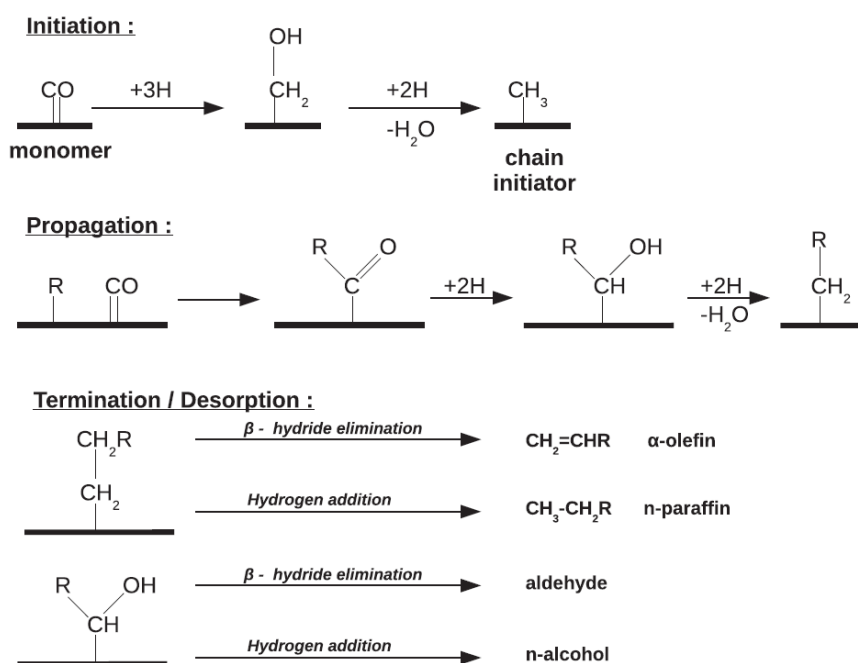


Figure 3.13: CO-insertion mechanism [Claeys et al., 2004].

3.4 Effect of process conditions on selectivity

Generally, it's well accepted that overall FTS product selectivity is influenced by variations in process parameters (temperature, pressure, reactant feed ratio, conversion level) to some extent.

The occurrence of secondary reactions of FTS primary products (olefin re-adsorption, hydrogenation, isomerization) and reactants (CO hydrogenation by water-gas-shift) makes the analysis of the effect of process conditions on FTS product selectivity a complex matter.

In particular, drawing a conclusion on the effect of process parameters on FTS product selectivity is complicated on iron catalysts because of its high activity for WGS. This reaction is charged for increasing the partial pressure of hydrogen (further supply to FTS) and carbon dioxide and decreasing carbon monoxide and water. These changes directly reflect on variation in kinetics of FTS and secondary reactions.

On cobalt-based catalysts, the effect of WGS is less relevant for less activity showed by cobalt towards this reaction and because of the role of lower temperatures involved with cobalt-base catalyst, which is responsible for a general decrease in WGS rate. Otherwise, the permanence of a liquid product phase in between the feeding (gas) and active phase (solid) would enhance olefin secondary reactions due to increase of chain length dependent solubility, diffusivity or physisorption effect. Therefore, the analysis of process parameter on FTS cobalt-based product selectivity should have great regard for the effect of secondary reactions of primary FTS products (1-olefin).

3.4.1 Temperature

A common behavior reported for all catalyst types is that increasing temperature has the effect of lowering the content of heavier C_{5+} products while rising selectivity up for lower weight products.

Among lighter products, methane selectivity shows a rapid increase whereas C_2 hydrocarbons only a small increment with increasing temperature in both high and low temperature mode of operation; however, changes in selectivity for lighter products (methane more than the others) together with a clear decline for C_{5+} contents are more pronounced for cobalt-based catalyst compared to iron [Todic et al., 2013].

This shift towards lighter products has been interpreted as caused by an overall decrease in chain growth probability value. As seen above, chain growth probability depends on the relative value of termination compared to propagation rate and some authors believe that activation energy for termination would be slightly higher than that for propagation. The assumption of higher potential barrier for termination will imply that termination rate vary more rapidly than propagation by increasing temperature. That would explain the overall lowering of chain growth probability with increasing temperature.

Instead, the influence of temperature on OPR is more complex due to the modification induced by changing temperature on kinetics of secondary olefin reactions, mainly re-adsorption. At this regard, very high activation energies (150 kJ/mol) are reported for secondary 1-olefin reactions, which means that an increase in temperature would increase the rate constant of secondary reactions faster than what occurs for primary hydrogenation or olefin desorption [Todic et al., 2012]. This could favor secondary olefin reactions mostly resulting in a decrease of OPR with temperature.

Actually, also the opposite behavior has been observed for OPR with varying temperature, making the relation difficult to reveal.

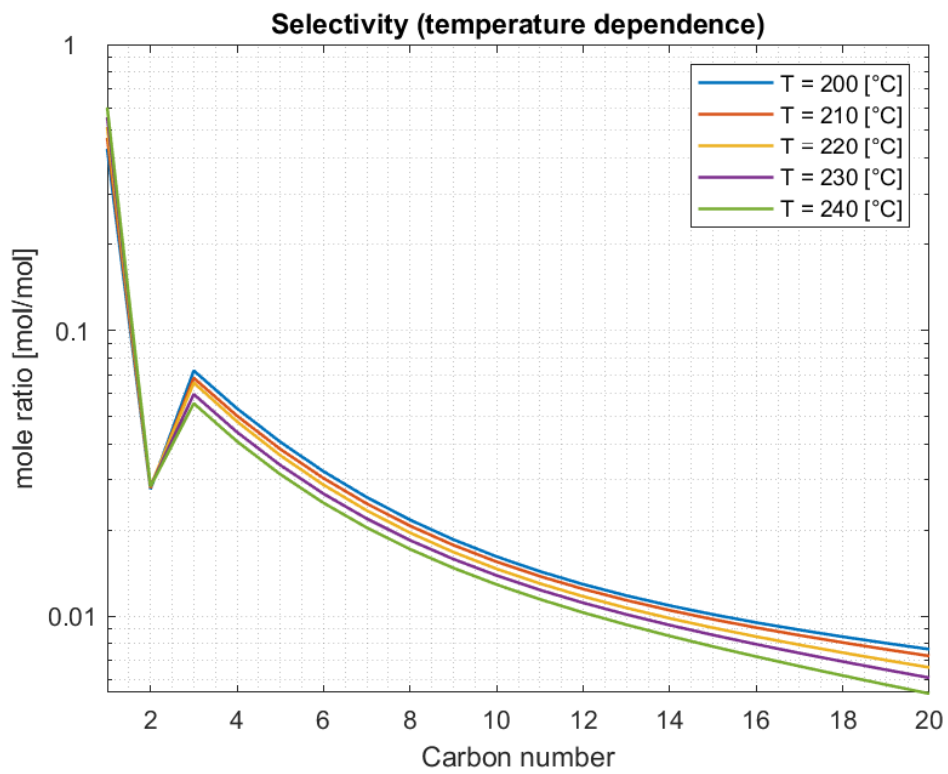


Figure 3.14: effect of varying process temperature in the FT cobalt-based reactor of the simulation model in this work ($P=2$ MPa, $H_2/CO = 2.078$, $\mathbf{x}_{CO} = 82.5$ %) on hydrocarbon molar fractions with carbon number (a form of carbide mechanism from Todici et al. 2013).

3.4.2 Pressure

General consensus is that increasing pressure has beneficial effects on selectivity (shift towards heavier products) and FTS rates.

Typically, increase in pressure leads to lower methane and higher C₅₊ selectivity for all catalysts. This could be due to a general increase in chain growth probability value with increasing pressure [Todic et al., 2013].

Actually, typical effect of pressure is to reduce the hydrogen coverage while increasing the CO coverage altogether. Lower values of hydrogen coverage imply reduced rate for chain termination (primary hydrogenation) to n-paraffin whereas higher carbon coverage causes the chain growth rate to rise up. Such a combination of effects could explain why chain growth probability increases when pressure is increased.

Moreover, either lower hydrogen or higher carbon monoxide coverages are known to inhibit secondary olefin hydrogenation also, in a way such that one should expect an increase in OPR with increasing pressure.

Instead, mixed results are commonly reported by several authors for the effect of pressure over OPR with carbon number. For instance, Todić et al. reported conflicting results for pressure effect on OPR trend with carbon number over iron and cobalt based catalyst [Todić et al., 2013]. Their experiments on iron catalyst revealed OPR exhibited an overall increase whereas a slight decrease has been observed for cobalt-based catalyst when raising pressure from 1.5 to 2.5 MPa. Because increasing pressure is supposed to decrease the hydrogen coverage, thus decreasing the rate of primary hydrogenation to n-paraffin, one should expect an increase in OPR if olefin formation would be unaltered.

Maybe an increase in olefin partial pressure could enhance secondary reactions (re-adsorption, isomerization) that would compensate for hydrogenation-inhibited effect of pressure, making for a net decrease of OPR [Todić et al., 2013]. Therefore, how pressure affects OPR depends on the competing effect of several mechanisms and, as for temperature, secondary effects has to be taken into account.

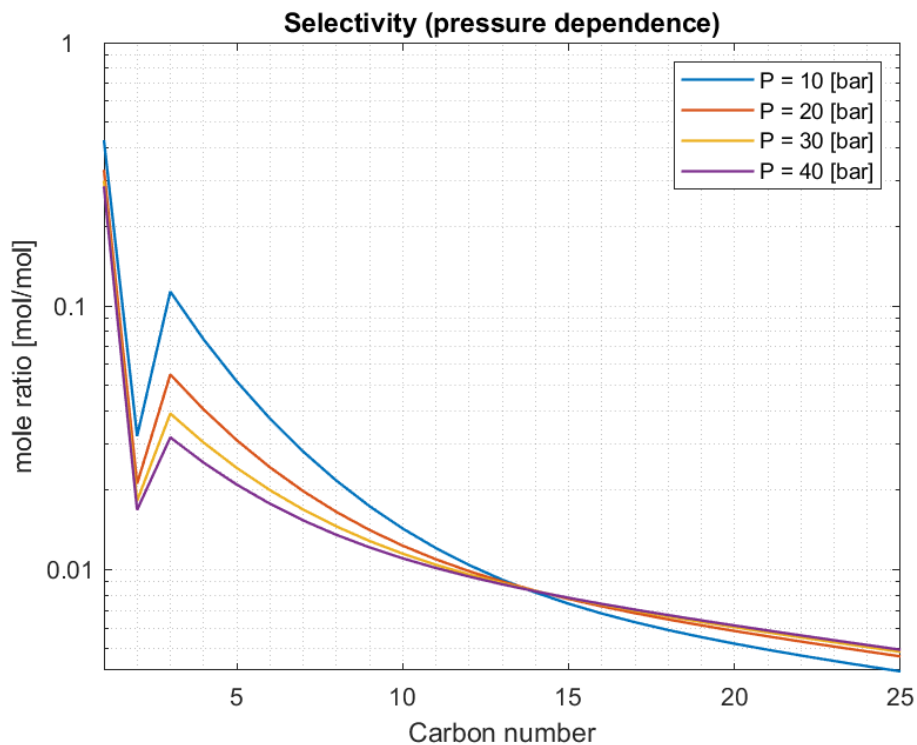


Figure 3.15: effect of varying process pressure in the FT cobalt-based reactor of the simulation model in this work ($T=230\text{ }^{\circ}\text{C}$, $\text{H}_2/\text{CO} = 2.078$, $\mathbf{x}_{\text{CO}} = 82.5\%$) on hydrocarbon molar fractions with carbon number (a form of carbide mechanism from Todic et al. 2013).

3.4.3 Reactant feed ratio

The effect of varying H_2 to CO ratio is widely reported in literature. Typically, lowering the reactant feed ratio under FTS stoichiometric value was proved to enhance the C_{5+} selectivity and for obtaining lower light products (C_1 and $\text{C}_2\text{-C}_4$ fractions). The reason would be the change in chain growth probability following the variation in hydrogen and monomer coverage. In particular, higher carbon monoxide respect to hydrogen surface coverages are noted for enhancing propagation over termination and consequently increasing chain growth probability α_n .

Notable is that variation with reactant feed ratio of α_1 is more pronounced than for α_{2+} . These results have been reported from studies of Todic et al. [Todic et al., 2013], Yates and Satterfield [Yates et al., 1994] and Van der Laan and Benackers [van der Laan et al., 1999]. These authors opined that enhancing C_{5+} selectivity effect with lowering H_2/CO ratio could be the consequence of a major effect of reactant feed ratio over α_1 . Numerous reports exist also on the effect of reactant feed ratio on OPR. Generally a decreasing

trend of OPR with increasing reactant feed ratio has been observed for all catalysts. Indeed, lower H_2/CO ratio implies higher CO partial pressure and it is widely known the inhibiting properties of CO to secondary hydrogenation. Thus lower H_2/CO means less probability for secondary hydrogenation, thus improving olefin formation and increasing OPR.

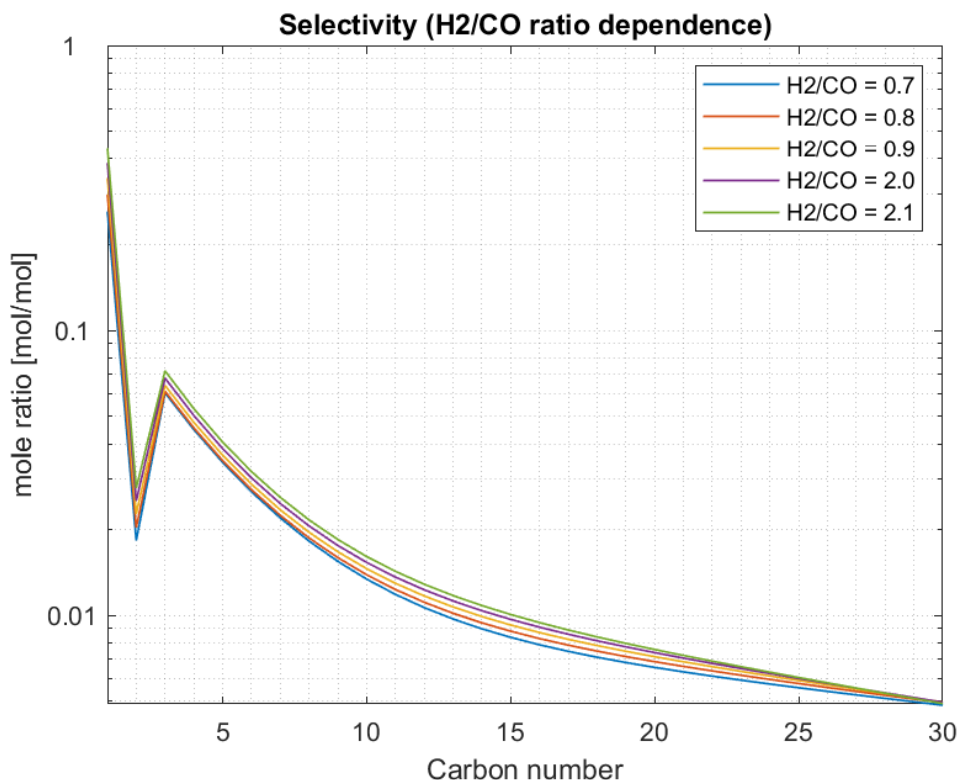


Figure 3.16: effect of varying process syngas ratio in the FT cobalt-based reactor of the simulation model in this work ($T=230\text{ }^{\circ}\text{C}$, $H_2/CO = 2.078$, $x_{CO} = 82.5\%$) on hydrocarbon molar fractions with carbon number (a form of carbide mechanism from Todic et al. 2013).

3.4.4 Conversion level

From experimental studies on the effect of conversion level on iron-based catalysts, generally CH_4 and C_{5+} selectivity remains relatively constant at different space velocities (i.e. conversion). Many researchers have computed constant chain growth probabilities for iron catalysts and their results show a constant trend with varying conversion at constant pressure, temperature and reactant feed ratio.

The effect of conversion is complicated by high activity of iron for WGS, which increases significantly by increasing partial pressure of water with increasing conversion and further supplies FTS active sites with hydrogen. Consequently, higher hydrogen to monomer coverages are known to increase the rate of termination, in turn decreasing the probability of chain growth. The lowering of the chain growth probability due to WGS could effectively compensate for the enhancing effect of conversion (higher residence time) on chain growth probability [Todic et al., 2013].

Typically, LTFT application on cobalt catalyst shows a clear increase of selectivity towards heavier hydrocarbons (C_{5+}) and consequently a decrease in methane and lighter hydrocarbons. This behavior was originally justified by the occurrence of secondary reactions of 1-olefins promoted by the increase in the 1-olefin reactor residence time through chain length inhibited-diffusion or enhanced-solubility effect.

Moreover, a general decreasing effect of conversion on OPR has been widely reported by many authors. The promoting effect of conversion towards secondary reactions (in particular re-adsorption) could be the reason for the decrease in olefin formation and so in OPR. However, experimental results from Todici et al. [Todic et al., 2013] and Lodberg et al. on cobalt-catalyst showed as chain growth probabilities for all hydrocarbons α_{2+} except methane remain relatively constant increasing conversion (i.e. residence time) [Logdberg et al., 2010]. This suggests that secondary olefin re-adsorption could only have a negligible effect on FTS selectivity and, instead, changes in the kinetics of methane formation could be the root of changes in selectivity with conversion.

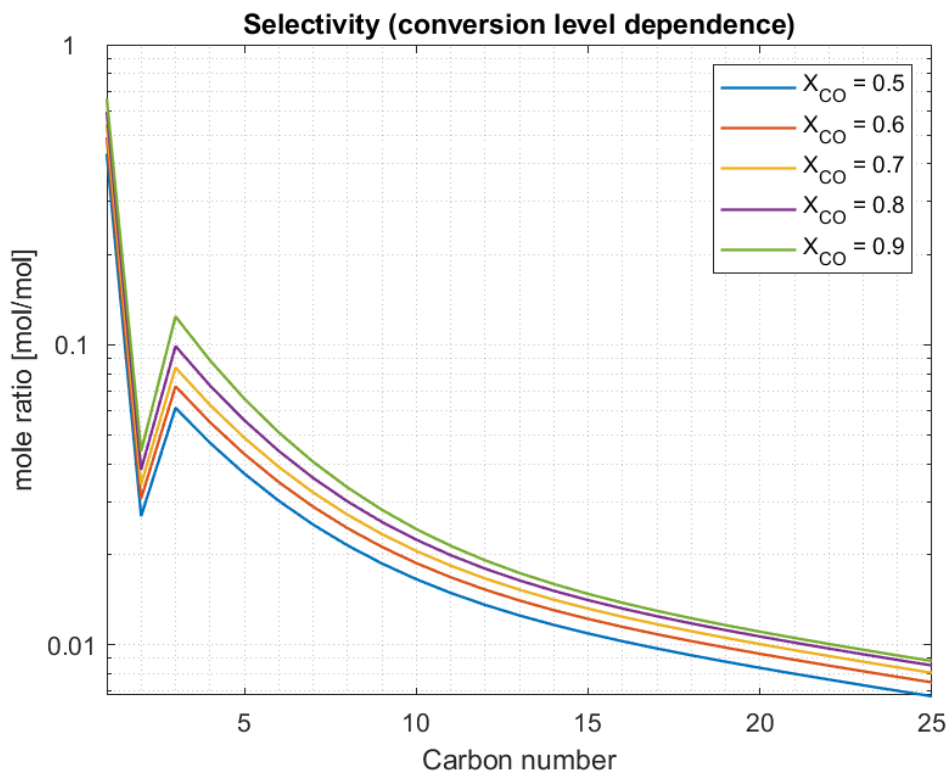


Figure 3.17: effect of varying process conversion in the FT cobalt-based reactor of the simulation model in this work ($T=230\text{ }^{\circ}\text{C}$, $H_2/CO = 2.078$, $P = 20\text{ bar}$) on hydrocarbon molar fractions with carbon number (a form of carbide mechanism from Todic et al. 2013).

4. FT WAX HYDROCRACKING

As we have seen before, there exist two effective ways to convert synthetic gas to liquid aliphatic hydrocarbons to be employed as transportation fuels.

Operating at high temperature (240 – 350 °C) yields hydrocarbons from C₁ to C₁₅ and usually the HTFT process is optimized for this purpose obtaining mainly light olefins or fuels in the gasoline range.

For low temperature (200 – 240 °C) application, instead, selectivity shifts towards long chain linear paraffins, widely enlarging the spectrum of products (> C₃₀), and usually the process is optimized for lowering as much as possible the selectivity of methane and lighter hydrocarbons in favor of heavier hydrocarbons. As a consequence a large fraction of FT products from low temperature FT technology have a boiling point higher than 350 °C.

Typically, the yield of diesel fuel (160 – 350 °C cut) from optimized Cobalt based LTFT application reaches up maximum 40 % [Bouchy et al., 2009]. Moreover, as a consequence of their paraffinic nature, FT derived middle distillate displays high cetane number (>75) but very poor flow properties at low temperature (CFPP – cold filter plug point and CP - cloud point) and thus it is not suitable to be directly used as blending component for diesel pool yet.

To increase the diesel yield, it may be convenient to run FT process to produce primarily waxes (chain growth probability close to 1) and then hydro-crack them to upgrade the wax and maximize the diesel fraction. This is achieved by cleavage of carbon-carbon bonds along the linear chain followed by saturation of the resulting fragments. These cracked products generally are formed by two successive reaction steps [Bouchy et al, 2009], i.e. isomerization and the actual cracking step.

The first reaction route leads to a marked improvement of cold flow properties because of the enrichment in branched paraffins (lower freezing point and CFPP) of the middle distillate fraction, while the middle distillate yields increase due to the proper cracking reaction and may range between 80 and 85 % at proper conditions and with suitable catalysts [Calemma et al., 2009].

4.1 Catalysts and operating conditions

The hydrocracking process is carried out over a bi-functional catalyst, characterized by two different active sites, properly [Coonradt et al., 1964]:

metal sites, which provide de/hydrogenation function or hydrogen activation function;
acidic sites (of the Brönsted type), where isomerization and cracking take place.

The metal can be a noble metal such as Palladium or Platinum or bimetallic systems of non-noble metals in the form of sulfides from group VIA (molybdenum, tungsten) and group VIIIA (cobalt, nickel) [Kumar, 2006]. The acidic support may be an amorphous oxide (in particular silica-alumina), crystalline zeolite or a mixture of both.

For crude oil processing only the base metal option can be applied because of significant content of Sulphur (and derived mercaptans) into the feed that would rather poison noble metal, whereas the amorphous silica-alumina option turns to be the only applicable due to the large size of the poly-cyclic feed molecules [Ndimande, 2004].

On the contrary FT derived waxes are generally Sulphur-free and aromatics and naphthenes are not produced by FT routes, so that more active metal catalysts such as noble metals (e.g. Platinum) and extremely porous acid phases such as crystalline zeolite could be employed. Possible compositions of a hydrocracking catalyst are shown in (Fig. 4.1).

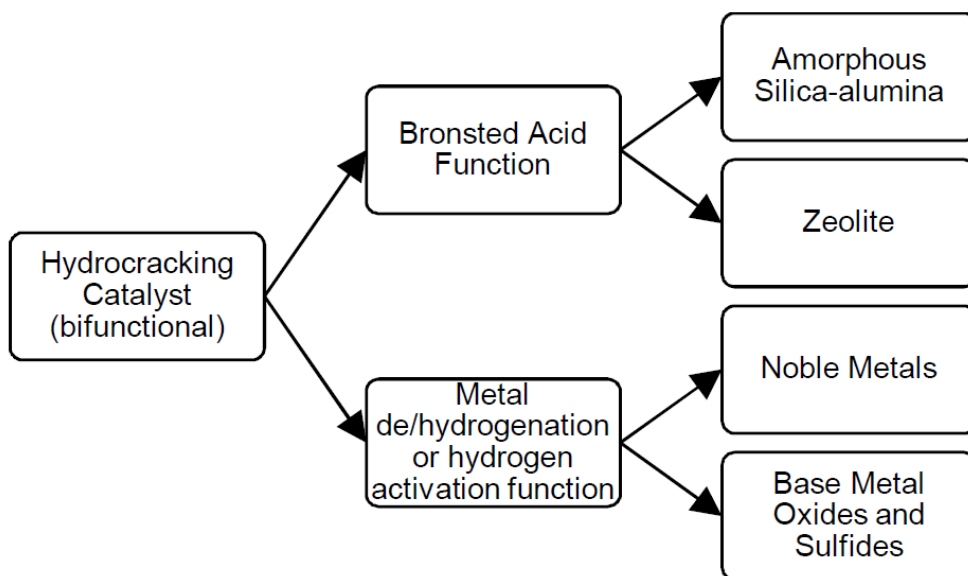


Figure 4.1: combinations of hydrocracking catalysts currently used [from Ndimande, 2004].

Moreover more active catalysts and higher activity of n-paraffins allow for carrying out the process at milder condition compared to hydrocracking of petroleum based feed stocks [Bouchy et al, 2009]: pressures may be lower (50-80 bar against 100-200 bar for mild and conventional hydrocracking, respectively) and the H_2 /feedstock ratio typically ranges between 400 and 800 m^3/m^3 against the deeper use of hydrogen in conventional reactors (800-2000 m^3/m^3).

Moreover conventional hydrocracking is conducted in a two stages process [Dufresne et al., 1987], in which a hydro-treatment step has the aim to convert poisoning organic Sulphur and nitrogen in the feedstock into H_2S and NH_3 and hydrogenate metals (such as vanadium and nickel) before the actual cracking step (350-430 °C). Instead mild hydrocracking and FT wax hydrocracking are generally carried out in a single stage process at about as the same temperature (340-440 °C) as for conventional reactors.

The process conditions are managed as to partially vaporize lighter hydrocarbons, those boiling in the diesel range and below, both for conventional hydrocracking and mild hydrocracking (such as for FT waxes). This implies much more limited catalyst contact time for these lighter molecules (typically the desired products) compared to the heavier feed molecules, which is well reflected by their low reactivity in the hydrocracking process [Eilers et al., 1990]. Consequently, the partial vaporization minimizes cracking of the lighter part of the feed and product (that is already boiling in the middle distillate range), guarantying significant cracking only of the heavy fraction of the feed.

Shell Middle Distillate Synthesis (SMDS) process plant, online since 1993, is an example of existing application of LTFT process including hydrocracking of LTFT wax for the increase and upgrade of the middle distillate production [Dry, 2002].

4.2 Reaction mechanism

A number of mechanisms have been proposed for the hydrocracking reactions but that proposed by [Wills et al., 1953] and [Weisz & Swegler, 1957] was generally thought to best represent the hydrocracking mechanism.

For the 'classical' scheme, as it is often referred to, the hydrocracking reactions occur on two separate and different sites via a series of intermediate diffusion and reaction steps between the metal and acid sites. The 'classical' scheme network starts when feed molecules are adsorbed into the pores of the acidic support from the surrounding fluid phase, which can be gas or liquid depending upon the reactor operating conditions. At this time the adsorbed paraffinic species are chemisorbed on the metal site and are dehydrogenated into the corresponding olefinic species. The olefin then desorbs and migrates by diffusion through the fluid phase to an acid site where olefin is protonated to the paraffinic carbenium ion [Kumar, 2006]. The paraffinic carbenium ion so produced is subjected to skeletal isomerization, in particular it can be isomerized by hydride shift (HS), methyl shift (MS) and protonated-cyclopropane (PCP) steps (fig. 4.2).

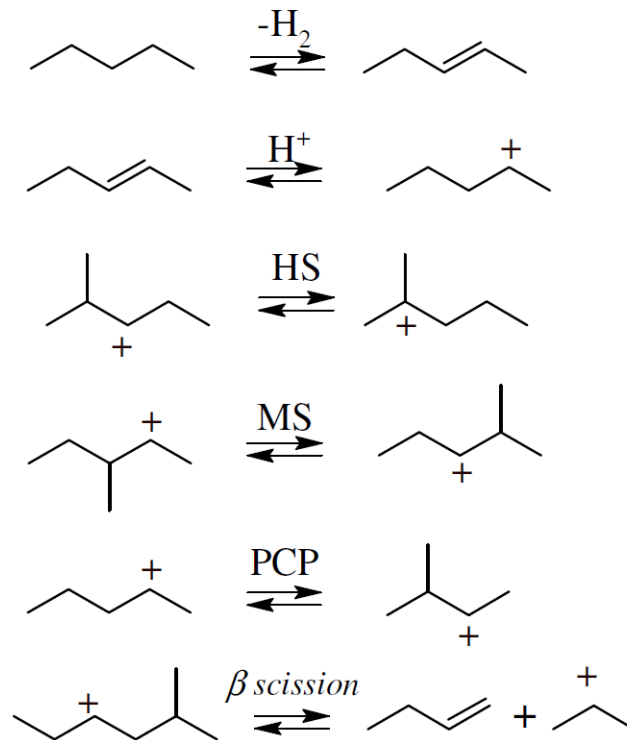
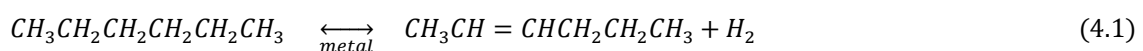


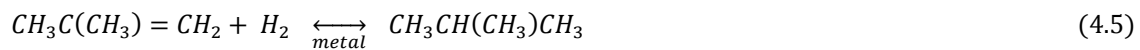
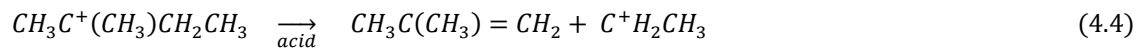
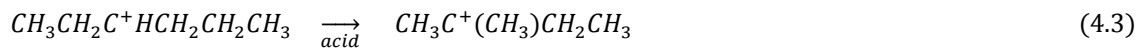
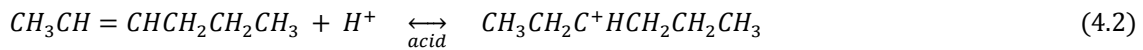
Figure 4.2: steps involved in the hydrocracking of paraffins (types of isomerization) [Kumer, 2006].

HS and MS do not modify the degree of branching in the carbenium ion whereas the PCP step generally adds a branch to the chain [Kumar, 2006]. The isomerized carbenium ion, with some degree of branching, cracks at the carbon-carbon bond in β position with respect to the carbon atom carrying the positive charge, resulting in a smaller carbenium ion and an olefin [Kumar, 2006]. This process is called β -scission (fig. 4.2) and it is recognized as the rate limiting step in the isomerization-cracking sequence.

It's clearly demonstrated that n-paraffins transformation occurs in successive steps, cracking being preceded by the branching of the skeleton, while direct cracking is neglected [Baltanas et al. 1983]. The carbenium ion fragment which results from cracking can undergo further cracking or deprotonation to olefin. Hence, the olefin can be then protonated to form a carbenium ion or can desorb from the acid site and migrate by fluid phase diffusion to a metal site where it is hydrogenated to paraffin [Weisz & Swegler, 1957] [Scherzer & Gruia, 1996].

Following is the aforementioned hydrocracking reaction sequence for n-hexane:





The probability to undergo either hydrogenation or protonation depends of the relative strength of the acid/metal function catalyst. In other words selectivity of isomerization/cracking and in turn the distribution of the reaction products depends on the number of acidic sites that the olefinic intermediates can encounter during their diffusion through between two hydrogenating sites (i.e. metal sites) and therefore on the acid sites / hydrogenating sites ratio [Guisnet et al., 1987].

4.2.1 Kinetic model approaches

The hydrocracking process over bi-functional catalyst has been extensively studied and many studies focusing on the formation of hydro conversion of n-paraffins from petroleum fractions are available since 60s.

Due to the complexity of heavy petroleum fractions, a "discrete lumping" process scheme was the first approach adopted in order to formulate reaction kinetics for hydro conversion units [Kumar, 2006]. According to this approach, the feedstock is divided into several lumps based on the boiling point range. Hence, a simplified reaction networks is set up and the rate coefficients for the global conversion of lump are estimated from the experimental data.

To achieve higher accuracy in the product yields predicted by the models, more and more lumps were introduced by various researchers. But increasing the number of lumps also leads to the introduction of more parameters in the kinetic model [Kumar, 2006]. Nevertheless, the kinetic parameters thus derived depend on the composition of the feedstock, thus the model has to be refitted each time a different feedstock is used and the set of parameters to be estimated again.

Another approach for modelling the kinetic of the conversion of complex petroleum feedstock was based on the notion of "continuum lumping". In this case the reaction mixture is considered to be a continuous mixture with respect to the feed properties like boiling point and molecular weight. A hydrocracking model based on this approach has been developed by Laxminarasimhan et al. [Laxminarasimhan et al., 1996], in which the true normal boiling point of the mixture was used as characterization parameter for each cut and the rate constant of hydrocracking was assumed to be a monotonic function of the true boiling point. As in the case of discrete lumping, last approach is unable to capture the mechanistic details of the process, basically leading a downfall of the prediction of the product formation and reactant consumption rates [Kumar, 2006].

Mechanistic models are based more closely on the chemistry of the process. Froment and coworkers developed a mechanistic kinetic modeling approach starting from the elementary steps of carbenium ion chemistry [Baltanas et al., 1989; Feng et al., 1993]. This approach was known as "single event kinetics", a network of elementary reactions designed to take into account the formation of each single component of the product mixture. It was selected by Baltanas et al. to generate the network of elementary steps involving carbenium ions and using computer algorithms based on the approach proposed by Clymans et al [Clymans et al., 1984]. Also Martens et al. applied the single event approach to predict the rate of hydrocracking for C₈-C₁₂ n-paraffins on Pt/USY zeolites [Martens et al., 2000], while Feng et al. modelling the process on RE-Y zeolite catalyst [Feng et al., 1993]. This last mechanistic model could be barely employed to modelling the hydrocracking of a varied hydrocarbons mixture, as in the case of FT waxes [Pellegrini et al., 2008].

A "single event kinetics" approach based on [Pellegrini et al., 2008] has been adopted for the modelling of hydro-cracking of FT waxes in the current simulation of a Gas-to-Liquids plant.

5. GTL PLANT MODEL DESCRIPTION

The simulation of a Gas-to-Liquids (GTL) process, such as that in this work, includes three stages: a reforming section, where natural gas is reformed through simultaneous steam-based methane reforming (SMR) and CO₂-based methane reforming (CDR) to produce syngas; a FT synthesis unit to produce fungible liquid fuels and waxes and a last section for hydro-cracking of the FT waxes, changing them into a shorter length and adding branches to the linear chain. In between these sections there are distillation units for separation of the hydrocarbon mixtures into the various main fuel cuts (naphta, middle distillate and waxes).

The simulation has been conducted using ASPEN Plus, a commercially available process simulator for process analysis. It contains a rigorous thermodynamic and transport property database set and provides comprehensive built-in process models for system modelling, integration and optimization. Process components of the simulation were implemented in Aspen Plus using standard, built-in unit operation modules including all the components present in the process, such as heat exchangers, pumps and compressors.

Aspen Simulation Engine solves heat and mass balance at unit operation level in order to obtain state variable (composition, pressure, temperature) and thermodynamic (i.e. enthalpy, entropy, Gibbs free energy) and/or transport variables for outlet mixture stream and the energy flow rate across the system.

Assumptions for the simulation process are considered as following:

- The process is steady state and isothermal and input flow rate of natural gas, water and carbon dioxide are constant;
- The process used FTS and hydro-cracking catalysts that are composed of homogeneous catalyst and the catalyst was charged with constant void fraction of catalyst bed in FT reactor;
- The process analysis does not have regard for heat and mass transport phenomena occurring at unit operation level and related properties (i.e. viscosity, surface tension, heat conductivity).

For simulating a generic chemical process, first step is to define all chemical species entering and produced within the process.

5.1 Chemical components

Generally, chemical compounds involved in a GTL and upgrading process are light gases (H₂, CO, CO₂), water, hydrocarbons (paraffin, olefin, methyl-alkanes) and organic oxygenated species (alcohols, aldehydes, carboxylic acids and ketones) to a minor extent. The last group of chemical components is not considered in the present process simulation. The chemical compounds are 180 in total (39 olefins, 70 paraffins, CO, H₂, H₂O, CO₂ and 67 methyl-alkanes) and the molecular formula for each of them is showed in (Tab. 5.1).

Table 5.1: molecular formula for each of the chemical components involved in the process. Blue formulas: components whose properties are estimated by literature correlations (Cap. 5.4) and/or PCES. Black formulas: components whose properties are retrieved from Aspen databanks (APEN DB-PURE 36).

n-ALKANES (n-paraffins)	n-ALKENES (n-olefins)	MONO-METHYL ALKANES	UNCOND. GASES & WATER
CH ₄	C ₂ H ₄	C ₄ H ₁₀	CO
C ₂ H ₆	C ₃ H ₆	C ₅ H ₁₂	H ₂
C ₃ H ₈	C ₄ H ₈	C ₆ H ₁₄	O ₂
C ₄ H ₁₀	C ₅ H ₁₀	C ₇ H ₁₆	N ₂
C ₅ H ₁₂	C ₆ H ₁₂	C ₈ H ₁₈	H ₂ O
C ₆ H ₁₄	C ₇ H ₁₄	C ₉ H ₂₀	CO ₂
C ₇ H ₁₆	C ₈ H ₁₆	C ₁₀ H ₂₂	
C ₈ H ₁₈	C ₉ H ₁₈	C ₁₁ H ₂₄	
C ₉ H ₂₀	C ₁₀ H ₂₀	C ₁₂ H ₂₆	
C ₁₀ H ₂₂	C ₁₁ H ₂₂	C ₁₃ H ₂₈	
C ₁₁ H ₂₄	C ₁₂ H ₂₄	C ₁₄ H ₃₀	
C ₁₂ H ₂₆	C ₁₃ H ₂₆	C ₁₅ H ₃₂	
C ₁₃ H ₂₈	C ₁₄ H ₂₈	C ₁₆ H ₃₄	
C ₁₄ H ₃₀	C ₁₅ H ₃₀	C ₁₇ H ₃₆	
C ₁₅ H ₃₂	C ₁₆ H ₃₂	C ₁₈ H ₃₈	
C ₁₆ H ₃₄	C ₁₇ H ₃₄	C ₁₉ H ₄₀	
C ₁₇ H ₃₆	C ₁₈ H ₃₆	C ₂₀ H ₄₂	
C ₁₈ H ₃₈	C ₁₉ H ₃₈	C ₂₁ H ₄₄	
C ₁₉ H ₄₀	C ₂₀ H ₄₀	C ₂₂ H ₄₆	
C ₂₀ H ₄₂	C ₂₁ H ₄₂	C ₂₃ H ₄₈	
C ₂₁ H ₄₄	C ₂₂ H ₄₄	C ₂₄ H ₅₀	
C ₂₂ H ₄₆	C ₂₃ H ₄₆	C ₂₅ H ₅₂	

C23H48	C24H48	C26H54	
C24H50	C25H50	C27H56	
C25H52	C26H52	C28H58	
C26H54	C27H54	C29H60	
C27H56	C28H56	C30H62	
C28H58	C29H58	C31H64	
C29H60	C30H60	C32H66	
C30H62	C31H62	C33H68	
C31H64	C32H64	C34H70	
C32H66	C33H66	C35H72	
C33H68	C34H68	C36H74	
C34H70	C35H70	C37H76	
C35H72	C36H72	C38H78	
C36H74	C37H74	C39H80	
C37H76	C38H76	C40H82	
C38H78	C39H78	C41H84	
C39H80	C40H80	C42H86	
C40H82		C43H88	
C41H84		C44H90	
C42H86		C45H92	
C43H88		C46H94	
C44H90		C47H96	
C45H92		C48H98	
C46H94		C49H100	
C47H96		C50H102	
C48H98		C51H104	
C49H100		C52H106	
C50H102		C53H108	
C51H104		C54H110	
C52H106		C55H112	
C53H108		C56H114	
C54H110		C57H116	
C55H112		C58H118	
C56H114		C59H120	
C57H116		C60H122	
C58H118		C61H124	
C59H120		C62H126	
C60H122		C63H128	
C61H124		C64H130	
C62H126		C65H132	
C63H128		C66H134	
C64H130		C67H136	
C65H132		C68H138	
C66H134		C69H140	
C67H136		C70H142	
C68H138			
C69H140			
C70H142			

The thermodynamic (or transport) property data for some of these molecules are not present in Aspen Property System databanks, where they are usually stored and which they are commonly retrieved from. In detail, for olefins with odd carbon number from C21 to C40, for methyl-alkanes from C21 to C70 and alkanes from C31 to C70 physical property parameters are not available within the common Aspen Physical Property

databases (Aspen PURE and Aspen HYSIS databases). As a matter of fact, pure component constants (such as molecular weight (MW), normal boiling temperature (TB), critical temperature (TC), critical pressure (PC), critical volume (VC), acentric factor (OMEGA)) and temperature-dependent property correlation parameters (such as DIPPR correlation for ideal gas capacity, vapor pressure and heat of vaporization) can be estimated within the ASPEN Plus Property environment by means of two different Aspen Property tools: PCES (Property Constant Estimation System) and/or TDE (Thermo-Data-Engine).

PCES is an Aspen Physical Property System tool based on *group contribution* concept and the *corresponding-state theory* approach for computing of all property data from a minimum of information about the molecule (typically molecular structure and molecular weight are sufficient). Like PCES, TDE uses the same approach to evaluate the property data but it also contains an automatic service to update property data to more recent published experimental ones (known as dynamic data evaluation).

Aspen Property Constant Estimation system and Thermo-Data-Engine compute thermodynamic or transport property parameters for models and/or methods by means of a summing procedure of property contribution of all functional groups (type and occurrence) making up the molecule (within *Properties/Estimation/Input/Setup* sheet *Estimate all missing parameters* should be typed to allow built-in group contribution methods to evaluate thermodynamic Pure Component Constant and parameters for Temperature Dependent properties that are necessary for all the physical property models and methods).

In this work, parameter estimation by PCES Aspen Property tool has been applied to evaluate some of the thermodynamic property data necessary to solve mass and energy balances. PCES methodology has been initially applied to each methyl-alkane molecule (C4-C70) and to each of the paraffins and olefins with carbon atom number higher than fifteen (C15-C70 for paraffins and C15-C40 for olefins). This choice is due to unrealistic results found for some values of pure component critical constants (TC and PC) for even-not-so-heavy hydrocarbon as computed by NIST Thermo-Data-Engine model equations (TDE – Thermo-Data-Engine of US National Institute of Standard and Technology represents the alternative option to Property Constant Estimation system in evaluating Pure Component and Temperature Dependent constant parameters for all those molecules which are not present within common ASPEN Plus databases). Further reason for evaluating compound property parameters by means of Aspen Property Estimation

system has been found to come up with a better consistency of estimation results for molecules of similar size.

The databases which almost all of the used physical property parameters for molecules up to thirty carbon atom are stored in are PURE36 for Pure Component and Temperature Dependent parameters and VLE-RK , EOS-LIT and LLE-ASPEN for Binary Interaction parameters.

A minimum of information is required by group contribution models (CGM) used by PCES for parameter assessment: Molecular Weight MW, Molecular Structure and/or Normal Boiling Point TB. Generally PCES results much more accurate (i.e. it reduces the propagation of errors) in estimating other parameters by using an experimental (or accurate enough) value for TB. Fortunately, even if one does not supply TB and MW but enters the general molecular structure, Property Estimation can estimate TB and MW.

There are different ways to enter the general molecular structure of chemical components to Aspen Property System: the first could be by drawing the structure within the *Molecular Structure/Structure* sheet. Another one might be by importing each missing structure in a specific (.mol) file format from online chemical compound databases, such as (PubChem ,2018) or (ChemSpider, 2018) into the ASPEN Plus Molecular Editor (available under *Components/Molecular Structure/Structure* ribbon in the Property environment). The second option has been adopted to enter molecular structure of some chemical components (in blue typed formula in Tab. 5.1) in this work and an example of the ASPEN Plus drawing interface (Molecular Editor) is reported for n-hexatriacontane in (Fig. 5.1).

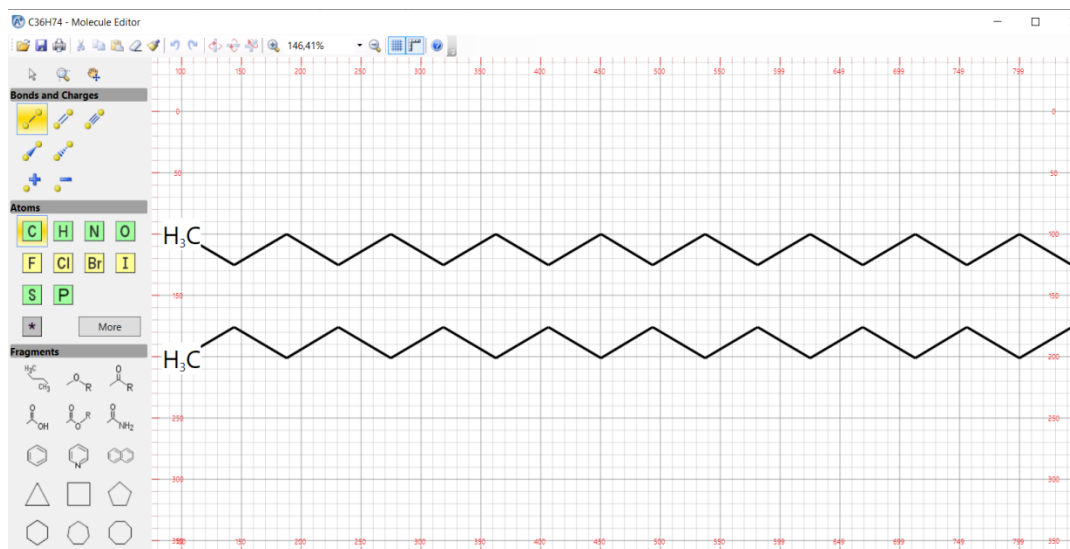


Figure 5.1: ASPEN Plus Molecular Editor GUI for providing molecular structure of n-hexadecane to Aspen Property Estimation System (PCES and NIST/TDE).

Alternately, one can use the general method (entering atoms and bonds on *General* sheet) or by specifying functional groups (choosing a functional group and indicating the occurrences on *Functional Group* sheet), but the latest is less preferred from Aspen Property System (AspenPlusV10 Help).

5.2 Property method

Equations and sets of equations used to calculate physical properties in the Aspen Physical Property System are strictly divided into methods and models.

A *method* is based on universal scientific principles only, and may need other properties (such as T_C and P_C) and state variables (T , p , composition) but not correlation parameters to calculate a specific property.

Instead, a *model* is something less universal and more specific property-related and includes state variables, properties and (empirical or semi-empirical) correlations as input variables.

Into Aspen Physical Property System methods and models are used to calculate thermodynamic and transport properties and they are packaged in *property methods*. Each property method contains all the methods and models for the calculation of all physical properties needed for simulating purpose.

Each property method is based on either the equation-of-state method or the activity coefficient method mainly on how properties (i.e. fugacity) are derived for vapor-liquid equilibrium calculation (as for flash, bubble or dew point calculation). With an equation-of-state method, these properties are derived from an equation of state, for both vapor and liquid phases. Instead, activity coefficient method provides an equation of state for vapor properties, whereas it employs a summation procedure of the pure component properties to which an excess term is added in the case of liquid phase. Generally, activity-coefficient-models are applicable to low pressures and are able to correlate polar mixtures or mixtures of polar and nonpolar components, while equation-of-state methods are suitable for nonpolar or slightly polar mixtures from low to high pressures (ASPEN Plus v10Help).

The simulation process in this work involves light gas and heavy hydrocarbon mixtures at high pressure and relatively-high temperature within synthesis or cracking reactors whereas low pressures and higher temperatures are expected along the separating columns. In such a range of conditions (especially at high pressure) encountered by complex mixtures of nonpolar and heavier compounds and permanent gases (CO₂, CO, H₂), one should expect inter-molecular forces to play a major role in affecting the fluid behavior and the phase equilibria along separators and within reactors. Generally, attraction and repulsion inter-molecular forces are responsible for the deviation of fluid behavior from the ideal case of no mutual influence (i.e. ideal-gas-law) between molecules and both high pressure and voluminous and elongated-shape molecules enhance that diverging.

Starting from the ideal gas law, Van der Waals first took into account the fact that molecules occupy space and that they exert an attraction on each other, introducing the inter-molecular forces effect into the ideal gas law expression as following:

$$\text{Van der Waals: } p = \frac{RT}{(V - b)} - \frac{a}{V^2} \quad (5.1)$$

Wherein it appears that the pressure results from a repulsive term $\frac{RT}{(V - b)}$ and an attractive term $\frac{a}{V^2}$.

The constant (temperature independent) term b is the *co-volume* and represents the molar volume that molecules exclude by their mutual repulsion. The molecular forces are incorporated in the model by the a -coefficient. Writing the critical constraints (i.e. that the molar volume does not vary no more with varying pressure at the critical point), it

becomes possible to express a and b parameters as function of the experimental values T_c and P_c , strictly characterizing the fluid: $a = \frac{27}{64} * R^2 T_c^2 / P_c$ and $b = \frac{1}{8} * R T_c / P_c$.

Van der Waals equation (1883) was the first example of *cubic equation of state*, followed by numerous modifications all through the years that resulted in possible ways to improve the model accuracy. Already in 1880, Clausius proposed a modified form in which a temperature inverse proportion for the attractive parameter (a) and a constant (c) to the volume dependency were added in the attractive part.

$$\text{Clausius: } p = \frac{RT}{(V-b)} - \frac{a/T}{(V+c)^2} \quad (5.2)$$

In the middle of 20th century, Redlich and Kwong (1949) introduced a deeper dependence on temperature in the attractive term of Van der Waals equation:

$$\text{Redlich - Kwong: } p = \frac{RT}{(V-b)} - \frac{a(T)}{V(V+b)} \quad (5.3)$$

Wherein

$$a(T) = a_c * \alpha(T) \quad (5.3.1)$$

$$b = 0,08664 R T_c / P_c \quad (5.3.2)$$

$$a_c = 0,4274 R^2 T_c^2 / P_c \quad (5.3.3)$$

$$\alpha = \sqrt{T_c/T} \quad (5.3.4)$$

Namely α is called "alpha function" and its expression has been derived pointing its value to unity in the RK EoS (eq. 5.3) at the critical point.

Hence, only two critical parameters (experimentally derived) are employed to derive the attractive term $a(T)$ (eq. 5.3.4), properly the critical temperature and pressure (T_c and P_c).

By then, Redlich-Kwong model was widely employed for a long time due to its improved accuracy for predicting very-well the pure-components vapor pressures of hydrocarbon and petroleum fractions from low to high pressures. However, the model seemed to exhibit much less accuracy whenever the acentric factor ω for a fluid was far from zero. Typically, the acentric factor is used to take into account molecular size and shape effects

since it varies with the chain length and the spatial arrangement of the molecule (small globular molecules have a nearly zero acentric factor). It is defined by Pitzer as:

$$\omega = -\log\left(\frac{P_{sat}(T = 0.7T_c)}{P_c}\right) - 1 \quad (5.4)$$

In the 1972, Italian engineer Soave, on the bases of the fact that different fluids showed different behavior for the same value of reduced temperature T_r and pressure P_r , proposed to introduce the acentric factor in the definition of $\alpha(T)$, turning from a two-parameter EoS (T_c and P_c) to a three-parameter EoS (T_c , P_c , ω). The resulting equation-of-state was named Soave-Redlich-Kwong (SRK) and the alpha function so defined took the name of *Soave alpha function*:

$$\alpha(T) = [1 + m(1 - \sqrt{T/T_c})]^2 \quad (5.5)$$

Where the dependence on the acentric factor of the attractive term was incorporated in the m coefficient:

$$m = 0.480 + 1.574 \omega - 0.176 \omega^2 \quad (5.6)$$

As it is, SRK EoS model was able to represent the fluid behavior of few polar and few associated molecules also (paraffins, naphthenic, aromatics, permanent gases). It is employed at each unit operation model in the current ASPEN Plus simulation workspace just because of the absence of polar compounds containing nitrogen and oxygen, the opposite of what occurs for petroleum derived fractions, where polar compounds may range between 1 and 20 wt %.

Extension to mixtures requires *mixing rules* for the energy (attractive) parameter and the co-volume. One way to extend the cubic EoS to a mixture containing n components, the mole fractions of which are x_i , is via the so-called Van der Waals one-fluid mixing rules (quadratic composition dependency for a and b parameters) and the classical mixing rules, i.e. the geometric mean rule for the *cross-energy* a_{ij} (eq. 5.8.3) and arithmetic mean rule for the *cross-volume* b_{ij} (eq. 5.8.5).

$$p = \frac{RT}{(V_m - b)} - \frac{a}{V_m(V_m + b)} \quad (5.8)$$

Where $a = a_0 +$

$$a_1. \quad (5.8.1)$$

a_0 is the standard quadratic mixing term and a_1 is the asymmetric (polar) term:

$$a_0 = \sum_{i=1}^n \sum_{j=1}^n x_i x_j a_{ij} \quad (5.8.2)$$

$$a_{ij} = \sqrt{a_i a_j} (1 - k_{ij}) \quad (5.8.3)$$

$$a_1 = \sum_{i=1}^n x_i (\sum_{j=1}^n x_j (\sqrt{a_i a_j} l_{ij})^{1/3})^3 \quad (5.8.4)$$

$$b = \sum_{i=1}^n \sum_{j=1}^n x_i x_j b_{ij} \quad (5.8.5)$$

$$b_{ij} = \frac{1}{2} (b_i + b_j) (1 - l_{ij}) \quad (5.8.6)$$

As can be seen, in the cross-energy and cross-volume mixing term (mixing rules) two new parameters appeared, the so-called *binary-interaction parameters* ($k_{i,j}$ and $l_{i,j}$). Among the two, when concerning not or few polar mixtures like mixture of hydrocarbons and permanent gases, only $k_{i,j}$ should be not-null and $l_{i,j}$ can be neglected. In this work, since each of the molecules involved is not polar (being absent particularly electronegative atoms, such as oxygen, in the molecule structure) the mixture can be considered not polar also and the last simplification can be applied. In this way the co-volume term simplifies to:

$$b = \sum_{i=1}^n x_i b_i \quad (5.8.7)$$

It is well-known that the $k_{i,j}$ parameter has a great influence on fluid-phase equilibrium calculation, although some authors opined that this dependence is quiet moderate for mixture of n-alkanes. However, it results far from zero for systems containing CO_2 and various hydrocarbons, and for H_2 -hydrocarbons mixtures, as occurs in a GTL plant, especially when CO_2 is employed as reactant (such as in CDR reactor, i.e. carbon dioxide based methane reforming) for syngas production and hydro-cracking is the option for FT wax upgrading. Furthermore, for a better prediction of fluid phase behavior of mixtures of heavy hydrocarbons, also the dependence on temperature of that interaction binary parameter should be considered (the temperature dependence of binary parameters for chemical compounds involved in this simulation work has not been evaluated nor regressed).

In order to improve the liquid molar volume prediction for pure compounds and then for mixtures, Peneloux *et al.* proposed to translate the equation of state adding a *volume translation* term to molar volume in the EoS (eq. 5.8), thus replacing V by $(V + c)$ and b by $(b + c)$, so that:

$$V = V_m - c \quad (5.9)$$

Where V_m is the mixture molar volume as computed by EoS (eq. 5.8) while the correction term c :

$$c = \sum_i x_i \cdot c_i \quad (5.9.1)$$

where

$$c_i = \frac{RT_{c,i}}{P_{c,i}} [0.1156 - 0.4077 z_{RA,i}] \quad (5.9.2)$$

Where z_{RA} is recognized as Rackett compressibility factor [Soave, 1972].

5.3 Property constant estimation (PCES)

It is clear from the expression above, that critical properties, acentric factor and liquid vapor pressures are the most important properties to be considered in order to obtain correct prediction of the pure component fluid behavior, even though the critical point is mostly never reached in practical applications.

Correct values for critical properties are necessary to efficiently compute the coefficients of the cubic equation of state, whereas high quality prediction of vapor pressure is one of the key properties for the correct design of distillation columns and it is also related to other properties, such as the latent heat of vaporization. Moreover critical properties, such as critical temperature and pressure, are required by mixing rule in the cubic equation of state for mixtures and important data such as vapor pressure, heat of vaporization and density are generally estimated by correlations (in particular, those based on corresponding state theory) requiring properties at critical point.

However, experimental data for critical properties are only available for smaller molecules because the larger and strongly associating ones tend to decompose (chemically degrade) before having reached the critical point. For example, C_{11+} n-paraffins tend to decompose, whereas C_{8+} n-olefins polymerize at elevated temperatures.

Furtherly, synthesis of sufficiently pure material is already very expensive and time consuming for these molecules and their thermal instability at near their critical point makes measurements much more difficult and in many cases impossible. For these reasons, there was and actually is great interest in developing estimation methods aiming to derive critical properties and vapor pressure data from basic and measurable features, such as molecular structure and/or normal boiling temperature.

There is a variety of estimation methods for critical property data available in the open literature. Of these, *group contribution* based methods have enjoyed the widest application over the world and they are effectively used as built-in models by Aspen Physical Property System (PCES and NIST/TDE) for estimating Pure Component Constants (not only at critical point) and correlative parameters for Temperature - Dependent properties of each of the chemical components whose these quantities are not retrieved from Aspen property databanks nor regressed from experimental data.

There is a variety of group-contribution-methods applied by PCES or TDE to evaluate the same constant property or the same set of parameters for a temperature-dependent property. Each of these methods differs from the others mainly for the particular set of functional groups that are used for fragmentation of the molecule and whether

interaction between different groups is considered (second-order CGMs) or not (first-order CGMs) into the group contribution.

Group contribution methods that are most applied are: Joback, Lydersen, Ambrose, which are first-order methods, and Gani, a method of the second-order. (Fig. 5.2) shows the (carbon) functional groups which are used by Joback method. They are clearly distinguished between non-ring increments groups, which are functional group inserted along an aliphatic chain, and ring-increments, that are more properly corrections for the functional groups when inserted in aromatic or poly-aromatic rings.

Table 3.5 Joback Method Functional Groups

Functional Group	Group Number
Nonring Increments	
·CH ₃	100
>CH ₂	101
>CH-	102
>C<	103
=CH ₂	104
=CH-	105
=C<	106
=C=	107
≡CH	108
≡C-	109
Ring Increments	
>CH ₂	110
>CH-	111
>C<	112
=CH-	113
=C<	114

Figure 5.2: some of the functional groups used by Joback group-contribution-method and their respective group number [from ASPEN Phys.Prop.Data, v.10.1-0; Reid et al., 1987].

5.3.1 Pure component Constant properties

Among the Pure Component constant parameters, molecular weight (MW) is directly and easily computed by PCES from summing up atom weights in the molecular formula.

Normal boiling point (T_B) is easily measurable and widely reported on literature data. Since its relevance for the estimation of critical constants, the user is greatly recommended to enter an experimental value (directly into *Properties/ Methods/ Parameters/ Pure Component* sheet) (ASPEN Phys.Prop.Meth.&Mod., v.10.1-0).; otherwise normal boiling point is estimated, by default, by Joback CGM (group-contribution-method). The Joback method is a first-order group contribution method, in the sense that it considers only contribution from single functional groups (first-order groups), without having regards for interactions between groups (second-order groups). Generally, CGM' s taking into account the contribution of neighboring groups/atoms by second-order groups (such as Gani method) results in higher accuracy. Moreover, only molecular structure is needed for these methods (ASPEN Phys.Prop.Meth.&Mod., v.10.1-0).

Also when estimating critical properties (critical temperature, pressure and volume), second-order CG-methods showed higher accuracy than first-order methods, requiring only molecular structure as input. Instead, first-order methods (Joback, Lydersen, Ambrose, Simple methods) provided by PCES for estimating critical temperature (T_C) require also normal boiling point as input, showing less accuracy than Gani method anyway. Among the first-order method, Ambrose yields small errors (0.7 [%] for average relative error or average error of 4.3 [K] over 400 organic compounds) than Joback and Lydersen methods, but is more difficult to use (more functional groups) (ASPEN Phys.Prop.Meth.&Mod., v.10.1-0).

For estimating the critical pressure (P_C), Joback needs only structure to work and it is simpler to use, but it shows less accuracy than Lydersen or Ambrose (4 [%] and 4.6 [%] for the average errors over almost 400 organic compounds) (ASPEN Phys.Prop.Meth.&Mod., v.10.1-0).

The same considerations don' t hold for critical volume (V_C): Joback method, based on the same functional groups of Lydersen, results more accurate than Ambrose method (2.3[%] and 2.8[%] for the average relative error respectively) (ASPEN Phys.Prop.Meth.&Mod., v.10.1-0).

The equations selected by Joback and Reid (1987) to predict normal boiling temperature, critical temperature, pressure and volume are reported here:

$$T_B = 198 + \sum_i N_i C_i \quad (5.10)$$

$$T_c = \frac{T_B}{0.584 + 0.965 \sum_i N_i C_i - (\sum_i N_i C_i)^2} \quad (5.11)$$

$$P_c = \frac{1}{(0.113 + 0.0032 n - \sum_i N_i C_i)^2} \quad (5.12)$$

$$V_c = 17.5 + \sum_i N_i C_i \quad (5.13)$$

As can be noted, they assumed no interaction between groups, and structurally-dependent parameters are thereby determined by summing up the number of frequency (N_i) of each group multiplied by its group contribution (C_i). Joback and Reid employed only 41 functional groups, that is insufficient to capture the structural effect of organic molecules and generally led to extremely inaccurate results when considering larger, complex or multi-functional molecules. The only advantage of the method lies in its simplicity but poor prediction and unrealistic extrapolation, (as can be observed from (Fig. 5.3-5.6) showing a comparison between different property estimation techniques) leads to its downfall (ASPEN Phys.Prop.Meth.&Mod., v.10.1-0).

Once critical pressure and temperature are available, PCES can estimate the acentric factor by the general formula by Pitzer (by default) (eq. 5.4) (thus vapor pressure parameters should be available also) or by Lee-Kesler group contribution method if dealing with hydrocarbons (in this case normal boiling temperature is needed in the place of vapor pressure).

All PCES built-in models (Benson, Joback, Gani) for evaluating the reference thermodynamic state (enthalpy and Gibbs free energy of formation at 298 [°C] and 1 [atm]) require only molecular structure to work. In particular for enthalpy of formation (DHFORM) the Benson method (second-order method) is recommended (Benson reports the same average error value as Gani method) and it is effectively used by default (ASPEN Phys.Prop.Meth.&Mod., v.10.1-0).

Also for the free Gibbs energy of formation (DGFORM), only structure is required by the three methods (Benson, Joback or Gani) but the simpler and less accurate (5-10 kJ/mol of average error) Joback method is used by default.

5.3.2 Pure component Temperature-Dependent property constants

The pure component temperature dependent properties whose correlation parameters are estimated by PCES and that are useful for the simulation in this work are *the ideal gas heat capacity, heat of vaporization and liquid heat capacity* for solving energy rate balance and *molecular weight and liquid vapor pressure* for multi-phase equilibria (mass rate balance). The correlative models used by Aspen Physical Constant Property System (PCES) are the Ideal-Gas-Heat-Capacity-Polynomial (eq. 5.14-5.15) for the ideal gas heat capacity and the Extend Antoine model (eq. 5.16) for vapor pressure. The Watson equation (eq. 5.17) and a DIPPR correlation (5.18) are employed for representing the latent heat of vaporization and the liquid heat capacity as a function of temperature, respectively.

For estimating parameters (*Methods / Parameters / Pure Components / CPIG*) which relates *ideal gas heat capacity* ($C_{p,i}^{ig}$) to temperature (eq. 5.14-5.15), PCES automatically employs the second-order Benson group contribution methods, that with an average relative error of 1.1 [%] for 27 compounds reveals to be more accurate than first-order Joback method. Both methods require only molecular structure for fragmentation of the molecule into functional groups (ASPEN Phys.Prop.Meth.&Mod., v.10.1-0)..

$$C_{p,i}^{ig} = C_{1,i} + C_{2,i} \cdot T + C_{3,i} \cdot T^2 + C_{4,i} \cdot T^3 + C_{5,i} \cdot T^4 + C_{6,i} \cdot T^5 \quad C_{7,i} \leq T \leq C_{8,i} \quad (5.14)$$

$$C_{p,i}^{ig} = C_{9,i} + C_{10,i} \cdot T^{C_{11,i}} \quad T < C_{12,i} \quad (5.15)$$

The parameters (*Methods / Parameters / Pure Components / PLXANT*) for the Extend Antoine equation (eq. 5.16) to compute the *vapor pressure* (p_i^l) at different temperatures are estimated by means of Reidel method by default. This method is used when normal boiling temperature, critical temperature and pressure are available and it estimates parameters for the temperature dependency of vapor pressure by applying Reidel equation and the Plank-Riedel constrain at the critical point [ASPEN Phys.Prop.Meth.&Mod., v.10.1-0].

$$\ln(p_i^l) = C_{1,i} + \frac{C_{2,i}}{T + C_{3,i}} + C_{4,i} \cdot T + C_{5,i} \cdot \ln(T) + C_{6,i} \cdot T^{C_{7,i}} \quad (5.16)$$

The range of temperatures within the use of Riedel-Plank method is recommended vary from the normal boiling point to the critical temperature and the validity of the results is restricted to nonpolar compounds. For polar molecules Li-Ma group contribution method appears to be more accurate (0.61 [%] of average relative error for 28 compounds), [ASPEN Phys. Prop. Meth. & Mod., v.10.1-0].

The parameters (*Methods /Parameters /Pure Components / DHVLWT*) necessary to Watson equation (eq. 5.17) to compute *latent heat of vaporization* $C_{p,i}^l$ at different temperatures are estimated from the definition of heat of vaporization according to the Clausius-Clapeyron equation, thus requiring at least one vapor pressure data and critical temperature and pressure as input. The average relative error reported for 98 components is 1.8 [%] with using definition. If critical constants are not available, Veteri method might be used (providing TB and structure only). Otherwise, Li-Ma group contribution method is provided by PCES, for which structure and TB are the only information required. Last method is also more accurate than the other discussed, showing 1.05 [%] of average relative error on a sample of 400 compounds [ASPEN Phys.Prop.Meth.&Mod., v.10.1-0].

$$\Delta H_{vap,i}(T) = \Delta H_{vap,i}(T_1) \cdot \left(\frac{1 - T/T_{c,i}}{1 - T_1/T_{c,i}} \right)^{a_i + b_i (1 - T/T_{c,i})} \quad T \geq T_{min} \quad (5.17)$$

Wherein $\Delta H_{vap,i}(T_1)$ is the heat of vaporization at the temperature T_1 .

Also the accuracy for the *liquid heat capacity* estimation could influence the energy rate balances in the simulation. PCES estimates the constant parameters (*Methods /Parameters /Pure Components / CPLDIP*) for the DIPPR equation (eq. 5.18) involving a group contribution method by Ruzicka. This method has been tested over almost ten-thousand compounds achieving an average relative error of 1.9 [%] for nonpolar compounds. The model parameters are valid only from melting point to normal boiling temperature [ASPEN Phys.Prop.Meth.&Mod., v.10.1-0].

$$C_{p,i}^l = C_{1,i} + C_{2,i} \cdot T + C_{3,i} \cdot T^2 + C_{4,i} \cdot T^3 + C_{5,i} \cdot T^4 \quad C_{7,i} \leq T \leq C_{8,i} \quad (5.18)$$

For the equation-of-state methods that apply the Peneloux correction (for a better estimation of the *mixture liquid molar volume* (V_m^l) by the Racket equation (eq. 5.18), the

Rackett parameter of each component of the mixture (Z_i^{RA}) can be estimated by PCES by means of the Gunn-Yamada method. It determines saturated liquid molar volume at temperatures below T_c and it uses these values for extrapolating the Rackett parameter. If the selected property method includes equation-of-state methods and/or models (as with RKS EoS, utilized in this simulation work), the Rackett parameter is estimated from Gunn-Yamm method by default [ASPEN Phys.Prop.Meth.&Mod., v.10.1-0].

$$V_m^l = \frac{RT_c (Z_m^{RA})^{1 + (1-T_r)^{2/7}}}{P_c} \quad (5.19)$$

where

$$T_c = \sum_i \sum_j x_i x_j V_{c,i} V_{c,j} (T_{c,i} T_{c,j}) (1 - k_{ij}) / V_{c,m}^2 \quad (5.19.1)$$

$$\frac{T_c}{P_c} = \sum_i x_i \frac{T_{c,i}}{P_{c,i}} \quad (5.19.2)$$

$$Z_m^{RA} = \sum_i x_i Z_i^{RA} \quad (5.19.3)$$

$$V_{cm} = \sum_i x_i V_{c,i} \quad (5.19.4)$$

$$T_r = \frac{T}{T_c} \quad (5.19.5)$$

5.4 Property constant estimation models (applied)

The behaviour of the group contribution at describing constant properties, in particular at the critical point, has been analysed. The results for critical properties as computed from PCES models are then compared to that derived by applying specific hydrocarbon class correlative equations, arising from polymeric theory or that obtained by iterating procedure specifically developed [Soave, 1998].

The linear contribution to each property from increasing carbon number hydrocarbons, as shown by PCES results, turns to be unsuitable to accurately predict the behaviour of the longer chain molecules at the critical point. On the other side, the logarithmic behaviour shown by the hydrocarbon class-specific correlative equations is more in line with that based on correlation of empirical data.

Following are the procedures for computing critical properties and acentric factor out of ASPEN Plus environment. Therefore, critical properties (temperature, pressure) and acentric factor are directly written into the ASPEN Plus Property section under *Methods /Parameters /Pure Components*.

Instead, PCES is allowed for computing temperature dependent properties, such as ideal gas heat capacity, liquid heat capacity, heat of vaporization and liquid molar volume. Vapour pressure is also derived based on correlation of experimental data for a small fraction carbon number molecules per class [Kreglewski et al., 1961].

5.4.1 Alkanes

5.4.1.1 Normal boiling temperature

For what is concerning n-alkanes, normal boiling temperature estimation performed by PCES through contribution of Joback method had come up with values of T_B (normal boiling point) for C_{30+} alkanes too much high if compared to the experimental values given by Zwolinsky and Wilhoit [Zwolinski et al., 1971] or derived from Asymptotic Behaviour Correlation by Marano and Holder [Marano et al., 1997]. The erroneous values obtained by Joback method reflects the linear trend of normal boiling point with varying carbon number expressed into the equation above (eq. 5.10).

Instead, the K-L (Kreglewski-Zwolinsky) relations (eq. 5.20-5.21), which are based on normal boiling point T_B [K] of n-alkanes, showed more accuracy and ease of application [Kreglewski et al., 1961], as studies of Somayajulu, Kudchadker and Zwolinsky already revealed in the 60' s [Kudchadker et al., 1966].

Some years before then, Kurata and Isida, using Flory' s expression for the free energy of a polymeric chain, developed a 'hole theory' treatment for n-paraffin liquids and found that the effective length of a carbon skeleton chain should lie proportional to the two-thirds power of the number of carbon atoms ($n^{2/3}$) when $n > 5$ [Kurata et al., 1955]. The 'hole theory' (or lattice-fluid theory) and its improved version, the 'cell theory' , were the basis for relating critical properties of polymers to their chain size s (number of mers) and thus to carbon number by means of asymptotic correlations (ABC Asymptotic Behavior Correlations). The ABC correlations were properly developed by Marano and Holder later [Marano et al., 1997] and they will be discussed more in detail in the olefin section (Cap. 5.5.3).

Using these results, Kreglewski and Zwolinsky found that some physical properties (θ), such as the normal boiling point (T_B), the critical temperature (T_C), the critical pressure (P_C) and the Antoine vapor pressure constant B , follow the simple functional relation [Kreglewski et al., 1961]:

$$\theta_\infty - \theta = a \cdot e^{-bx} \quad (x = n^{2/3}) \quad (5.20)$$

$$\ln(\theta_\infty - \theta) = a' - b' * n^{\frac{2}{3}} \quad (5.21)$$

where $a' = \ln(a)$, $b' = 0,43429 * b$ and θ_∞ is the property for polymer at infinite carbon number $n = \infty$.

Moreover, the model behavior was in line with the asymptotic trend for T_B reported by Flory, Orwoll and Vry, according to which the limit was 1078 [K] for $n \rightarrow \infty$ [Flory et al., 1964].

The resulting equation for T_B of n-alkanes (applied for C_{30} - C_{70} n-alkanes in this work) has been derived based on correlation of data for C_7 - C_{30} alkanes from Kreglewsky and Zwolinsky [Soave, 1998]:

$$\ln(1078.7141 - T_B[K]) = 6.9811554 - 0.11483075 n^{2/3} \quad (5.22)$$

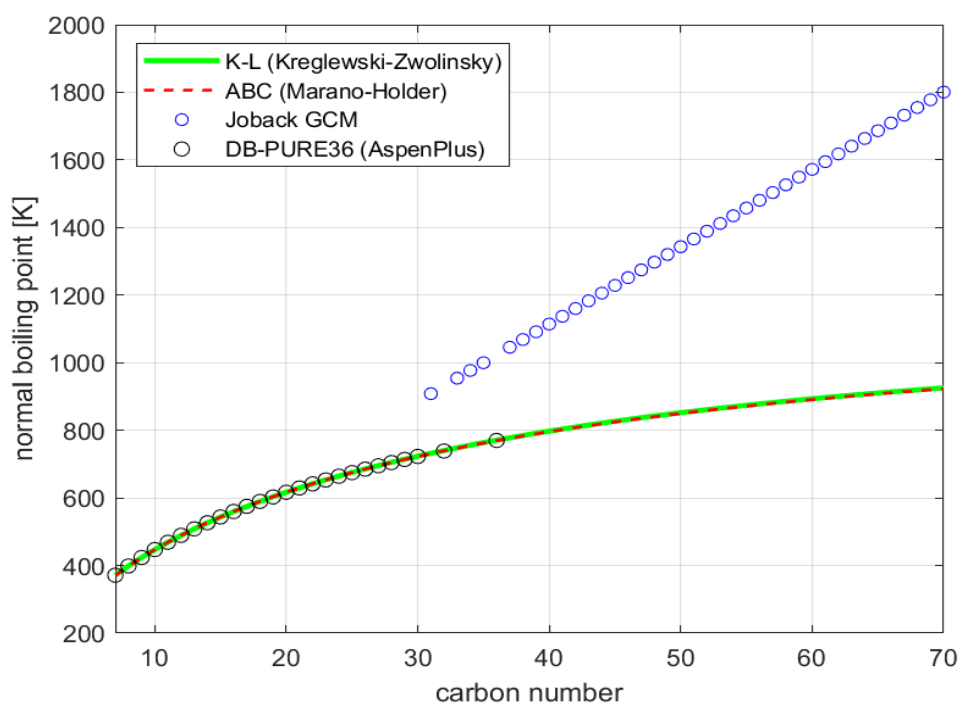


Figure 5.3: normal boiling point for C7-C70 n-paraffins: comparison between values computed by nonlinear regression of experimental values [Kreglewski et al., 1961] (eq. 5.22), Marano and Holder semi-empirical correlation [Marano et al., 1997] and Joback group contribution method (eq. 5.10) (as default by PCES) [ASPEN Phys.Prop.Data, v.10.1-0]. The values retrieved by ASPENPLUS (PURE36) pure database are black marked.

5.4.1.2 Critical temperature

It's well-known that thermal instability seriously affects measurements near the critical point for n-alkanes from C₁₈ on. However, the critical temperature model reported by Joback and Reid is the less accurate among the three (Fig. 5.4), due to the binomial equation used for the purpose (eq. 5.11). Indeed, it's a general rule using higher order polynomial in group contribution method only when a maximum or minimum appear: clearly, critical temperature shows no maximum or minimum as a function of molecular weight (carbon number).

Fortunately, there exist several correlative expressions to estimate T_c of heavier hydrocarbons from experimental data of the lighter ones, although the critical temperatures estimated by these expressions achieved very different results between each other that may diverge with increasing carbon number. As Soave marked [Soave, 1998], a

lot of these empirical expressions for the critical temperature were similar to those for normal boiling point. Actually, as discussed before for the Flory' s theory derived model for T_B estimation, also T_C could be correlated to the chain length by means of the carbon number of the molecule by a ' hole theory' . Soave proposed to equalize the two expressions for deriving a functional relation between critical temperature and normal boiling temperature [Soave, 1998], and added the assumption that for $n \rightarrow \infty$ the ratio T_C/T_B had to reach the unity (imposing equalization of the constants in the two logarithms). Thus he obtained the generic formula following:

$$\ln(c1 - T_c [K]) = c2 \ln(c1 - T_B [K]) - c3 \quad (5.23)$$

Correlating the same experimental data used by Teja, Tsonopoulos and Ambrose for n-alkanes from C_7 to C_{18} [Ambrose et al., 1995], Soave obtained the equation below:

$$\ln(1127.171 - T_c [K]) = 2.3724157 \ln(1671.5921 - T_B [K]) - 10.635057 \quad (5.24)$$

This equation was proved to give absolute error lower or almost equal to the experimental uncertainty in measuring critical temperature for higher alkanes (± 3 [K] up to C_{18} and ± 8 [K] from C_{19} to C_{24}) and, mainly, the difference between calculated and experimental value does not diverge with increasing carbon number [Soave, 1998].

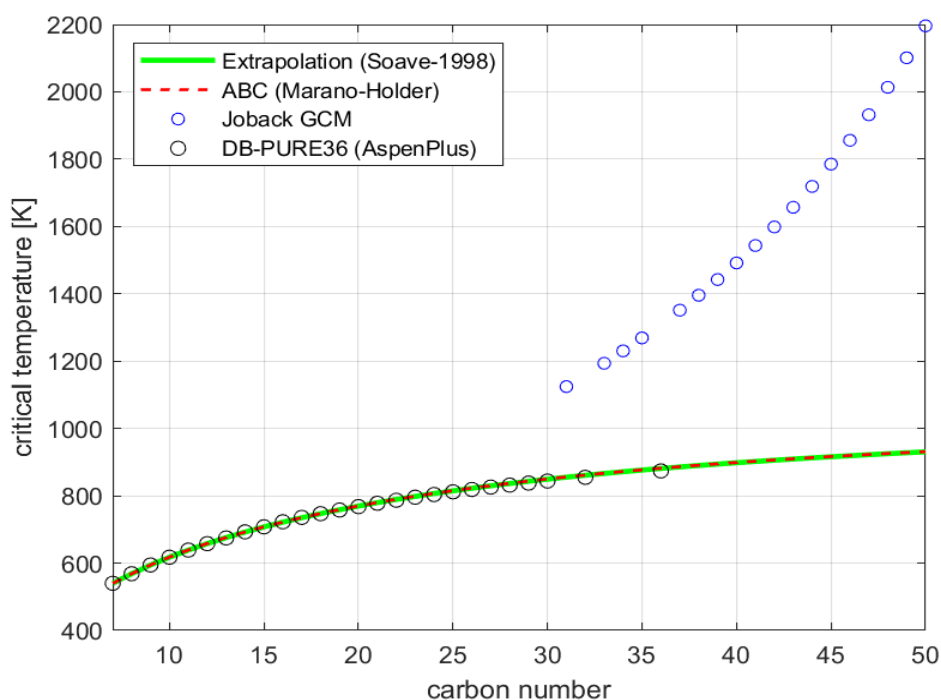


Figure 5.4: critical temperature for C7-C70 n-paraffins: comparison between values extrapolated by [Soave, 1998] (eq. 5.24), estimated values by ABC correlation (eq. 5.29) [Marano & Holder, 1997] and predictive by Joback group contribution method (eq. 5.12) (by default by PCES) [ASPEN Phys.Prop.Data, v.10.1-0]. The values retrieved by ASPEN Plus pure component databank (DB-PURE36) are reported and marked in black.

5.4.1.3 Critical pressure and acentric factor

The critical pressure and the acentric factor has been estimated by means of the iterative procedure described by Soave [Soave, 1998] for predicting pure vapor pressure of the higher weight (C₇-C₇₀) alkanes from SRK (Soave-Redlich-Kwong) cubic EoS. The reason for this choice lies in the evidence that using any cubic EoS (SRK, PR) for VLE calculations at a value of temperature outside the range of validity of the alpha function dependence could bring to unreasonable results [Soave, 1998].

The relation between attractive parameter and temperature just like expressed by (eq. 5.5) holds only from the normal boiling point to the critical point. But typical processes involving heavy organic streams are operated at temperatures surely below the normal boiling point of the heavier alkanes.

Soave [Soave, 1998] analyzed the trend of pure vapor pressure for n-dodecane at different temperatures as well as computed by SRK EoS and showed that even though experimental (or well-estimated) values for critical (T_C and P_C) properties and acentric factor were provided into the SRK EoS, the results were affected by serious errors at temperatures near and below the normal boiling point, increasing with lowering temperature.

Therefore, he tried to adjust the value of acentric factor so as SRK EoS to accurately reproduce the normal boiling point in order to extend the accuracy of the vapor pressure prediction to near the normal boiling point. However, this led to worsening of the vapor pressures results into the low-temperature region (below T_B) [Soave, 1998].

Therefore, in order to improve the results for lower saturation temperatures and maintain the refinement at T_B , Soave derived both critical pressure and acentric factor simultaneously by applying SRK equation iteratively until the saturation temperature at 10 mmHg and 760 mmHg (T_B) were correctly reproduced. The procedure brings to a marked improvement not only in the low temperature region but for temperatures widely above the normal boiling temperature also.

Of course, suppressing the condition at the critical temperature has worsened the prediction of vapor pressure for temperatures close to the critical point, but so much high temperatures are anyway outside the normal operating range for heavy hydrocarbons [Soave, 1998]. The iterative procedure consists of several steps:

The value of *critical pressure* (P_C) computed iteratively has been then correlated to the normal boiling point of the hydrocarbons with normal boiling point between 359.13 and 988.05 [K] (from C_7 to C_{100}) by Soave and coworkers, through equation (eq. 5.25)[Pellegrini et al., 2009]:

$$\ln(P_C(\text{bar})) = -15.488321 + 3.2328187 \left(\frac{100}{T_B[\text{K}]}\right)^3 + 2.7447020 \ln(1288.8545 - T_B[\text{K}]) \quad (5.25)$$

Also the *acentric factor* (ω) derived iteratively can be correlated to the normal boiling point of n-alkanes from C_7 to C_{100} . Soave proposed two different correlations for less weight n-alkanes and higher weight alkanes, due to high errors in the saturation temperatures at 10 mmHg reached by means of a single correlation for the acentric factor all over the range of n-alkanes considered (C_7 - C_{100}); mainly the error results unacceptable for lower weight alkanes, therefore two equations separately were used [Pellegrini et al., 2009]:

$$\ln(1187.9291 - \omega) = 8.9643355 * 10^{-4} \ln(1004.8417 - T_B[K]) + 7.0738919 \quad (359.13 < T_B[K] < 723.59) \quad (5.26)$$

$$\ln(1185.0931 - \omega) = 1.0478687 * 10^{-3} \ln(1047.5707 - T_B[K]) + 7.0704986 \quad (723.59 < T_B[K] < 988.05) \quad (5.27)$$

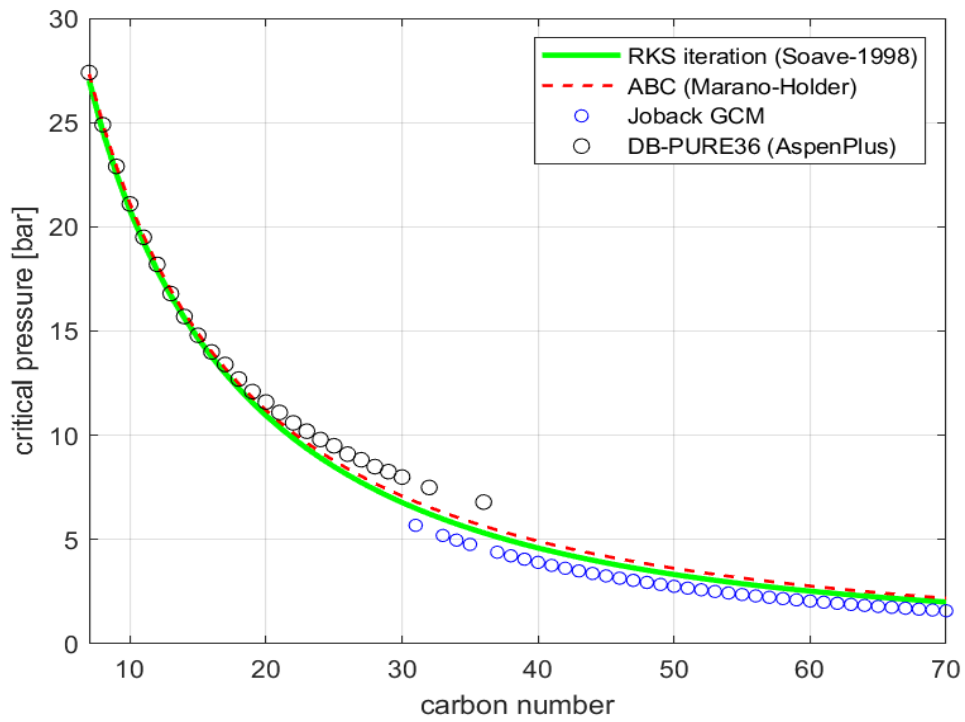


Figure 5.5: critical pressure for C7-C70 n-paraffins: comparison between values computed iteratively by RKS EoS to interpolate experimental vapour pressure at 10 and 760 mmHg [Soave, 1998] and estimated values by ABC semi-empirical equation (eq. 5.30) [Marano et al., 1997] and Joback group contribution method (eq. 5.12) (as default by PCES). The critical pressure values retrieved from Aspen Plus pure databank (DB-PURE36) are black marked.

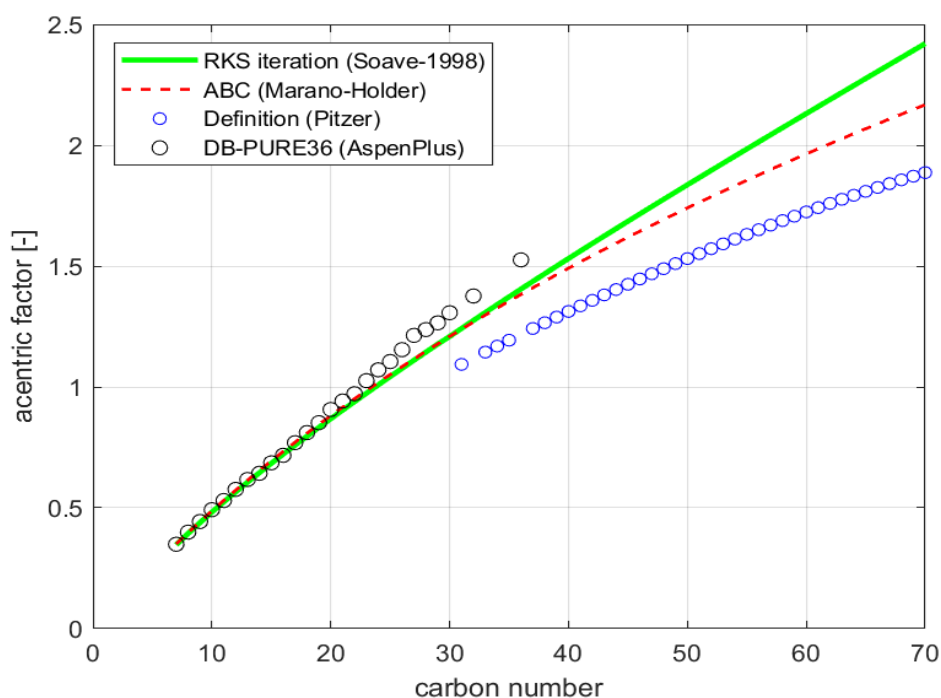


Figure 5.6: acentric factor for C7-C70 n-paraffins: comparison between values computed iteratively by imposing RKS EoS to interpolate experimental vapor pressure at 10 and 760 mmHg [Soave, 1998] and estimated values by ABC semi-empirical equation (eq. 5.32) [Marano et al., 1997] and Joback group contribution method (eq. 5.13) (as default by PCES) [ASPEN Phys.Prop.Data, v.10.1-0]. The acentric factors retrieved from ASPEN Plus pure databank (DB-PURE36) are black marked.

5.4.2 Methyl-alkanes

5.4.2.1 Critical parameters and acentric factor

A comprehensive set of equations for deriving derive critical properties for branched alkanes (methyl-alkanes) becomes more difficult compared to n-alkanes due to the unavailability of experimental values for normal boiling point and the huge number of possible isomers that diverges with carbon number; for these reasons, the branched alkanes of a certain carbon number has been lumped, i.e. only one branched alkane molecule represent the entire set of possible isomers at each carbon number.

Gamba et al. [Pellegrini et al., 2009] showed as the same correlations for the alkanes may be applied to methyl-alkanes (lumped), once having derived a suitable value for the

normal boiling point for each lump. According to experimental values of normal boiling point for mono and di-methyl branched alkanes up to C₁₀, Gamba et al. noted that ratio between the mean normal boiling temperature for methyl-alkanes and the same quantity for the n-alkane with the same molecular weight was practically constant and equal more or less to 0.973.

Thus, also in this work the normal boiling temperature of each methyl branched alkane has been computed from that of the corresponding n-alkane [Pellegrini et al., 2009]:

$$T_{B,iso-alkane} = 0.973 T_{B,alkane} [K] \quad (5.28)$$

Comparing the experimental value for critical temperature of isomers (mono and di-methyl alkanes) and alkanes up to C₁₀, Soave et al. [Pellegrini et al., 2009] argued that mean critical temperature for isomers with a certain carbon number resulted to be always lower than the critical temperature of the n-alkane with equal n_c and, mainly, all the branched paraffins with a given normal boiling point showed about the same value for critical temperature.

Therefore, a correlation between critical temperature and normal boiling point as that for n-alkanes could give reasonable results for isomers (lumped) also. In particular, Soave et al. yield very reliable results for mono-methyl isomers (maximum error of -3.4 [K] for 3-methylhexane) [Pellegrini et al., 2009]. Therefore the same correlation (eq. 5.24) between critical temperature and normal boiling point used for n-alkanes from C₇ to C₇₀ has been applied also to lumped isomers with the same n_c.

Also critical pressure and acentric factor were computed iteratively by imposing the SRK EoS to pass through the experimental value of boiling temperature at 10 and 760 mmHg. This choice was supported by the evidence that the vapor pressure data (at 10 mmHg) of branched n-paraffins were the same as those of the n-alkane with similar normal boiling point [Pellegrini et al., 2009].

Moreover the correlative expression between critical pressure (eq. 5.25) (or acentric factor) and normal boiling point for n-alkanes was employed for methyl-alkanes also, following the same consideration about the use of two different expressions for correlating the acentric factor over all the range of normal boiling temperatures (eq. 5.26-5.27) (C₇-C₇₀ lumped methyl-alkanes).

5.4.3 Olefins

5.4.3.1 Critical parameters and acentric factor

The rates of olefin formation decrease considerably with carbon number so that the amount of olefin products is very low if compared to that of saturated hydrocarbons in a Co-based FT process plant because of intrinsic kinetics and/or secondary chemical (secondary reactions) and physical (accumulation) reasons, as discussed in (Cap. 3.2). Rather light olefins are produced in the simulative process and in particular α -olefins up to α -tetracontene (C_{40}) are involved in the current Aspen Plus simulation work.

Generally, the economic value and the intended market (as valuable chemicals) for these products are really different with respect to paraffin (transportation fuels) due to their marked reactivity and capability of polymerization at high temperatures. Moreover, latter features make measurement of critical properties even more difficult than in the case of paraffins and generally experimental values for normal boiling point are available only up to C_8 for 1-olefins [Marano et al., 1997]. Therefore, a theoretical approach is usually involved to derive correlations for estimating critical parameters of high molecular weight olefins. In particular, statistical thermodynamics, once applied to the polymer theory, had provided two fundamental approaches for deriving saturation and critical properties of high molecular weight polymers: the lattice-fluid model (Kurata and Isida, Lacombe and Sanchez) [Kurata et al., 1955; Sanchez et al., 1976] and the Flory cell theory (Flory, Orwoll and Vrij) [Flory et al., 1964].

The former considers the polymer-solvent mixture to have a quasi-crystalline structure wherein each lattice site is occupied by either chain segments (mers, as they are often referred to, such as $-CH_2-$ segments in linear hydrocarbons) or empty holes and the mer can move almost freely through the holes (intermolecular interactions between mers are not considered).

In the Flory cell theory, instead, each mer can move only within a limited volume of space (the 'cell') due to the close presence of neighboring mers (bonded or non-bonded) and the holes are not directly introduced into the model [Marano et al., 1997].

Anyway, the objective for both models was to develop a PVT-relation (EoS) in order to write all the thermodynamic functions (internal energy, entropy, enthalpy, free energy) with respect to the chain size (s), which represents the number of mers within a polymer molecule.

It's clear how the chain size is strictly related to the number of carbon atoms into a molecule. From the lattice-fluid theory [Marano et al., 1997] it can be shown as all these functions are asymptotically ($s \rightarrow \infty$) linear in s and applying the critical constraints ($dP/dV = 0$ and $d^2P/dV^2 = 0$ at critical point) it is possible to appreciate the asymptotic behavior of critical temperature, pressure and volume too.

Mariano and Holder developed a generalized asymptotic behavior correlation (ABC) applicable to homogeneous series of compounds (n-paraffins, n-olefins exc.) [Mariano et al., 1997] starting from the results of 'lattice' and 'cell' theory. The ABC correlations for critical properties and acentric factor take the form underneath:

$$T_c = Y_\infty - \Delta Y_0 \exp(-\beta(n - n_0)^\gamma) \quad (5.29)$$

$$P_c = Y_\infty - \Delta Y_0 \exp(-\beta(n - n_0)^\gamma) \quad (5.30)$$

$$V_c^{2/3} = \Delta Y_\infty(n - n_0) - \Delta Y_0 \exp(-\beta(n - n_0)^\gamma) \quad (5.31)$$

$$\omega = \Delta Y_0 + \beta(n - n_0)^\gamma \quad (5.32)$$

Where Y_∞ is the value of the asymptote for critical temperature and pressure (type I properties), whereas it arises a more than linear dependency on carbon number for critical volume (type II properties); indeed, on the basis of the lattice-fluid theory, critical volume is proportional to $n^{3/2}$, thus $V_c^{2/3}$ should be proportional to carbon number to obtaining the ABC correlation stated above (eq. 5.31) [Marano et al., 1997].

As can be seen from values in Table (5.2), critical temperature and normal boiling point ABCs across at a carbon number of 110.5; therefore, the critical pressure at the carbon number of intersection was constrained to atmospheric pressure to maintain consistency between the different correlations.

Table 5.2: ABC Parameters for normal boiling point, critical temperature, pressure, volume and acentric factor for n-olefins

n_0	1.340265	0.980154	-3.039461	-53.081049	-23.174122
ΔY_0	1256.04	892.82	-1336.74	218.71	-6.5597
Y_∞	1091.11	1020.71	0		
ΔY_∞				2.37919	
β	0.153505	0.198100	2.111827	0.000114026	3.383261
γ	0.602490	0.629752	0.258439	2.19258	0.208770

5.4.4 Mathias-Copenam alpha function (parameters)

Especially into the Fischer-Tropsch reactor and downstream separation, the range of operating temperatures allow the vapor pressure of long chain hydrocarbon to be small and difficult to compute.

At this regard, Soave et al. [Soave et al., 2010] have compared the values of saturation temperature for alkanes from C₂₁ to C₁₀₀ at 5, 2, 1 and 0.5 mmHg from literature (Zwolinsky and Wilhoit) [Zwolinski et al., 1971] with those computed by means of SRK with critical parameters (P_C and ω) derived iteratively before [Soave, 1998].

The results appeared to be acceptable down to 5 mmHg, while at lower pressures the error increased rapidly to high percentage value. The error was proved to diverge with lowering temperature or to worse at middle vapor pressure range (10-700 mmHg) also when SRK EoS with Soave alpha function was forced to pass through normal boiling point (760 mmHg) and whatever saturation point lower than 5 mmHg.

The unacceptable behavior of vapor pressure at so-low temperature inspired Soave and coworkers to force SRK EoS with critical parameters and acentric factor computed before to pass through three points (0.5, 10 and 760 mmHg), employing the Mathias-Copenam alpha function for modeling the attractive term, instead of the classic Soave alpha function [Pellegrini et al., 2009].

$$\alpha(T_r) = \left(1 + m_1(1 - \sqrt{T_r}) + m_2(1 - \sqrt{T_r})^2 + m_3(1 - \sqrt{T_r})^3\right)^2 \quad (5.33)$$

Since the value of the ratio $\alpha(T_r)/T_r$ (into the a-dimensional A/B ratio seen before) and thus of the alpha function $\alpha(T_r)$ at 0.5, 10 and 760 mmHg could be derived directly from P_r/T_r (into the a-dimensional B term), the three parameters of Mathias-Copeman alpha function can be computed by solving a system of three equations for each $\alpha(T_r)$ (at 0.5, 10 and 760 mmHg) in three unknowns (m_1, m_2, m_3) for each hydrocarbon. Successively these parameters can be correlated to the normal boiling point of the paraffins and (lumped) methyl-alkanes by means of the equation here below [Pellegrini et al., 2009]:

$$m_{i,j} = c_{1,i}(T_{B,j}[K])^6 + c_{2,i}(T_{B,j}[K])^5 + c_{3,i}(T_{B,j}[K])^4 + c_{4,i}(T_{B,j}[K])^3 + c_{5,i}(T_{B,j}[K])^2 + c_{6,i}(T_{B,j}[K]) + c_{7,i} \quad (5.34)$$

Where $i = 1, 3$ indicates the m coefficient and j stands for the hydrocarbon involved.

Table 5.3: parameters to be used in eq. (5.26) to derive Mathias-Copenam α function m-coefficients for n-alkanes with TB < 925.7 [K] (Gamba et al., 2009)

$C_{1,i}$	0	1.941450005839E-14	-7.220152534737E-14
$C_{2,i}$	0	-8.730499182421E-1	3.255208275938E-10
		1	
$C_{3,i}$	0	1.632815151766E-07	-6.102063230887E-07
$C_{4,i}$	0	-1.625605200540E-0	6.087515227689E-04
		4	
$C_{5,i}$	5.969887338262E-06	9.086006185896E-02	-3.408512463993E-01
$C_{6,i}$	-4.342676461393E-03	-2.703122831103E+0	1.015601714000E+02
		1	
$C_{7,i}$	2.193285810607	3.3430956878E+03	-1.257861132321E+04

The Mathias-Copenam alpha function clearly helped to improve liquid vapor pressure prediction of long chain alkanes and methyl-alkanes at temperatures well below that of saturation at 5 mmHg, considering that these temperatures are usually reached during the process.

(Fig. 5.7) shows liquid vapor pressure of four heavy paraffins at temperature typically involved in hydrocracking reactors (300-360 °C) as predicted by RKS-BM EoS, i.e. eq. (5.8) with Mathias-Copenam parameters (eq. 5.34) in the alpha function (eq. 5.33).

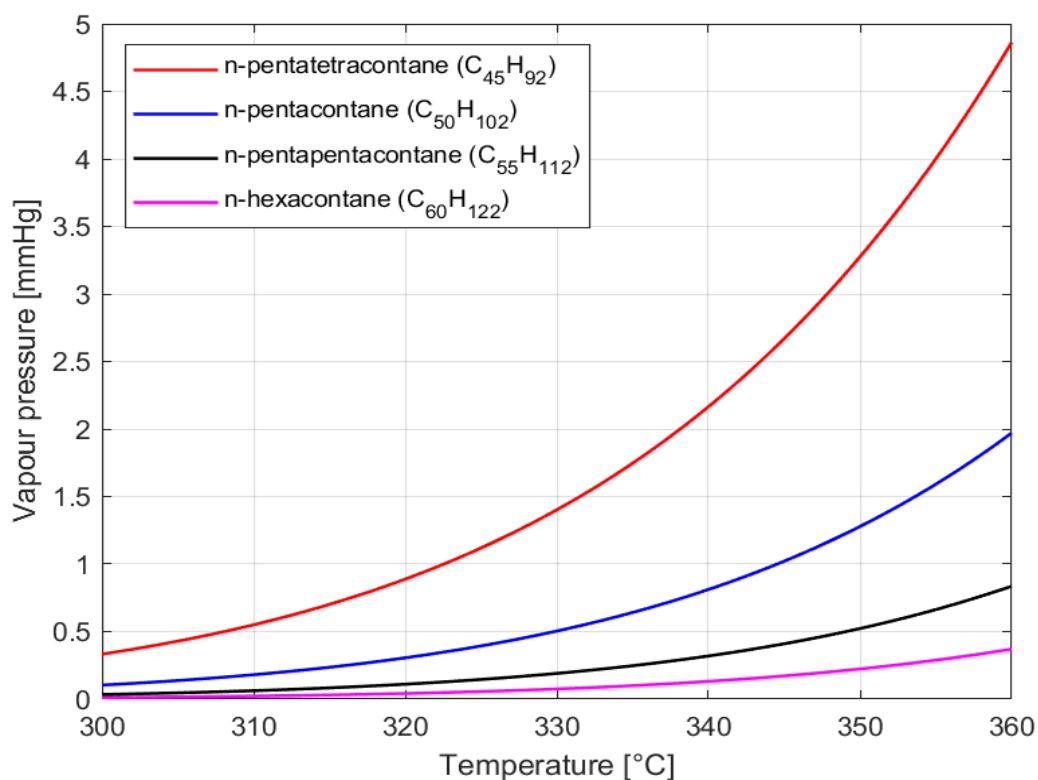


Figure 5.7: pure component liquid vapor pressure computed by RKS-BM EoS for some heavy alkanes at temperatures typically used for mild hydrocracking of FT waxes

5.4.5 Binary parameters (classical mixing rule)

Usually, Aspen Property System sets to zero the binary interaction parameter that account for the symmetrical attraction term in the classical parameter mixing rule for RKS-BM, which reflects the contribute of London dispersion or Van der Waals force field onto the behavior of nonpolar compound mixtures. Therefore, a correct estimation of $k_{i,j}$ is fundamental for SRK equation to predict the behavior of nonpolar gas and liquid compound containing systems (such as hydrogen and heavy liquid paraffin in the hydrocracking module or CO₂-paraffin mixtures in FT reactor) at equilibrium (VLE behavior). In particular, hydrocracking of FT paraffin waxes is hugely affected by the vapor-liquid equilibrium of mixture since isomerization/cracking reactions occur both into vapor and liquid phase and VLE calculation results, such as fugacity, are directly involved

into the product formation and reactant consumption rates. However, VLE calculations by means of SRK showed vapor phase was dominant at the range of operating conditions considered [Pellegrini et al., 2004, 2007a]. The interaction parameters that really affect the hydrocracking results are the hydrocarbon-H₂ ones that have been computed by means of the relation by [Tsonopoulos et al., 1986],[Pellegrini et al., 2008]:

$$k_{i,j} = d_1 + \frac{d_2 x_{H_2,j}^3}{1 + x_{H_2,j}^3} \quad (5.35)$$

Where $d_1 = 0.0067$, $d_2 = 0.63375$ and

$$\frac{x_{H_2,j}}{T_{C,j} - 50} = \frac{1000 - T_{C,j}}{1000 - T_{C,j}} \quad (5.35.1)$$

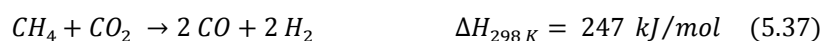
($T_{C,j}$ is the critical temperature of the j-component).

5.5 Kinetic models

The three sub-process models for the GTL process, i.e. the syngas production, the syngas conversion to liquid fuels (FTS) and the product upgrading (wax hydrocracking), are analyzed with ASPEN Plus within appropriate reactor models.

The first step is to generate the mixture of H₂ and CO at suitable composition for the next synthesis step (H₂/CO ratio of about 2.1). The steam reforming of methane is dominant among all the process technologies for the production of hydrogen and is currently applied in various GTL plants worldwide. However, steam reforming alone could provide syngas with too high H₂/CO ratio (about or greater than 4), due to high quantities of hydrogen in the feed and also to the increase of the rate of water-gas-shift reaction, favored by the presence of steam. A steam reforming process with simultaneous utilization of CO₂ could enhance the syngas quality (decreasing the H₂/CO ratio) and allow for the utilization of the more infamous green-house-gases, CO₂ and CH₄.

The simultaneous CO₂ (CDR) and steam (SMR) reforming process of methane are simulated and analyzed using ASPEN Plus on the Gibbs reactor model. In the simultaneous CO₂ and steam reforming process, CO₂ and H₂O are converted simultaneously by reacting with methane, as follows:



Generally, to maximize methane and CO₂ conversion, reforming reactors are operated at high temperatures (about 800-1000 °C) and reactions are catalyzed over different noble metals and nickel and/or cobalt based catalysts. Under these conditions, it can be assumed that the two reactions above reach chemical equilibrium, since the reactions are very fast at higher temperatures. Last consideration justifies the use of a phase/chemical equilibrium reactor model, such as the selected RGibbs reactor model.

Recently, [Choudary & Mondal,2006] have investigated the performance of reduced NdCoO₃ perovskite-type mixed metal oxide catalyst (Co dispersed on Nd₂O₃) at different process conditions for CO₂ reforming with simultaneous steam reforming of methane to syngas. Several experiments of last researchers reveal that this catalyst is more active for the CO₂ reforming as compared to that for the steam reforming and, notably, no carbon deposition was observed on the catalyst during either of the reactions. This is surprising

since carbon deposition is a major issue for all reforming catalysts and it is enhanced by increasing the amount of carbon in the feed. Therefore, carbon deposition should occur even more rapidly onto CO₂ reforming catalysts.

Anyway, in order to reduce the carbon formation, the use of steam, oxygen or both has been largely suggested because of their ability to oxidize the carbon precursor species (such as partially hydrogenated CH_x species). Moreover, in the presence of steam, methane steam reforming (SMR) occurs simultaneously and thereby 100 % selectivity for both H₂ and CO can be achieved and the H₂/CO ratio can be controlled and adjusted to the desired value in a flexible way.

PFR (plug flow reactor) ASPEN Plus model has been used for both the Fischer-Tropsch and hydrocracking reactor.

The detailed kinetic models for an industrial alumina-supported Re promoted Co catalyst for FTS [Todic et al., 2013] and for an industrial alumina-supported Pt catalyst for hydrocracking [Pellegrini et al., 2008] were programmed in FORTRAN language and compiled as defined-user kinetics for ASPEN Plus (Appendix A.4-A.5). These user kinetic models were applied in the PFR ASPEN Plus model according to the procedure described in (Appendix A.1-A.2-A.3)

Though there is no accordancy on the actual mechanism occurring over FT or hydrocracking catalyst surface, the scientific community agrees that both FTS and hydrocracking are rate controlled and heterogeneously catalyzed reactions, in which adsorption takes a fundamental role. Hence, in principle, they can be described by means of a combination of kinetic and equilibrium constants between adsorbed and desorbed species [Selvatico et al., 2016]

Following a well-established approach for reactor and process design, the simplified scheme and the reaction assumptions turns to be the basis for deriving the reaction rates by fitting experimental (i.e. power of law) or semi-empirical (i.e. LHHW) equations to experimental data (according to the inductive approach mentioned before). In this way it is possible to model the reaction dependence on reactant partial pressures and on temperature (through rate constant dependency on the Arrhenius law).

It is clear that the assumptions on any elementary reaction are fundamental for a correct prediction of the reaction rates (that immediately correlate each product with the partial pressures of the reactants directly involving the surface concentration (coverage) of the intermediate adsorbed species).

One of the most largely employed reaction scheme for modelling chemisorption process on solid surface catalysts is the Langmuir-Hinselwood-Hougen-Watson (LHHW) model. It provides a simplified model according to which the surface of the catalyst is depicted as a continuum array of equivalent sites assumed to interact only through chemisorption of reactant species. Langmuir adsorption isotherms are the theoretical basis for the LHHW approach development since they are able to correlate surface coverages with partial pressures of reactant species in fluid phase.

According to the LHHW approach, the reaction rates for any product can be expressed as:

$$r = \frac{(KINETIC FACTOR) (DRIVING FORCE)}{(ADSORPTION)} \quad (5.38)$$

where:

$$(KINETIC FACTOR) = k e^{-\frac{E_a}{RT}} \quad (5.39)$$

$$(DRIVING FORCE) = \frac{K_1 (\prod C_i^{v_i})}{K_2 (\prod C_i^{v_i})} \quad (5.40)$$

$$(ADSORPTION) = \left[\sum K_i (\prod C_i^{v_i}) \right]^m \quad (5.41)$$

In which:

- k : pre-exponential factor $\left(\frac{kmol}{kg_{cat}h}\right)$ or $\left(\frac{kmol}{m^3 h}\right)$;
- E_a : activation energy $\left(\frac{kJ}{mol}\right)$;
- K_1, K_2 : equilibrium constants for forward and backward reaction, respectively $\left(\frac{1}{[C_i]}\right)$;
- K_i : Langmuir adsorption isotherm constant for adsorbed (intermediate) species i ;
- C_i : concentration of the chemical species i (Pa), $\left(\frac{kg}{m^3}\right)$, $\left(\frac{kgmol}{m^3}\right)$, (y_i) , (x_i) ;
- v_i : concentration exponent;
- m : adsorption term exponent.

The rate of product formation increases when catalyst reactivity is increased as it is expressed by the kinetic factor (eq. 5.39); also the driving force expression (eq. 5.40) shows as the reaction rate is increased with increasing concentration of reactants at the equilibrium, as well as with higher intrinsic kinetic constant at equilibrium; on the other

hand, reaction rate decreases with increasing surface coverage of the intermediate species due to lower availability of catalyst surface sites for reactant species; this aspect is accounted in the adsorption expression (eq. 5.41).

5.5.1 FT synthesis

One of the first detail mechanisms to reproduce the FT synthesis sequence of elementary reactions has been the carbide mechanism. This mechanism has gain particular relevance for FTS iron-based catalysts, but originally was developed also for LTFT application with cobalt-based catalysts. The carbide mechanism differs from the other mechanism proposed over the years mainly for the monomer formation pathway and successive insertion into the growing chain, which occurs only after dissociation of carbon and oxygen atoms embedded into adsorbed carbon monoxide.

Adopting the approach implemented in [Todic, et al., 2013] as a reference, the kinetics of FTS is modelled via the carbide mechanism proposed by [Lox & Froment, 1993]. The scheme of elementary reactions is displayed below:

Table 5.3: FTS reaction pathway

Step	Type	Elementary reaction	Kinetic / equilibrium constant
1	RDS	$CO + H - S \rightarrow H - S - CO$ $CO + CH_3 - S \rightarrow CH_3 - S - CO$ $CO + C_n H_{2n+1} - S \rightarrow C_n H_{2n+1} - S - CO$	k_1
2	EQS	$H - S - CO + H_2 \rightarrow H - S - C + H_2O$ $CH_3 - S - CO + H_2 \rightarrow CH_3 - S - C + H_2O$ $C_n H_{2n+1} - S - CO + H_2 \rightarrow C_n H_{2n+1} - S - C + H_2O$	K_2

3	EQS	$\begin{aligned} H-S-C + H_2 &\rightarrow H-S-CH_2 \\ CH_3-S-C + H_2 &\rightarrow CH_3-S-CH_2 \\ C_nH_{2n+1}-S-C + H_2 &\rightarrow C_nH_{2n+1}-S-CH_2 \end{aligned}$	K_3
4	EQS	$C_nH_{2n+1}-S-CH_2 \rightarrow C_nH_{2n+1}-CH_2-S$	K_4
5	RDS	$\begin{aligned} CH_3-S + H_2 &\rightarrow CH_4 + H-S \\ C_nH_{2n+1}-S + H_2 &\rightarrow C_nH_{2n+2} + H-S \end{aligned}$	k_{5M} k_5
6	RDS	$\begin{aligned} C_2H_5-S &\rightarrow C_2H_4 + H-S \\ C_nH_{2n+1}-S &\rightarrow C_nH_{2n} + H-S \end{aligned}$	k_{6E} $k_{6,n}$
7	EQS	$H_2 + 2S \leftrightarrow 2H-S$	K_7

Source: (Todic, et al., 2013)

This reaction pathway has been coupled with the chain-length-desorption concept, first proposed by [Botes, 2007], to derive the kinetic model. The key assumption of this concept is the exponential dependence of the 1-olefin formation rate on the chain length of the molecule desorbed. In a study conducted by [Todic, et al., 2014] the researchers has showed that the linear dependency of the heat of chemisorption of 1-olefins with carbon number results into a linear dependency of desorption activation energy:

$$E_{d,1-olefins}^n = E_{d,1-olefins}^0 + \Delta E \cdot n \quad (5.42)$$

This dependency is caused by the weak Van der Waals' s (VdW) interactions of the 1-olefin precursors, a π complex, with the catalyst surface. Indeed the formation of 1-olefins consists of two steps: β -hydrogen elimination from the growing chain (alkyl chain or σ -complex, $C_nH_{2n+1}-S$) forming the π -complex and desorption of a π -complex, which is the rate limiting among the two steps. [Cheng, et al., 2008] incorporated the two steps into one-step desorption process. As the chain length increases, the weak VdW forces causes

an increase in the activation energy of the one-step desorption of 1-olefins, which is followed by a decreased probability in 1-olefin formation. Therefore, being σ -complex and π -complex in equilibrium, what it could seem to see is an increase in residence time of the alkyl chain (σ -complex) that results in a higher probability for chain growth and hydrogenation to n-paraffins with increasing chain length [Todic, et al., 2013]. Using DFT (density theory function) and statistical thermodynamics calculation the increasing character of chemisorption energy of 1-olefins with increasing chain length involving VdW forces was validated by the works of [Nguyen, et al., 2011].

All the possible secondary reactions involving 1-olefins, once they have desorbed, such as re-adsorption, hydrogenation and isomerization, have not been considered in the present model.

The linearity of the activation energy of the one-step desorption of 1-olefins lead to an exponential dependency of rate constant for 1-olefin desorption on chain length:

$$k_{d,1-olefins}^n = k_{d,1-olefins}^0 \cdot e^{c \cdot n} \quad (5.43)$$

Where the constant $c = -\frac{\Delta E}{RT}$ represents the contribution to desorption rate constant of the weak VdW interactions of the chain with the surface for each C-atom (or CH₂ group). Before deriving the formation rate equations for each FT product some assumptions are needed and clearly introduced into the mathematical derivation [Todic, et al., 2013]:

- Only one type of FTS active site is present on Co catalyst surface;
- The total number of active sites on the catalyst surface is constant (no deactivation);
- The concentration of surface intermediates (occupied sites) and vacant sites are at steady-state;
- Methane and ethylene have different formation rate constants than other n-paraffins and 1-olefins, respectively;
- Rate constants of chain propagation and termination to n-paraffin are independent on chain length;
- The rate constant of chain desorption to 1-olefin is exponentially dependent on carbon number (desorption concept);
- Elementary steps for the formation of n-paraffins (step 5) and 1-olefins (step 6) and the first step of monomer formation (CO adsorption) and chain propagation (step 1) are rate-determining-steps (RDS). All other steps are considered quasi-equilibrated.

Rates of formation of n-paraffin and 1-olefin with n carbon atoms can be written as:

$$R_{C_nH_{2n+2}} = k_5 [C_nH_{2n+1} - S] P_{H_2} \quad (5.44)$$

$$R_{C_nH_{2n}} = k_6^n [C_nH_{2n+1} - S] \quad (5.45)$$

$[C_nH_{2n+1}]$ represents the surface coverage of the adsorbed (intermediate) species $C_nH_{2n+1} - S$ and P_{H_2} is the hydrogen partial pressure. k_5 is the kinetic rate constant for desorption to n-paraffin, whereas k_6^n is the kinetic rate constant for desorption to 1-olefin, equal to $k_6^0 e^{c \cdot n}$.

As just defined for hypothesis, the formation rate for methane and ethylene have different kinetic rate constant:

$$R_{CH_4} = k_{5M} [CH_3 - S] P_{H_2} \quad (5.46)$$

$$R_{C_2H_4} = k_{6E,0} e^{c \cdot 2} [C_2H_5 - S] \quad (5.47)$$

Where k_{5M} is the kinetic rate constant for desorption to methane, whereas k_{6E}^n is the kinetic rate constant for desorption to ethylene, equal to $k_{6E}^0 e^{2 \times n}$.

The introduction of growth probability factor allows relating the surface fractions of various chain intermediates $[C_nH_{2n+1} - S]$ to intrinsic kinetic constants, partial pressure of reactants (P_{CO} and P_{H_2}) and fraction of vacant sites $[S]$. The chain growth probability for surface intermediate having n carbon atoms in the chain could be expressed as:

$$n \geq 3 \quad \alpha_n = \frac{[C_nH_{2n+1} - S]}{[C_{n-1}H_{2n-1} - S]} \quad (5.48)$$

$$n = 1 \quad \alpha_1 = \frac{[CH_3 - S]}{[H - S]} \quad (5.49)$$

$$n = 2 \quad \alpha_2 = \frac{[C_2H_5 - S]}{[CH_3 - S]} \quad (5.50)$$

According to the third assumption listed above [Todic, et al., 2013], the PSSH (pseudo-steady-state-hypotesis) is applied for the intermediate surface fraction $[C_nH_{2n+1} - S]$, which implies that catalyst deactivation is not considered in the present model:

$$n \geq 3 \quad -\frac{dC_n}{dt} = -k_1 P_{CO} C_{n-1} + k_1 P_{CO} C_n + k_5 P_{H_2} C_n + k_6 e^{c \times n} C_n = 0 \quad (5.51)$$

where C_n is the surface coverage of the adsorbed intermediates with n carbon atoms: $[C_n H_{2n+1} - S]$, whereas C_{n-1} is the surface fraction of the adsorbed intermediate with n-1 carbon atoms $[C_{n-1} H_{2n-1} - S]$.

Hence, the surface fraction of generic intermediate with n carbon atoms has been related to that of the previous intermediate (with n-1 carbon atoms), allowing to express the chain growth probability in terms of reactant partial pressure and intrinsic kinetic constant of adsorption, propagation and termination:

$$n \geq 3 \quad \alpha_n = \frac{k_1 P_{CO}}{k_1 P_{CO} + k_5 P_{H_2} + k_6 e^{c \cdot n}} \quad (5.52)$$

Where it can be noted the exponential trend of chain growth probability with chain length (through n at the exponent at denominator).

The chain growth probability for methane and ethylene involve different kinetic constant for termination and they has been defined separately:

$$\alpha_1 = \frac{k_1 P_{CO}}{k_1 P_{CO} + k_{5M} P_{H_2}} \quad (5.53)$$

$$\alpha_2 = \frac{k_1 P_{CO}}{k_1 P_{CO} + k_5 P_{H_2} + k_{6E} e^{c \cdot 2}} \quad (5.54)$$

After having defined the chain growth probability in terms of reactant conditions (partial pressures of H₂ and CO) and intrinsic kinetic constants (catalyst and temperature dependent) for each product, next step is to relate the surface fraction appearing in rate equations to these quantities. Indeed from definition of chain growth probability (eq. 5.52), it is possible to write:

$$\begin{aligned} [C_n H_{2n+1} - S] &= \alpha_n \cdot [C_{n-1} H_{2n-1} - S] = \alpha_n \cdot \alpha_{n-1} \cdot [C_{n-2} H_{2n-3} - S] = \dots \\ &= \alpha_1 \cdot \alpha_2 \cdot \prod_{i=3}^n \alpha_i \cdot [H - S] \end{aligned} \quad (5.55)$$

The fraction of adsorbed hydrogen can be related to the fraction of vacant sites $[S]$ and the equilibrium constant of the hydrogen adsorption reaction (step 7):

$$[H - S] = \sqrt{K_7 P_{H_2}} \cdot [S] \quad (5.56)$$

Introducing (1.5), the (1.4) expression can be rewritten as:

$$[C_nH_{2n+1} - S] = \alpha_1 \cdot \alpha_2 \cdot \prod_{i=3}^n \alpha_i \cdot \sqrt{K_7 P_{H_2}} \cdot [S] \quad (5.57)$$

In order to express the surface fraction of vacant sites in terms of computable quantities (partial pressures and kinetic constants) a balance of all sites is needed. According to the complete procedure exposed in [Todic, et al., 2013] and making use of the second hypothesis listed above (negligible deactivation), the surface fraction of vacant sites can be expressed as:

$$[S] = 1 / \left\{ 1 + \sqrt{K_7 P_{H_2}} + \sqrt{K_7 P_{H_2}} \cdot \left(1 + \frac{1}{K_4} + \frac{1}{K_3 K_4 P_{H_2}} + \frac{1}{K_3 K_4 P_{H_2}} \frac{P_{H_2 O}}{P_{H_2}^2} \right) \cdot (\alpha_1 + \alpha_1 \alpha_2 \dots + \alpha_1 \alpha_2 \sum_{i=3}^n \prod_{j=3}^i \alpha_j) \right\} \quad (5.58)$$

The equilibrium constants (K_2, K_3, K_4, K_7) of the different elementary reaction steps are evaluated according to:

$$K_i = A_i \cdot e^{-\Delta H_i / R T} \quad (5.59)$$

Where:

- A_i : pre-exponential factor of the i elementary step;
- ΔH_i : enthalpy of i elementary step and adsorption step;

Finally, the resulting reaction rate equations for methane, ethylene, n-paraffin, 1-olefin can be written in terms of computable quantities and expressed in kmoles of product over kilogram of catalyst:

$$R_{CH_4} = k_{5M} K_7^{0.5} P_{H_2}^{1.5} \alpha_1 \cdot [S] \quad (5.60)$$

$$R_{C_nH_{2n+2}} = k_5 K_7^{0.5} P_{H_2}^{1.5} \alpha_1 \alpha_2 \prod_{j=3}^n \alpha_j \cdot [S] \quad (5.61)$$

$$R_{C_2H_4} = k_{6,E} e^{2 \cdot c} \sqrt{K_7 P_{H_2}} \alpha_1 \alpha_2 \cdot [S] \quad (5.62)$$

$$R_{C_nH_{2n}} = k_6 e^{n \cdot c} \sqrt{K_7 P_{H_2}} \alpha_1 \alpha_2 \prod_{j=3}^n \alpha_j \cdot [S] \quad (5.63)$$

The intrinsic kinetic and equilibrium constants present in the model were evaluated by [Todic, et al., 2013] fitting experimental data obtained over a Re promoted cobalt-alumina catalyst. Various models were considered to be likely to represent the FT reaction sequence, but only one (that reported in the present work) was able to pass both the statistical test providing a good fit of the experimental data and the physicochemical test, meaning that the model parameters must satisfy the following physicochemical laws:

- Kinetic rate constants k_i have to follow the Arrhenius law, whereby activation energy:

$$E_{a,i} > 0 \quad (5.64)$$

- Since adsorption is an exothermic process, adsorption enthalpy has to satisfy:

$$-\Delta H_{a,i}^0 > 0 \quad (5.65)$$

- The adsorption entropy has to satisfy two conditions:

$$0 < -\Delta S_{a,i}^0 < S_{g,i}^0 \quad (5.66)$$

$$41.8 < -\Delta S_{a,i}^0 < 51.4 + 1.4 \cdot 10^{-3} \cdot \Delta H_{a,i}^0 \quad (5.67)$$

Where $S_{g,i}^0$ is the standard entropy of a gaseous species i , $\Delta S_{a,i}^0$ is the standard adsorption entropy and $\Delta H_{a,i}^0$ is the standard adsorption enthalpy.

Table 5.4: estimated parameters for the FT synthesis kinetic model used in the present work (a form of carbide mechanism).

Parameter	Value	Unit
A_1	$1.83 \cdot 10^{10}$	$mol/(kg_{cat} \cdot h \cdot MPa)$
E_1	100.4	kJ/mol

A_2	5.08	kJ/mol
ΔH_2	8.68	kJ/mol
A_3	24.4	MPa^{-1}
ΔH_3	9.44	kJ/mol
A_4	2.90	kJ/mol
ΔH_4	7.90	kJ/mol
A_5	$4.49 \cdot 10^5$	$\text{mol}/(\text{kg}_{\text{cat}} \cdot \text{h} \cdot \text{MPa})$
E_5	72.4	kJ/mol
A_6	$7.47 \cdot 10^8$	$\text{mol}/(\text{kg}_{\text{cat}} \cdot \text{h} \cdot \text{MPa})$
$E_{6,0}$	97.2	kJ/mol
A_7	$1.0 \cdot 10^{-3}$	MPa^{-1}
ΔH_7	-25.0	kJ/mol
A_{5M}	$8.43 \cdot 10^5$	$\text{mol}/(\text{kg}_{\text{cat}} \cdot \text{h} \cdot \text{MPa})$
E_{5M}	63.0	kJ/mol
A_{6E}	$7.03 \cdot 10^8$	$\text{mol}/(\text{kg}_{\text{cat}} \cdot \text{h})$
$E_{6E,0}$	108.8	kJ/mol
ΔE	1.12	$\text{kJ/mol}/\text{CH}_2$

Source: (Todic, et al., 2013)

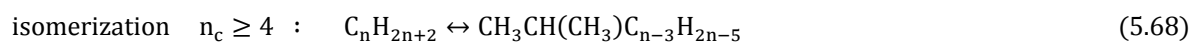
5.5.2 FT wax hydro-cracking

The approach illustrated in [Pellegrini et al., 2008] for the modelling of wax hydrocracking reaction is based on the Langmuir-Hinshelwood-Hougen-Watson (LHHW) mechanism for heterogeneous reactions. The LHHW approach allows describing adsorption of reactants to acid and metal sites on catalyst surface, reactions between the adsorbed reactants and intermediates and desorption of products. The aim of their work was to develop a hydrocracking reactor model accounting for H₂/waxes ratio effect, which is not feasible without considering vapor-liquid equilibrium (VLE). The authors wanted to improve and integrate previous hydrocracking model from [Pellegrini et al., 2004, 2007a] that considered the presence of only the vapor phase inside the reactor. The kinetic equations were thus written by [Pellegrini et al., 2008] in terms of fugacity, which at equilibrium is the same for both vapor and liquid. The reaction rate constants for each product molecule was derived fitting the reaction model equations to experimental results (analyzed by gas chromatography - GC) for hydrocracking of paraffins from C₄ to C₇₀

carried out into a trickle-bed reactor charged with Platinum and supported on amorphous silica-alumina.

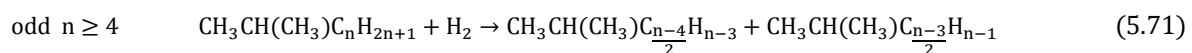
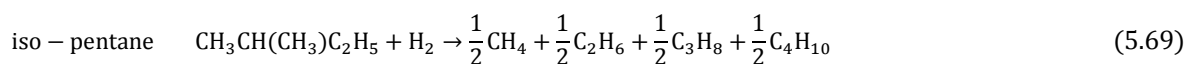
The authors made some assumption for simplifying the reaction model; first of all they reduced the isomer class to mono-methyl alkanes (lumping process), on the basis of the experimental results that posed in evidence that the major part of the isomers was constituted by molecules with only one methyl branch in the side chain. Then, each of these methyl-alkanes was supposed to break in the middle of the chain. This assumption come from carbon number spectra of the products obtained by primary hydrocracking of light hydrocarbons (C₈-C₁₆) reported in literature works [Froment, 1987; Sie, 1993], where all the hydrocarbon fragments seemed to be produced in the same amounts, except for C₁, C₂ and C₃ fragments. In order to include the fraction of lighter hydrocarbons into the model without introducing excessive complications (such as a proper breakage distribution function), the reaction scheme proposed by [Pellegrini et al., 2008] presents a different way of cracking for iso-pentane.

Based on the aforementioned assumptions, the simplified reaction stoichiometry for the isomerization-cracking sequence can be represented as follows:



wherein each of the n-paraffin heavier than propane has been considered at chemical equilibrium with its branched mono-methyl isomer (from well-known experimental evidence).

Indeed the rate limiting step of the reaction sequence is the scission of the carbenium ion into small fragments. From the assumptions made before the cracking reaction results into different products whether are considering n-paraffin with odd or even carbon number, or the particular case introduced for iso-pentane:



Moreover it' s clear that isomerization and cracking reactions are viewed as single events, thus neglecting the presence of intermediate species and their diffusion between different functional sites.

After having defined the set of hydrocracking reactions, applying the LHHW methodology to the reaction scheme, (Pellegrini et al, 2008) derived the rate of isomerization and cracking which are reported here below:

$$r_{isom}(n) = \frac{k_{isom}^0(n) e^{\frac{-E_{isom}(n)}{RT}} (fug_{n-c}(n) - \frac{1}{K_{eq}(n)} fug_{iso-c}(n))}{ADS} \quad (5.72)$$

$$r_{cr}(n) = \frac{k_{cr}^0(n) e^{\frac{-E_{cr}(n)}{RT}} fug_{iso-c}(n)}{ADS} \quad (5.73)$$

Where

- $k_{isom}^0(n)$: pre-exponential factor of isomerization of n-alkane with n carbon number;
- $k_{cr}^0(n)$: pre-exponential factor of cracking of iso-alkane with n carbon number;
- $E_{isom}(n)$: activation energy for isomerization reaction of n-alkane with n carbon number;
- $E_{cr}(n)$: activation energy for cracking of iso-alkane with n carbon number;
- $K_{eq}(n)$: equilibrium constant for isomerization of n-alkane with n carbon number;
- $fug_{n-c}(n)$: fugacity (at VLE) of n-alkane with n carbon number;
- $fug_{iso-c}(n)$: fugacity (at VLE) of iso-alkane with n carbon number;
- $ADS = fug_{H_2} [1 + \sum_{i=1}^{70} K_{L_{n-c}} fug_{n-c} + \sum_{i=4}^{70} K_{L_{iso-c}} fug_{iso-c}]$: adsorption factor, in which $K_{L_{n-c}}$ and $K_{L_{iso-c}}$ are the Langmuir adsorption constant that govern the adsorption of n-alkanes and iso-alkanes onto the hydrogenating and the acidic sites, respectively;

As reported in [Pellegrini et al., 2008], the kinetic parameters have been estimated by fitting the experimental data through polynomial or exponential correlative expressions as a function of the carbon number of the species revealed during the experiments:

$$K_{L_{n-c}} = 10.3 e^{0.40 n} \quad \frac{1}{Pa} \quad (5.74)$$

$$K_{L_{iso-c}} = 20.0 e^{0.10 n} \quad \frac{1}{Pa} \quad (5.75)$$

$$E_{isom}(n) = 2.23 \ln(n) \times 10^4 + 1.20 \times 10^5 \quad \frac{kJ}{kmol} \quad (5.76)$$

$$E_{cr}(n) = (3.06 \ln(n) + 8.75) \times 10^4 \quad \frac{\text{kJ}}{\text{kmol}} \quad (5.77)$$

$$k_{isom}^0(n) = 3.88 n^{7.70} \times 10^{17} \quad \frac{\text{kmol}}{\text{kg}_{cat}\text{h}} \quad (5.78)$$

$$k_{cr}^0(n) = 1.52 n^{7.63} \times 10^{16} \quad \frac{\text{kmol}}{\text{kg}_{cat}\text{h}} \quad (5.79)$$

$$K_{eq}(n) = 1.24 n^2 - 1.15 n \times 10^{-2} + 5.20 \times 10^3 \quad - \quad (5.80)$$

The values are in line with the literature data, in particular satisfying the following physicochemical constraints:

- Langmuir constants for n-paraffins are greater than those for iso-paraffins with equal carbon number:

$$K_{L_{n-C}}(n) > K_{L_{iso-C}}(n) \quad (5.81)$$

- Activation energies for isomerization reactions are similar to those for cracking reactions as reported in literature [Martens et al., 1986];
- Equilibrium constants increase with the number of carbon atom.

This section holds all the process units that allow producing syngas from combined CO₂ and steam reforming of methane with the specific features required by LTFT synthesis, in terms of H₂/CO ratio, temperature and pressure.

The natural gas (NG) feed stream is supposed to come from any natural gas source with no local market (i.e. either from “stranded” reservoirs or co-produced with petroleum or placed on the top of petroleum reservoirs). The composition of the natural gas employed is shown in (Tab. 6.1). Natural gas enters the plant at 5 bars and 50 °C and it is pre-heated up to 150 °C.

The carbon dioxide (CO₂) stream, entering the plant at 25 °C and 1.5 bars, is supposed to come from the condensing unit of a distillation column (stripper) of an amine plant, which separates carbon dioxide and other acid gases from the flue gas stream after fuel combustion. The fuel which is combusted it is composed of the unreacted gases from the FT reactor that are not recycled, or vent stream (VENT). The heat generated from combustion of un-recycled gases can be employed at the aim of supplying some of the heat of reaction required by the reforming unit.

Table 6.1: composition of the feed fuel NG [*Union Gas* – Canadian natural gas storage company – web site].

Components	Mole %
CH ₄	94.9
C ₂ H ₆	4.2
C ₃ H ₈	0.3
n-C ₄ H ₁₀	0.06
n-C ₅ H ₁₂	0.02
n-C ₆ H ₁₄	0.01
CO ₂	0.4
O ₂	0,01

N2	0.1
----	-----

The carbon dioxide in the flue gas stream from unrecycled (and combusted) gases is compressed to 5 bars and mixed with feed natural gas and water vapor stream (STEAM-3). Last stream comes out from a series of heat recovery exchangers, where the feed water flow (H₂O) is heated up to vaporization by a countercurrent flow of gas products and unreacted gases from FT reactor (HEX-X4) and of syngas exiting the reformer (HEX-X3), that has to be cooled before the separation of the water that has not reacted in the reforming unit.

The mixed stream of natural gas, water, carbon dioxide and the recycled stream of unreacted gas from FT product separation are heated up to the temperature needed by the pre-reformer (850 °C) by exchanging heat (HEX-X1) with the countercurrent flow of syngas exiting the reformer.

The reforming unit includes two reaction units: the pre-reformer (PRE-REF) and the reformer (REF-R) operation unit. Temperature and pressure of the pre-reformer are set at 550 °C and 5 bars. Under these conditions, almost all C₂+ hydrocarbons contained in the recycled gas from the FT reactor and the fresh feed natural gas are converted into methane in the pre-reformer. For simulating pre-reformer the RGibbs model has been employed including chemical (and phase) equilibrium for C₁-C₄ hydrocarbons (in the *PRE-REF/Setup/Specifications*, "Calculate restricted phase equilibrium and chemical equilibrium" option is selected). The mixture of fuel

(almost only composed of methane), carbon dioxide and water (partially reacted at the pre-reformer level) is heated up to the temperature specified at the reformer reactor (850 °C), first exchanging heat with the countercurrent flow of syngas exiting the reformer (HEX-X2) and then externally heated up to the reforming temperature (HEX-H4).

Here, it can be assumed that the two reforming reactions (CO₂ and steam based methane reforming) reach chemical equilibrium, since the reaction rates are very fast at elevated temperatures. In order to simulate the reformer well (a burner type reformer) "Restricted chemical equilibrium" option is implemented in the RGibbs model under the *REF-R/Setup/Specifications* options, as done for the pre-reformer unit.

The syngas exiting the reformer at high temperature, after a series of cooling steps in the feed pre-heat exchangers, enters a water cooled heat exchanger (HEX-C1) where it is

cooled down to the temperature set at the flash reactor (FLASH-1), where water is separated as liquid.

6.2 Syngas conversion unit

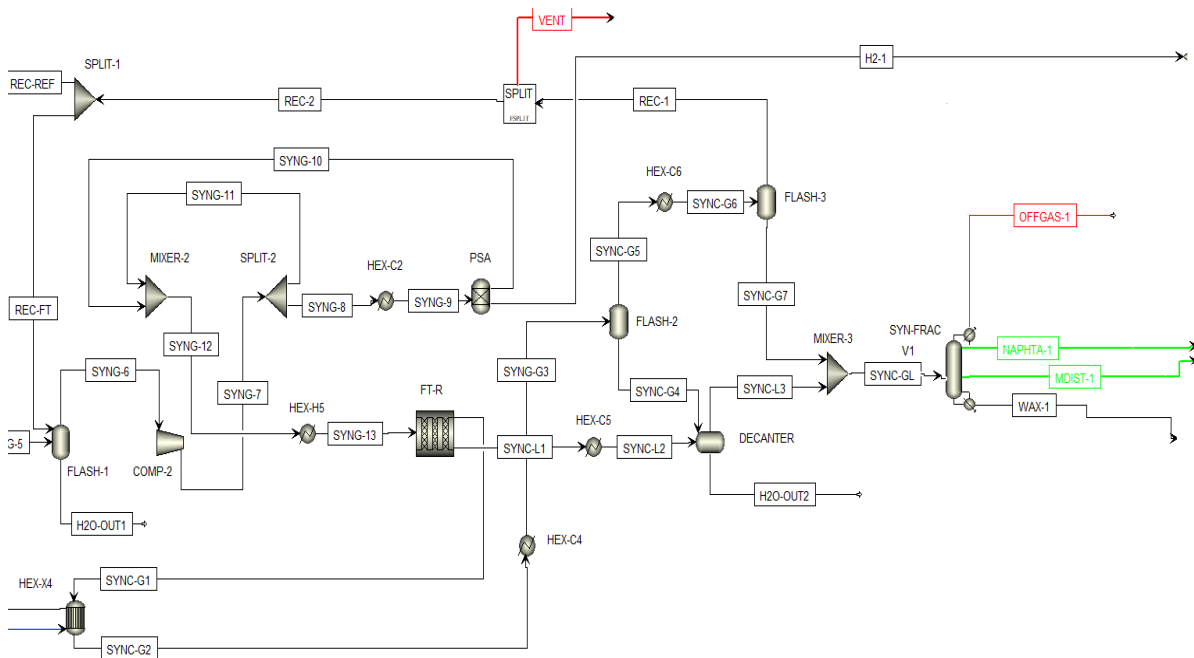


Figure 6.2: Fischer-Tropsch synthesis unit and product separation unit flowsheet section. Green lines: product streams (naphta (C5-C10) and middle distillate (C11-C22)). Red lines: tail gas and vent gas (to combustion and CO₂ separation units).

The syngas utilization section embeds the Fischer-Tropsch reaction unit and the first main distillation unit.

Syngas exiting the heat recovery exchanger is further cooled down to near the ambient temperature and mixed with the recycled gas stream from a split unit (SPLIT-1) that spreads out the flow between syngas generation and utilization unit. A flash unit (FLASH-1) separates water from the main flow.

The syngas is then compressed up to the pressure of the reaction unit (20 bars). The compressor (COMP-1) has been designed with 75 % ASME polytropic efficiency.

A part (7.5 % of total flow) of the flow is separated from the main flow (SPLIT-2) and, after cooling (HEX-C2), it is allocated to the Pressure-Swing-Adsorption (PSA) unit where hydrogen with 99.5 % purity is produced and then sent to the hydrogen-treatment units (natural gas desulfurization and hydro-cracking units). The fraction of the flow to be submitted to PSA has been selected at the aim to guarantee a hydrogen-to-wax feed ratio of 0.05 [$\text{kg}_{\text{H}_2}/\text{kg}_{\text{WAX}}$] at the entry of hydro-cracking section [Pellegrini et al., 2008] (Cap. 6.3).

The hydrogen-lean flow from PSA unit (SYNG-10) is then mixed with the main flow (MIXER-2) and heated up to the temperature used in FT synthesis reactor (230 °C).

A gas mixture of syngas and other hydrocarbons reacts across the FT reactor, which has been designed and charged so as to achieve 2000 [$\text{kg}_{\text{cat}}/\text{m}^3$] cobalt-based catalyst reactor density and 0.6 void fraction (for pressure drop limitation).

Gas product flow from the FT synthesis unit is then cooled down passing through a heat recovery exchanger (HEX-X4), while pre-heating up the fresh feed water flow.

Water in the gas product flow is totally condensed by cooling it into an external heat exchanger (HEX-C4) and separated at the level of a flash reactor (FLASH-2). The output gas from the flashing unit is further thermally treated (i.e. cooled down) to condense the light fraction of hydrocarbon products still present. This fraction is separated as liquid from the subsequent flash unit (FLASH-3) and sent to the collective distillation column. The gas portion from flashing, mainly made of un-condensable gases (un-reacted and light gas products from FT unit), is split between recycled (REC-2) and vented (VENT) gas lines. The recycled fraction is further split between the reforming (REC-REF) and Fischer-Tropsch (REC-FT) unit section.

The liquid fraction of products from FT reactor is directly cooled (HEX-C5) and sent to a decanter unit (DECANTER) that separates condensed water from hydrocarbon fuels. The decanter unit accepts the liquid streams from condensed gas products (SYNC-G4) and liquid products (SYNC-L2).

The hydrocarbon liquids from the decanter are mixed with that from the condensed gas flash units and sent to the collective distillation column (SYN-FRAC).

The distillation column is modelled by means of a RAD-FRAC unit operation model. The column is structured as 20 stages (number of trays) column, with a simple reboiler (*Kettle*) and *Reflux ration* and *Bottoms to feed ratio* as operating specifications. The reflux ratio doesn't exceed 2.5 during all of the runs in the simulation. The distillate exiting the top

of the column (condenser) embeds light hydrocarbons, which typically form naphta fuel (NAPHTA-1), while middle distillate (MID-DIST-1) comes out from one of the internal trays and includes kerosene and diesel fuel fraction. The bottom tray collects the heavier part of the feed: an externally driven reboiler partially evaporates the heavy fraction of the feed and the remaining fraction, which is still liquid (WAX-1), goes through the third part of the plant (hydro-cracking unit) to be partially recovered as liquid automotive fuel.

6.3 Upgrading unit

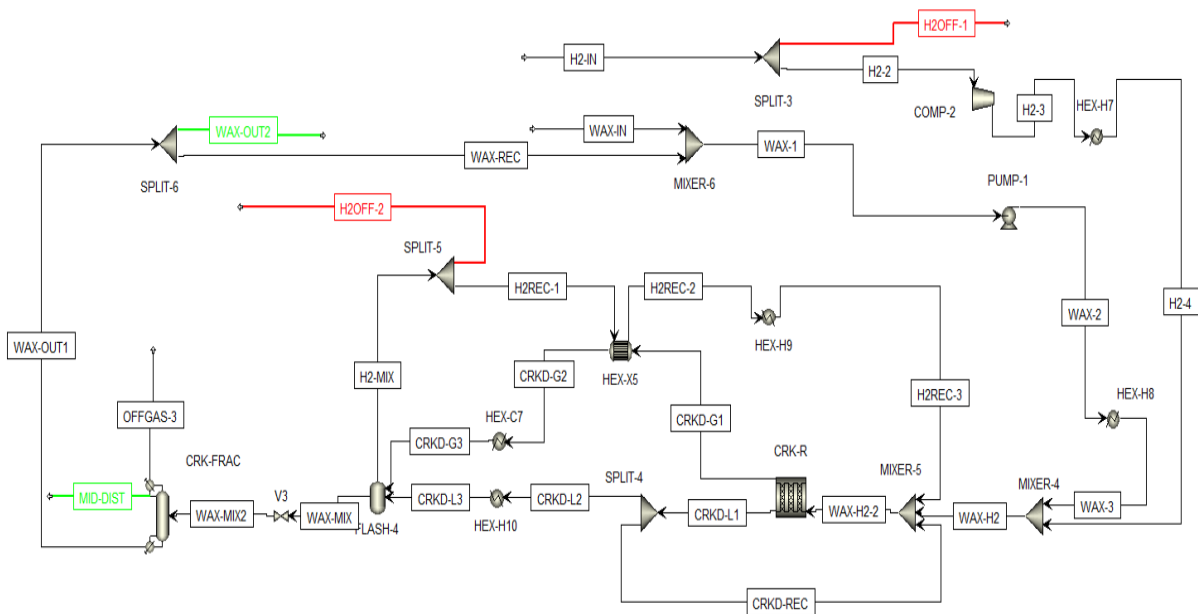


Figure 6.3: hydro-cracking and fuel product distillation unit flowsheet section. Green lines: products streams (middle distillate (C11-C22) and waxes (C23-C70)). Red lines: waste streams (hydrogen to electric generation or thermal recovery units).

The third and last of the main parts of a Gas-to-Liquids plant involving low temperature (200-240°C) of synthesis turns to be the hydro-cracking unit, designed to recover the heavier fractions (C23-C70) of hydrocarbons produced into the FT section. Treating them with hydrogen at high pressure and temperature onto a platinum-alumina catalyst they

isomerize and subsequently break up into smaller molecules. Hydrogen for chemical treatment is produced in the reforming section together with the main syngas stream and then purified by Pressure-Swing-Adsorption (in the FT section).

The hydrogen-rich stream flow (H2-IN) is compressed to 50 bars (COMP-2) and then heated up to 360 °C (HEX-H7). In parallel to the hydrogen-rich stream the liquid stream of heavier hydrocarbons from distillation (WAX-IN) is mixed with the recycled portion (WAX-REC) of the wax-based mixture exiting the plant (WAX-OUT1) and then pumped and heated up to the hydrogen pressure and temperature.

The mixture of hydrogen and heavier hydrocarbons is further mixed with two recycle lines, one for recirculating unreacted (normal paraffin waxes) or partially reacted (iso-paraffin waxes) hydrocarbons of the liquid stream drawn out from the bottom of the reactor (CRKD-REC) and one for the reutilization of the unreacted gas fraction (CRKD-G1), made substantially of hydrogen.

The reactor has been modelled as a plug-flow reactor, as for the Fischer-Tropsch unit. Temperature and pressure are set at the constant values of 360 °C and 50 bars and design and catalyst charging are set so as to achieve 2000 [kg_{cat}/m³] Pt-alumina hydro-cracking catalyst reactor density.

A gas flow stream exits the top of the reactor (CRKD-G1) and enters a recovery heat exchanger (HEX-X5) where it heats the countercurrent stream flow of un-reacted gases that are recycled (H2REC-1). The recycled stream completes the heating process into an externally driven heat exchanger (HEX-H8). The gaseous products are then externally cooled down to the temperature at which recycled gaseous and liquid products are separated (into the flash unit FLASH-4).

The unrecycled fraction of liquid products drawn out from the bottom of the reactor goes through the same flash unit to separate un-condensable gases.

A part (H2OFF-2) of the unreacted hydrogen (H2-MIX) goes through a recovery section (not represented in figure) for providing thermal or electrical needs (pumps, compressors and controllers) or to other hydro-treatment process throughout the plant (i.e. the pretreatment unit, not analyzed in this work).

The liquid fraction from the flash is decompressed to 5 bars and then submitted to the distillation tower (CRK-FRAC), which has been modelled as RAD-FRAC unit operation model type. A column of 10 stages and a simple reboiler (*Kettle*) with imposed *Reflux ratio* (never exceeding 2.5) and *Bottoms to feed ratio*, reveals to be sufficient to distillate the main cuts of the feed: a middle distillate fuel cut (MID-DIST) that composes the liquid stream from the condenser unit, and a heavier fraction of waxes from the bottom tray

(WAX-OUT1). The last heavy stream is partially recycled back to the hydro-cracking reactor, while the un-recycled portion has been assumed as it is valuable product (WAX-OUT2) from the plant.

7. RESULTS AND DISCUSSION

Results from first simulations of the integrated GTL process model reflect the main feature of this type of plant: a strong endothermic balance of the first section (reforming), an opposite behavior for the second section (Fischer-Tropsch unit) and an approximately neutral balance at the hydro-treatment unit (third section) (Table 7.2).

However, lower temperatures of the synthesis (230 °C) does not allow for supplying the heat request of the syngas production unit (850 °C), whose energy demand can be satisfied only by combustion of additional fuel (natural gas).

The considerable amount of fresh feed water (H₂O/NG equals 1.5) should help avoid carbon deposition at the reformer level.

Moreover, a large portion of FT synthesis reactants (syngas) and inert components (unreacted natural gas and carbon dioxide at reformer unit) flows out the FT reactor (without reacting) together with a significant quote of methane by-produced from FT synthesis (Table 7.1).

At the hydro-treatment section, it has been noted that a very large recycle of unreacted waxes and hydrogen into the hydro-cracking reactor is necessary for achieving appreciable values of conversion.

Following are the balance (mass and energy) outcomes from ASPEN Plus simulation for main units of the GTL integrated plant.

Material balance

FEED [kmol/hr]		PRODUCTS [kmol/hr]			
NG	1500	NAPHTA	18.4		
CO ₂	700	MID. DIST.	21.0	(9% branched)	
H ₂ O	2250	WAX	22.3	(20% branched)	
REFORMER [kg/hr]		FT REACTOR [kg/hr]		HC REACTOR [kg/hr]	
79832		99773		wax	11564
				hydrogen	579
CO ₂ EMISSIONS		FT INERTS			

[kmol/hr]	[kmol/hr]	
999	CO2	453
	CH4	92

Table 7.1: mass and mole balance results from ASPEN Plus simulation run without recycle [base case].

Energy balance

FEED [LHV] [MW]		PRODUCTS [LHV] [MW]		
NG	342	NAPHTA	23	
CO2	-	MID. DIST.	61	(10% branched)
H2O	-	WAX	150	(18% branched)
REF. REACTOR [MW]		FT REACTOR [MW]		HC REACTOR [MW]
pre-reformer	16.9			
pre-heater	3.6	55		0.01
reformer	76.9			
VENT GAS [LHV] [MW]				
115.3				

Table 7.2: energy (heat) balance results from ASPEN Plus simulation run without recycle [base case].

7.1 Effects of recycle

A series of simulation runs are conducted under the prescribed process conditions mentioned in Table 7.1. The aim has been to analyze the effects of recycle ratio of unreacted gases mixture on reactor sizes, process efficiency, product selectivity and green-house-gases (GHG) emissions.

In particular 13 different recycle ratios are applied in order to monitor the behavior of the GTL process, at the aim to find the best process configuration in terms of performance.

The process of the study is designed to produce 2700 barrels of FT synthetic oil (C5+) per day and so as to achieve an optimum syngas reactant feed ratio (H₂/CO) at the entrance of FT reactor (that can vary in the restricted range of 2.075 - 2.08).

In order to simultaneously reach the aforementioned prescriptions the molar ratio of the fresh feed (H₂O/NG and CO₂/NG) are continuously varied into a restricted range (Table 7.1) while changing the amount of recycle.

Actually, different recycle ratios lead to changes in the syngas ratio, in particular the amount of CO increases with respect to H₂, i.e. the syngas ratio decreases with increasing recycle ratio. This is due to the increase of CO₂ flow rate at the entrance of the reformer due to the additional quantity supplied by the recycle line. The ratio of CO over H₂ produced by CDR would be higher than SMR. In other words, the activity of CDR (carbon dioxide reforming) would increase with respect to SMR (steam methane reforming) with increasing recycle. This means that in order to achieve an optimum syngas ratio (from 2.075 to 2.08) the carbon dioxide molar feed ratio should be decreased or/and the water feed ratio increased with increasing recycle ratio.

A clear benefit of this type of reformer is the syngas composition flexibility due to the contemporary occurring of CDR (carbon dioxide methane reforming) and SMR (steam methane reforming) reactions.

The molar feed ratio of fresh feed CO₂/NG/H₂O turns to vary in the range (0.51-0.23):1:(1.5-1.78) during all of the simulation runs, as depicted in Table 7.1.

Table 7.3: simulation case studies and relative operating parameters used at varying recycle ratio.

Recycle ratio ⁽¹⁾	Feed H2O/NG CO2/NG		Reformer	Syngas	FT reactor	Split ratio ⁽²⁾	Recycle ratio (HC) ⁽³⁾
0	1.500	0.513		2.078			
0.1	1.517	0.503		2.079			
0.2	1.535			2.078			
	0.489						
0.3	1.533			2.078			
	0.474		850 [°C]		230 [°C]		
0.4	1.550			2.078		0.6	0.6
	0.454		5 [bar]		20 [bar]		
0.5	1.568			2.079			
	0.432						
0.6	1.596			2.078			
	0.408						
0.7	1.626			2.076			
	0.378						
0.8	1.672	0.341		2.077			
0.9	1.719	0.290		2.076			
0.95	1.732			2.077			
	0.258						
0.975	1.758			2.079			
	0.242						
0.99	1.780	0.231		2.078			

(1) Recycle ratio = recycle gas / total un-reacted gas.

(2) Split ratio = recycle to FT reactor / total recycle.

(3) Recycle ratio (hydro-cracking) = H2 recycled to hydro-cracking reactor / total un-reacted H2 from gas-liquid product separation.

7.1.1 Effects of recycle on reactor sizes

It is obvious that the recycle line (Figure 6.1) in the reformer section is able to provide additional amounts of unreacted by-products, such as CO₂ and CH₄, at the entrance of the reformer, where they behave as active components. Therefore, at the same productivity, the fresh feed supply of CO₂ and CH₄ can be largely reduced; in particular the flow rate of fresh CH₄ is strictly related to the operating cost of GTL plants. Therefore, the higher is the recycle ratio the lower are the cost of plant operation.

However, raising the recycled gas flow rate (at constant space velocity) into a reactor should require reactor with higher volumes and this clearly affects a significant piece of capital cost for GTL plants. This is true mainly for the FT reactor, where recycled CO₂ and CH₄ behave as inert material for FT synthesis. CO₂ and CH₄ together with H₂ and CO are major components in the recycle line. Recycled methane comes from that unreacted in the reformer section and from that by-produced at the FT reactor level, whereas recycled CO₂ is only that unreacted at the reforming step by CDR reaction. In turns, the higher the recycle ratio the higher the mole flows of inert materials (Figure 7.2) through the FT reactor. Therefore, the recycle itself and the aforementioned accumulation of inert materials in front of reactor clearly cause larger mass/volume flow rate (Figure 7.1) at the exit of the FT reactor. Larger mass/volume flow rate induce in turns larger reactor volumes (significantly affecting capital cost). Moreover the accumulation of inert materials affects the level of conversion in the FT reactor, which shows a slight decrease with increasing recycle (from 82 to 79 %). A decrease of conversion forces the reactors to more severe operation conditions or the catalyst loading to be increased.

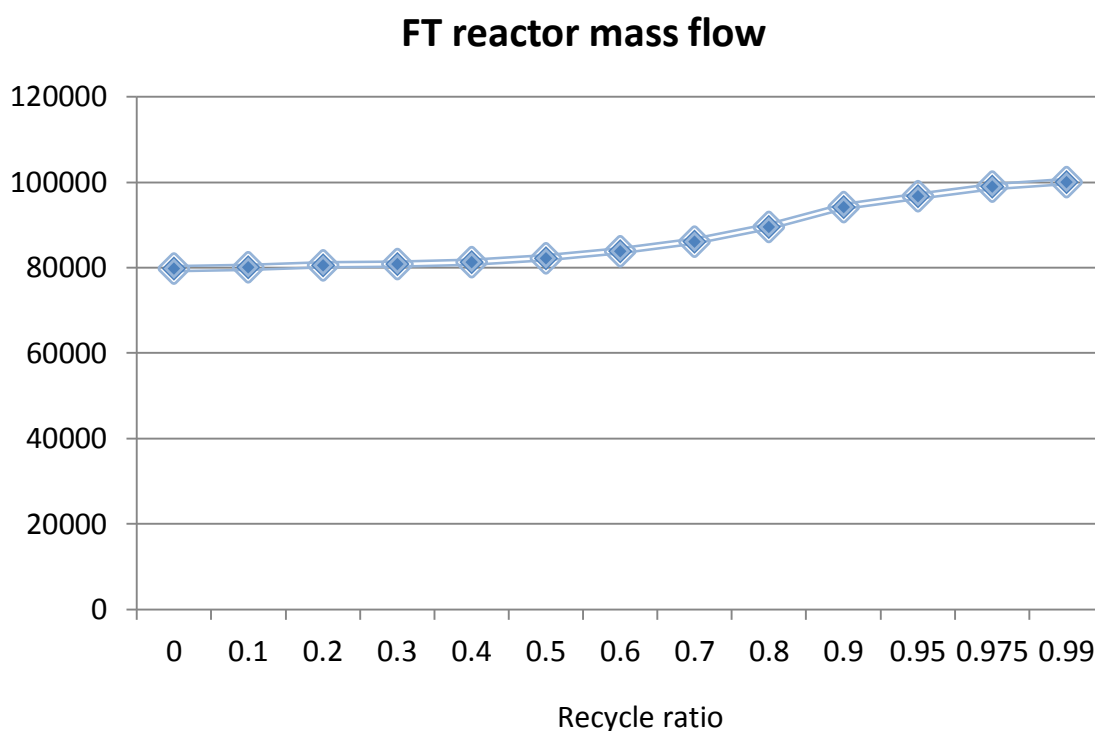


Figure 7.1: mass flow rate [kg/hr] at the entrance of FT reactor.

The mole fraction of inert components (Fig. 7.2) shows that CO₂ and CH₄ accumulate with the same trend at the FT reactor inlet. This is due to the presence of CDR reaction at the reformer level, which leads to consumption of CH₄ and CO₂ as reactants. And since with increasing recycle the fresh feed NG fuel and CO₂ are simultaneously reduced, they are consumed to the same extent with varying the recycle.

Moreover, it should be noted that CO₂ accumulates to a higher extent with respect to CH₄ for each value of recycle ratio. This is due to the weight of SMR reaction over CDR at the reformer level. Actually, the hydro-cracking unit needs large amounts of hydrogen for the subsequent intensive FT wax hydro-treatment. Hydrogen is fully produced at the reformer level and it is drawn out from the reformer down process (but before the FT reactor). Therefore, in order not to lower the syngas ratio (due to hydrogen deficit in the syngas) and maintain the syngas ratio within the optimum value range (2.075-2.08) at FT reactor inlet, an additional amount of fresh H₂O over fresh CH₄ (H₂O/CH₄) is necessary. Therefore, the conversion of CO₂ through CDR reaction results lower than that of CH₄ (through CDR and SMR). This causes the aforementioned major level of accumulation of CO₂ at the FT reactor inlet with respect to CH₄.

Finally, it can be also noted that CH₄ accumulation level increases more rapidly than CO₂ with increasing recycle ratio. This could be related to the aside effect of accumulation of

inert material at the FT reactor level on the methane formation by FT synthesis. Actually, accumulation of inert material leads to reduced CO partial pressure due to lower reactant total pressure. A decrease of CO partial pressure can decrease the overall chain growth probability favoring the increase of selectivity for methane (and light species) over heavier species at the catalyst site. Therefore, since increasing the amount of recycle has the effect of rising the entity of accumulation and, furtherly, a large portion (60 %) of this extra methane is recirculated (REC-FT) to the front of the FT-reactor, even more methane is accumulated in front of reactor with increasing recycle (with respect to CO₂).

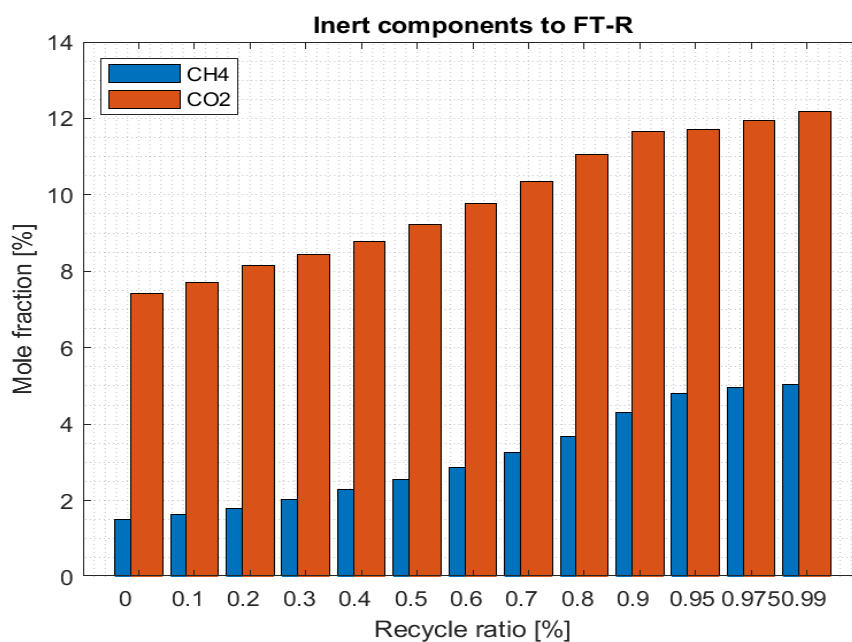


Figure 7.2: mole fraction of inert components in front of FT reaction inlet.

On the opposite side, the flow rate at the reformer inlet shows a different trend with respect to the FT reactor: the results show a descendent trend of the mass flow rate at the reformer inlet (Fig. 7.3).

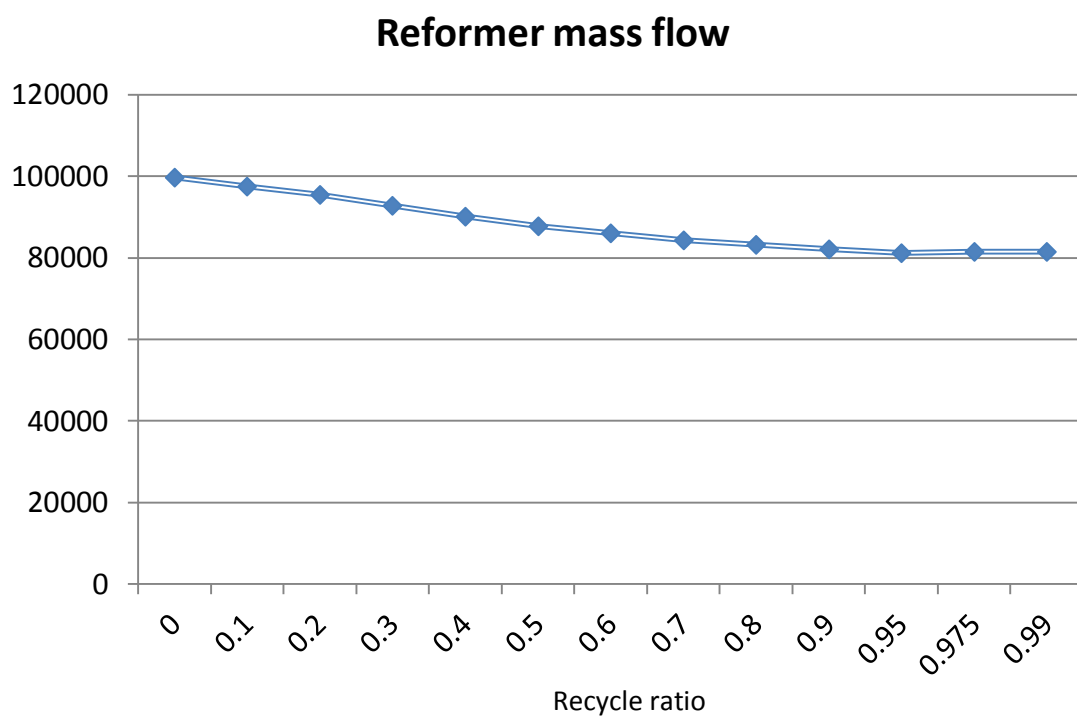


Figure 7.3: mass flow rate [kg/hr] at the reformer exit.

This is due to the fact that CO₂ and CH₄ are both active components in this reformer. Since they are supplied by the recycle itself the amounts of fresh CO₂ and CH₄ can be largely reduced with increasing the recycle ratio. Moreover, fresh feed CO₂ has to be reduced in order to prevent higher degree of accumulation at FT reactor level. And the reduction of CO₂ at the reformer level is the major contribute to the decrease of mass flow rate through the reactor with the increasing of recycle.

7.1.2 Effects of recycle on process efficiency

As it has been introduced in the description of the process model (Par. 6.1) and (Par. 6.2), it is supposed that the amount of unreacted gases that are not recycled, or vent stream (VENT), composed of syngas and other light hydrocarbons can be used as fuel for the burner-type reformer, supplying some of the heat required by the endothermic CO₂ and steam combined reforming reactions. Therefore, less recycle ratio can provide more vent gas, thus more fuel for the burner-type reformer. This can improve the thermal efficiency of the plant. Thermal efficiency is defined in this work as following:

$$EFF_{th} = \frac{\text{LHV of products}}{\text{LHV of total NG entered}} \quad (7.1)$$

The numerator collects the lower heating values of the synthetic hydrocarbon products streams (naphta, middle distillate and waxes drawn out from the plant, i.e. the green bold line streams in Figure 6.1 and 6.3). The denominator is the lower heating value of the fresh feed natural gas supplied at the plant inlet (blue bold line stream in Figure 6.1 plus that needed to supply the entire heat duty of the reformer section).

The reformer section includes three main heat sinks: the pre-reformer (PRE-REF), the pre-heat exchanger (HEX-H4) that allows the reforming reactants to reach the reaction temperature (850 °C) and the reformer itself (REF-R). For two cases in this study (when recycle ratio equals or stays below 0.1), the heat energy required by the reformer can be fully compensated by the vent stream gas. Instead, for the other cases (recycle ratio value above 0.1), the energy derived from the vent stream is not sufficient to fully supply the thermal request of the reformer section.

Thus, higher is the recycle ratio higher is the quantity of additional NG fuel that is necessary to satisfy the plant energy demand.

In particular, it has been assumed that the overall heat transfer efficiency of main endothermic unit (that includes reformer, pre-reformer and high-temperature pre-heater) equals 0.9. This means that the quantity of heat to be supplied equals the reformer heat duty/0.9. Therefore, the thermal efficiency can be re-written considering two cases:

If the heat retrieved from vent gas stream exceeds the effective thermal need, i.e. heat duty/0.9:

$$EFF_{th} = \frac{\text{LHV of products}}{\text{LHV of fresh feed NG}} \quad (7.2)$$

Conversely, if the heat retrieved from vent gas doesn't exceed the value of heat duty/0.9:

$$EFF_{th} = \frac{LHV \text{ of products}}{LHV \text{ of fresh NG entered} + \text{heat duty}/0.9 - LHV \text{ of vent gas}} \quad (7.3)$$

LHV of products, vent gas and fresh feed natural has been computed by processing these streams (at 25 °C and 1 bar) into ASPEN Plus *RStoich* combustion reactors, feed by stoichiometric oxygen at 25 °C and 1 bar, and working at 100 °C and 1 bar (water saturation temperature reactor pressure).

Figure (7.4) shows the value of thermal efficiency at different recycle ratios:

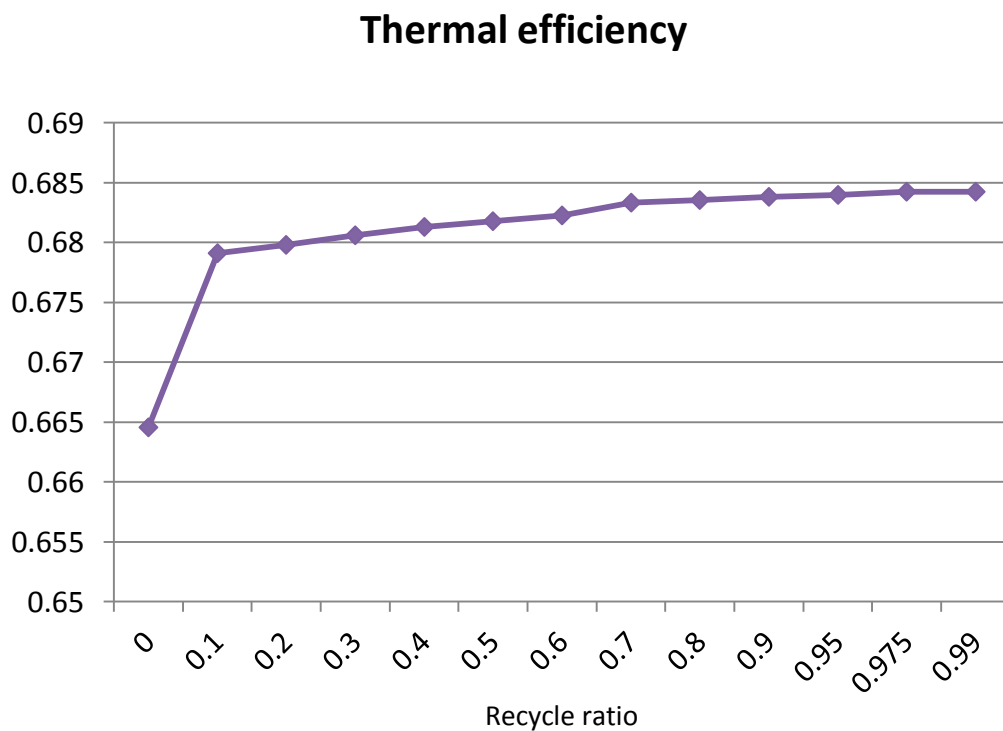


Figure 7.4: thermal efficiency at recycle ratio ranging from 0 % to 99 %.

It should be noted that the thermal efficiency slightly increases with increasing recycle ratio (almost monotonously for lower recycle and appear quietly constant at higher recycle ratio), whereas it falls downward at null recycle ratio. Last discontinuity in the process efficiency is due to the quantity of heat retrieved by vent gas stream that exceed

the necessary heat duty for the reformer (considering heat transfer efficiency). Actually, the extra quantity of heat cannot be used in the burner-type reformer directly and it should be wasted or used for less efficient heat exchange.

At recycle ratio of 0.1 the quantity of heat retrieved from vent stream compensate quite exactly for the reformer heat duty. The increase of thermal efficiency with increasing recycle, even if slight, is due to the additional quantity of CO₂ and CH₄ supplied at the reformer inlet with increasing the recycle ratio. Indeed, the fresh NG fuel and CO₂ feed can be largely reduced, i.e. the denominator in eq. (7.2) or (7.3) decreases, whereas the lower heating value of the fuel products stays more or less the same (the numerator in eq. (7.2) or (7.3)), respecting the aforementioned prescription of constant productivity.

The carbon efficiency is the parameter used to evaluate the conversion efficiency of any carbon source into valuable products for a XTL (something-to-liquids) process. The calculation of the carbon conversion efficiency has been made on a molar basis. The results are reported in Figure (7.5), where it is clear that the recycle has benefic effects on carbon conversion. The monotonic trend of carbon efficiency (ranging from 59 to 79 [%]) is the result of the amounts of fresh CO₂ and CH₄ (carbon sources) saved due to the recirculation effect of recycle. In other words, higher is the recycle ratio, lower turns to be the effective quantity of fresh carbon source to generate the same amount of carbon product.

Carbon efficiency

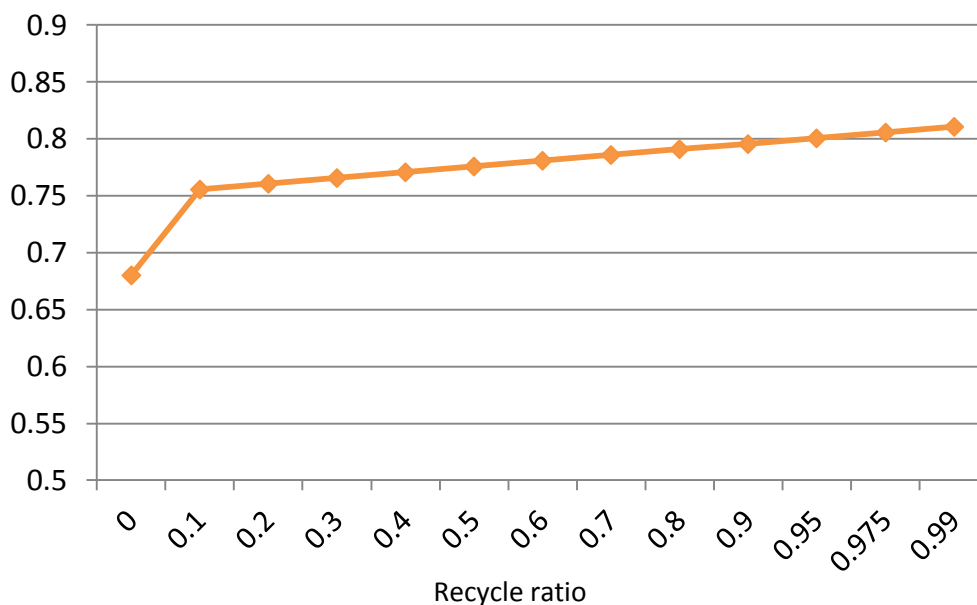


Figure 7.5: carbon efficiency at recycle ratio ranging from 0 to 99 %.

Another parameter useful to evaluate the efficiency of a GTL plant is the quantity of natural gas (in kilograms) needed to produce one kilogram of syngas. Since also CO₂ plays an important role as carbon source, it seems obvious that a SCR (steam-carbon dioxide combined methane reforming) reformer would be more performant than a simple SMR reforming reactor. Moreover, the effect of recycle has a clear benefit on the specific natural gas consumption, as it can be seen in Figure (7.6).

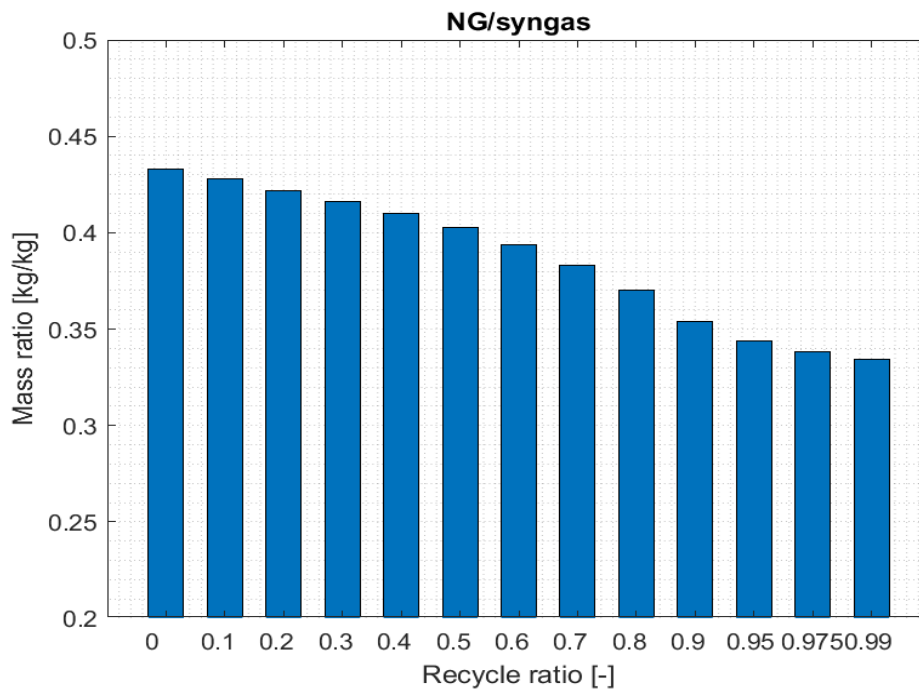


Figure 7.6: quantity of NG (kg) needed to produce 1 kg of syngas at various recycle ratios (0-99 %).

The syngas cost of the GTL plant under study decreases from 0.43 [kg/kg] to 0.33 [kg/kg] with increasing recycle ratio from 0 to 99 [%]. The recycle has the effect of increasing the unreacted CO₂ and CH₄ recirculated through the reformer section, where they act as active components, allowing a consistent portion of fresh feed NG and CO₂ to be saved while keeping the syngas flow rate (on a mass basis) almost constant.

7.1.3 Effects of recycle on green-house-gases (GHG) emission

The analysis of the effects of recycling the unreacted gases on CO₂ and CH₄ (the most representative green-house-gases) emission has been founded on the assumption that some of the unreacted gases in the vent stream (VENT) are used to supply the heat request of the plant. At this point, the CO₂ generated from combustion of vent gas can be extracted by use of absorption technologies, such as amine absorbers. Therefore, the derived pure-CO₂ stream can be opportunely re-used as a carbon source for the reformer.

Therefore, the quantity of CO₂ given off by the plant is directly related to the amounts of unreacted gases that are not recycled. In other words, CO₂ emissions reduce with increasing recycle ratio, as depicted in (Fig.7.7). The figure shows the ratio of CO₂ drawn out from the combusted vent gas over the fresh CO₂ feed to the plant.

It can be noted that the CO₂ generated is higher than that consumed (feed) at lower recycle ratio, implying that CO₂ cannot be fully re-used in these cases and it must be actually emitted into the atmosphere. However, this ratio continuously decreases with increasing recycle and quickly drops down at high recycle ratios. At high recycle ratios the CO₂ generated by combustion of vent gas turns to be not enough to satisfy the CO₂ feed demand of the plant.

The analysis of (Fig. 7.7) can infer that generated CO₂ and used CO₂ acquire the same value at 60-70 % recycle. This implies that CO₂ emission from the plant is nearly zero at this value of recycle.

CO2 emission

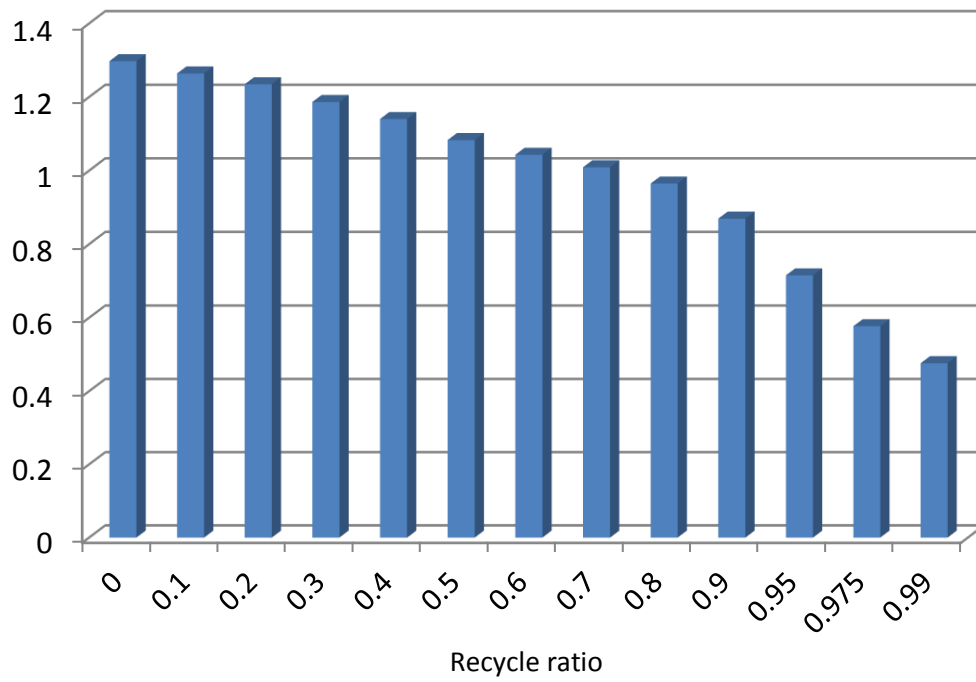


Figure 7.7: ratio of CO2 produced by combustion of vent stream over CO2 feed to the plant

7.1.4 Effects of recycle on plant selectivity

The analysis concerning selectivity of this plant is based on the assumption of equal productivity of the plant with varying recycle. Selectivity refers to the value of fraction of hydrocarbon fuel cut present in the overall product mixture. The different cuts are represented by naphta (C5-C10), middle distillate (C11-C22) and waxes (C23-C70). Each of these cuts is furtherly composed of different hydrocarbons, namely n-alkanes (n-paraffins), n-alkenes (n-olefins), methyl-alkanes (iso-paraffins).

The results are represented in the figures following:

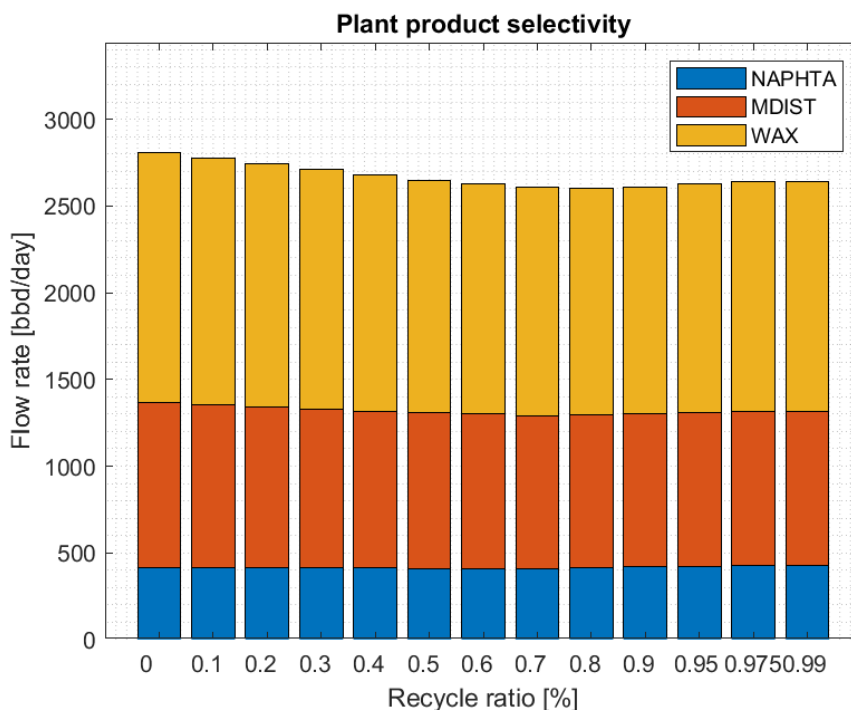


Figure 7.8: plant selectivity (barrels/day) in terms of main cuts (naphta, middle distillate and waxes) at various recycle ratios.

(Fig. 7.8) shows the trend of plant productivity and selectivity (in terms of the aforementioned cuts) with increasing recycle ratio and measured on a volume basis (barrels/day). It can be noted how productivity slightly changes during various recycle configurations. In particular, the total volume flow rate undergoes a little reduction with increasing recycle. This could be attributed to a slight reduction of conversion level at FT reactor level (from 82 to 79 %). Actually, the increasing partial pressure of inert

components at FT reactor entrance during the increase of recycle clearly reduces the reactant (H₂ and CO) partial pressure, slightly lowering the amount of produced liquid fuel (C₅+). Productivity of the plant reduces from 2800 [bbd/bay] at 0 [%] recycle to 2650 [bbd/day] at 99 [%] recycle. The major contribution to the reduction comes mainly from waxes, which reduces to a higher extent with respect to middle distillate and naphta (which is almost constant in the total range). This confirms what mentioned before about the decrease of FT conversion because FT reactor major products are mainly waxes (C₂₃-C₇₀).

The results of the analysis on the selectivity of each cut in terms of normal species (n-paraffins and n-olefins) and branched species (iso-paraffins) are reported below:

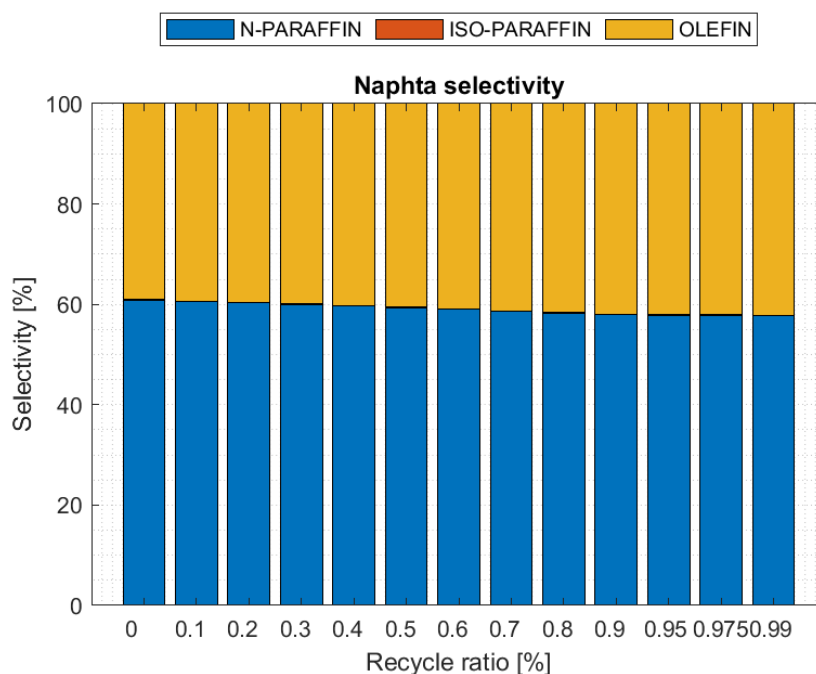


Figure 7.9: naphta selectivity (percent on a volume basis) in terms of different hydrocarbon species (n-paraffins, n-olefins and iso-paraffins) at various recycle ratios.

The three different hydrocarbon product species forming naphta fraction are represented in (Fig. 7.9). The branched cut (methyl-alkanes from C₅ to C₁₀) is completely absent. It can be considered obvious because of the isomerization and cracking activity of the different carbon species at hydro-cracking reactor level. According to the hydro-cracking mechanism adopted and as general rule for iso-cracking reactions, higher is the molecule size, higher turns to be the probability of isomerization and then cracking. Therefore,

molecules making up the naphta fraction are too small sized to be isomerized and the fraction of middle distillate that undergoes cracking (to form smaller naphta molecules) is negligible.

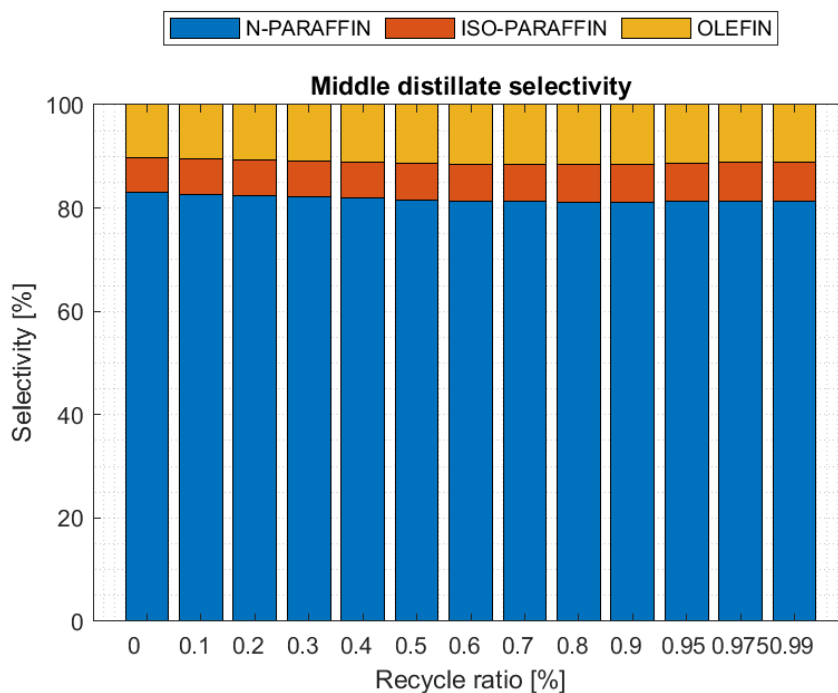


Figure 7.10: middle distillate (kerosene and diesel cuts) selectivity (percent on a volume basis) in terms of different hydrocarbon species (n-paraffins, n-olefins and iso-paraffins) at various recycle ratios.

The middle distillate cut comprises kerosene (C11-C14) and diesel (C15-C22) fuel fractions. Figure (7.10) depicts selectivity results for the middle distillate drawn out from two points of the plant (i.e. from the main distillation column of both FT synthesis section and hydro-cracking reaction section). The portion of middle distillate cut drawn out from the hydro-cracking section contains a not negligible fraction of branched species (mono-methyl-alkanes). Branched alkanes are necessary to improve the cold properties of normal paraffins forming diesel and kerosene fuel, as clearly explained in Par. (2.4). Volume percent of flow rate of the different species in the middle distillate product are exposed in Figure (7.10) for different recycle values. The volume percent of iso-paraffins attested to about 7 [%], normal paraffins reach 82 [%], while normal olefins are 11 [%] of the total. Moreover it can be noted as the fraction of branched paraffins slightly tends to increase with increasing recycle. This could be due to the increase of the H2/wax ratio, due to the

aforementioned slight decrease of selectivity for waxes with rising recycle at FT reactor level. An average value assumed for H₂/wax ratio in the plant of our concern is 0.05 [kg/kg], i.e. kilograms of hydrogen over kilograms of waxes at hydro-cracking section inlet. Therefore, lower conversion levels at FT reactor causes lower wax productions, while hydrogen drawn out from the PSA unit (Par. 6.1) (before the FT reactor inlet) remains about the same because the split fraction (SPLIT-2 in Fig.6.2) has been kept constant with changing recycle. Hence, higher H₂/wax ratios can increase the hydro-cracking activity, thus the amount of branched paraffins in the middle distillate mixture is increased and the cold flow properties improved with increasing recycle.

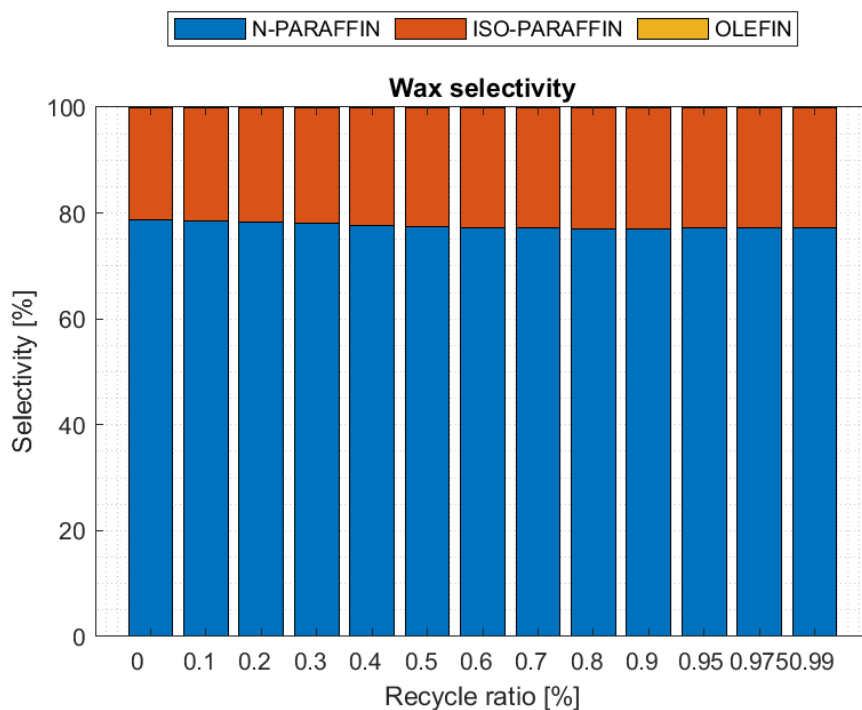


Figure 7.11: waxes (lubricants, heavy oils, plastics etc.) selectivity (percent on a volume basis) in terms of different hydrocarbon species (n-paraffins, n-olefins and iso-paraffins) at various recycle ratios.

The different hydrocarbon species forming the fraction of waxes and their volume (in percent) in different fuel products are represented in Figure (7.11). It should be noted that the olefin fraction is null, this because of the FT reaction mechanism (carbide mechanism) employed in this study, which causes an exponential decrease of olefin formation with increasing carbon number. This is the reason by which olefin volume percent is higher in the naphta cut and not negligible in the middle distillate cut. The fraction of branched

paraffins in the wax cut reaches about 22 [%] on average and slightly decreases with increasing recycle ratio. This is due to the aforementioned increase of H₂/wax ratio when recycle is raised. Higher values for this ratio imply higher hydro-cracking activity for catalysts in the hydro-cracking reactor, improving the branched species production.

[APPENDIX] Fortran User Subroutine

A *Fortran user model* is a subroutine written by user that can be used in sizing, costing and unit operation models (reactor models) [ASPEN User Models, v7.0].

A *subroutine (procedura)* is a sub - program like a *function*, but it is different from the latest for a series of characteristics, such as the possibility to manipulate more parameters of different type: IN, OUT, INOUT, besides the clear advantage to have more than one OUT variables:

<i>Function</i> :	<i>fun-name (formal parameters)</i>	{address - OUT} {IN}
<i>Sub-routine</i> :	<i>sub-name (formal parameters)</i>	{address} {IN,OUT,INOUT}

A.1 Installation pathway

To write and use any Fortran user subroutine 3 steps are required:

- Install Microsoft Visual Studio (2013/Community) as integrated develop ambient to *write* the Fortran code;
- Install Intel Fortran Compiler (INTEL PARALLEL STUDIO XE 2015 UPDATE 6 / Cluster edition for Windows) to *compile* the Fortran code;
- Matching Microsoft Visual Studio and Fortran compiler (through ASPEN Plus *Set Compiler for ver.*).

A summary of the couples of VS any IF versions that can be used they can be found under *Start/AspenProperties8.8*. Once a matching couple has been successfully installed "OK" will appear instead of "ERROR" in the *State* column of the corresponding line. It' s necessary to select the same combination for both USER (pc) and MACHINE (Aspen Simulation Engine).

```

Set Compiler for V10
6 IVF10_V$71 ERROR Intel Fortran 10.x and Microsoft Visual Studio .NET 2003
7 IVF10_V$8 ERROR Intel Fortran 10.x and Microsoft Visual Studio 2005
8 IVF10_V$9 ERROR Intel Fortran 10.x and Microsoft Visual Studio 2008
9 IVF10_VCX8 ERROR Intel Fortran 10.x and Microsoft VC++ 2005 Express
10 IVF10_VCX9 ERROR Intel Fortran 10.x and Microsoft VC++ 2008 Express
11 IVF11_V$71 ERROR Intel Fortran 11.0 and Microsoft Visual Studio .NET 2003
12 IVF11_V$8 ERROR Intel Fortran 11.0 and Microsoft Visual Studio 2005
13 IVF11_V$9 ERROR Intel Fortran 11.0 and Microsoft Visual Studio 2008
14 IVF11_VCX8 ERROR Intel Fortran 11.0 and Microsoft VC++ 2005 Express
15 IVF11_VCX9 ERROR Intel Fortran 11.0 and Microsoft VC++ 2008 Express
16 IVF11X_V$71 ERROR Intel Fortran 11.x and Microsoft Visual Studio .NET 2003
17 IVF11X_V$8 ERROR Intel Fortran 11.x and Microsoft Visual Studio 2005
18 IVF11X_V$9 ERROR Intel Fortran 11.x and Microsoft Visual Studio 2008
19 IVF11X_V$B ERROR Intel Fortran 11.x and Bundled VS 2008 Shell ONLY
20 IVF11X_VCX8 ERROR Intel Fortran 11.x and Microsoft VC++ 2005 Express
21 IVF11X_VCX9 ERROR Intel Fortran 11.x and Microsoft VC++ 2008 Express
22 IVF12X_V$9 ERROR Intel Fortran 12.x/2011 and Microsoft Visual Studio 2008
23 IVF12X_V$10 ERROR Intel Fortran 12.x/2011 and Microsoft Visual Studio 2010
24 IVF12X_V$B ERROR Intel Fortran 12.x/2011 and Bundled VS 2008 Shell ONLY
25 IVF12X_V$B2 ERROR Intel Fortran 12.x/2011 and Bundled VS 2010 Shell ONLY
26 IVF12X_VCX10 ERROR Intel Fortran 12.x/2011 and Microsoft VC++ 2010 Express
27 IVF13_V$B ERROR Intel Fortran 13/2013 and Bundled VS 2010 Shell ONLY
28 IVF13_V$10 ERROR Intel Fortran 13/2013 and Microsoft Visual Studio 2010
29 IVF13_VCX10 ERROR Intel Fortran 13/2013 and Microsoft VC++ 2010 Express
30 IVF13_VCX11 ERROR Intel Fortran 13/2013 and VS Express 2012 for Win Desktop
31 IVF13_V$11 ERROR Intel Fortran 13/2013 and Microsoft Visual Studio 11/2012
32 IVF13_V$12 ERROR Intel Fortran 13/2013 and Microsoft Visual Studio 12/2013
33 IVF14_V$9 ERROR Intel Fortran 2013SP1 and Bundled VS 2010 Shell ONLY
34 IVF14_VCX11 ERROR Intel Fortran 2013SP1 and VS Express 2012 for Win Desktop
35 IVF14_VCX12 ERROR Intel Fortran 2013SP1 and VS Express 2013 for Win Desktop
36 IVF14_V$11 ERROR Intel Fortran 2013SP1 and Microsoft Visual Studio 11/2012
37 IVF14_V$12 ERROR Intel Fortran 2013SP1 and Microsoft Visual Studio 12/2013
38 IVF15_VCX12 ERROR Intel Fortran 15/2015 and VS Express 2013 for Win Desktop
39 IVF15_V$10 ERROR Intel Fortran 15/2015 and Microsoft Visual Studio 10/2010
40 IVF15_V$11 ERROR Intel Fortran 15/2015 and Microsoft Visual Studio 11/2012
41 IVF15_V$12 OK Intel Fortran 15/2015 and Microsoft Visual Studio 12/2013
42 IVF16_V$12 ERROR Intel Fortran 16/2016 and Microsoft Visual Studio 12/2013
43 IVF16_VCX14 ERROR Intel Fortran 16/2016 and VS Express 14/2015 WITH C++
44 IVF16_V$14 ERROR Intel Fortran 16/2016 and Visual Studio 14/2015 WITH C++
45 IVF17_V$12 ERROR Intel Fortran 17/2017 and Microsoft Visual Studio 12/2013
46 IVF17_VCX14 ERROR Intel Fortran 17/2017 and VS Express 14/2015 WITH C++
47 IVF17_V$14 ERROR Intel Fortran 17/2017 and Visual Studio 14/2015 WITH C++

The current compiler option settings in order of searching
 IVF15_V$12 for current user in HKEY_CURRENT_USER registry
 Not set for current machine in HKEY_LOCAL_MACHINE registry
 IVF14_V$12 in file C:\Program Files (x86)\AspenTech\APRSystem V10.0\Engine\xeq\Compilers.cfg

Enter option (1:47) for current USER, 0 to skip, -1 to delete: 41_

```

Figure A.4. Set Compiler for v10.

A.2 Code development

Since Aspen calculation system processes Fortran-based code programs to explicate its calculator function, the Fortran-based language should be preserved.

Therefore, the *formal parameters* Fortran-based language form of our subroutine has been kept out, starting the code development from one of the several *templates* available once ASPEN Plus has been installed.

For a kinetic user model to be implemented into the *Simulation Flow sheet / Reactions* form to be used into unit operation models (R-PLUG/RCSTR reactor model) the base file (*usrkin.for*) can be found under *Programs(x86) > Aspen tech > Aspen Plus ver. > Engine > User*.

Black bold: OUT

Orange: IN/OUT

Black light: IN

```

SUBROUTINE SUB-NAME (SOUT, NSUBS, IDXSUB, ITYPE, NINT,
2      INT, NREAL, REAL, IDS, NPO,
3      NBOPST, NIWORK, IWORK, NWORK, WORK,
4      NC, NR, STOIC, RATES, FLUXM,
5      FLUXS, XCURR, NTCAT, RATCAT, NTSSAT,
6      RATSSA, KCALL, KFAIL, KFLASH, NCOMP,
7      IDX, Y, X, X1, X2,
8      NRALL, RATALL, NUSERV, USERV, NINTR,
9      INTR, NREALR, REALR, NIWR, IWR,
*      NWR, WR, NRL, RATEL, NRV,
1     RATEV)

```

The output of kinetic sub-routine is the rate of generation (RATES) for each component in each sub-stream; for our purposes, one *mixed* type sub-stream only enters as feed and exits as product through R-plug type reactors (number - NSUBS, order - IDXSUBS and type - ITYPE of each sub-stream making up the stream defines the *Stream Class*, which the stream belongs to); the streams of our concern in this study belong to the so called *Conventional* Stream Class, because sub-stream number is 1 and the allowable sub-stream type is the *Mixed* one only [ASPEN User Models, v7.0].

In order to access specific information from ASPEN Plus simulation concerning the unit operation model design parameters (DIAM, LENGHT, CATMASS) or operation ones (P, T), or to access simulation data of all components (such as activity and/or fugacity coefficient) there are *common blocks*, under *Programs(x86) > Aspen tech > Aspen Plus ver. > Engine > Commons* (such as [rplg_rplugi.cmn](#) and [rplg_rplugr.cmn](#) for design and [rxn_rprops.cmn](#) for operation parameters, and [dms_plex.cmn](#) for all component data in the simulation) [ASPEN User Models, v7.0].

The Plex is the main memory area where all data for a simulation are stored and consists of data areas (integer and real arrays equivalence to each other) sized to hold the amount of data in the simulation. To access these areas (arrays) the *name*, the *offset*, and the *structure* (*one-* or *two-* dimensional) of the area are necessary.

Alternatively, you can use Aspen Plus monitor routines, such as PPMON_FUGLY, to access simulation data, such as the liquid fugacity coefficient of all components in the mixture. The ASPEN Plus physical monitor routines are able to control calculations of the required properties, using the methods, models, data sets and model options identified by the

option set (*Property method*) pointers. To use the physical monitors it's needed to pass to the monitor the following information, through the monitor's argument list:

- State variables (temperature, pressure and composition) (T,P,X,Y,NCOMP)
- Calculation codes indicating the required properties. (KPHI)
- Physical property option set pointers. (NBOPST)

CALL PPMON_FUGLY (T,P,X,Y,NCOMP,IDX,NBOPST,KDIAG,KPHI,**PHI,DPHI,KER**)

Black bold: OUT

Black light: IN

The composition vectors (X - liquid, Y - vapor) must be supplied in *packed* form (in other words, the composition vectors have to contain only the components actually present at the reaction place). To do that, it has been called one of the several Aspen Plus *Utility Subroutines*, in detail a packing utilities:

CALL SHS_CPACK (SUBSTR,**NCOMP,IDX,X,FLOW**)

Black bold: OUT

Black light: IN

That supplies the *sequence number* (IDX) of each of the conventional components actually present (NCOMP) at the reaction place (with molar flow different from 0) among all the conventional components entered on the *Components / Specifications / Selection* sheet; for each of the components actually present (NCOMP) composition (X) and flow (FLOW) vectors (molar flow rate for each of the NCOMP components) are provided by SHS_CPACK [ASPEN User Models, v7.0].

Furthermore, it could be useful to identify some components among all of the conventional components entered on the *Components / Specifications / Selection* sheet; to do that, it has been used another ASPEN Plus *Utility Subroutine*, DMS_KCCIDC, that locates a component by its ID specified as string (i.e. arrays of character variables) [ASPEN User Models, v7.0].

A.3 Compiling and linking

The compiling process has the aim to check the correspondence between the user code developed in the Microsoft Visual Studio integrated develop environment and the ASPEN Plus source code language (Fortran- based) and provide debug function. The ASPEN Plus Simulation Engine needs the Fortran compiler developed by Intel to read and execute the user code.

To open the Aspen Simulation Engine command window (a sort of Command Prompt) the pathway is following:

```
Start > Programs(x86) > Aspen Tech > Process Modelling ver.> Aspen Plus ver. >
Customize Aspen Plus ver.
```

To open the Aspen Properties Calculation Window follow the pathway:

```
Start > Programs(x86) > Aspen Tech > Aspen Plus ver. > Customize Aspen Properties ver.
```

Both the command windows are equivalent to be used for compiling and linking.

To compile, first enter the working file directory `.cd` at which the user code `.for` or `.f` is located, then enter (Fig. A.3):

```
aspcomp name_of_file
```

At this time, all the after compiling codification error are shown in the screen. After being corrected in the Fortran file, the compiling procedure has to be repeated, until no error messages are shown, which means that compilation is successful.

This process generates an object file, (with the extension `.obj`), an organized machine code that allows the following linking process.

The linking process procedure starts creating a text file (`.txt` , `.dat`) by means text-file programs, such as *Notepad*, in which the direction where the object file is placed must be written. The file must be saved with the extension `.opt`. If this file is saved in the same folder than the object file, the complete address is unnecessary, and writing the name of the file is enough.

To perform the linking process (Fig. A.3), enter:

```
asmlink [dlopt name_of_object_file.opt] name_of_dll_file
```

A successful message will be shown in the Aspen Plus Simulation Engine window, and a .dll file will be generated at the working file directory.

At this point, an .opt file (object file, i.e. a compiled script) must be created following the same procedure than the compiling process, to provide Aspen with the location of the compiled script file. If the .opt and .dll files are in the same folder, writing only the name of .dll file is enough for Aspen to locate the subroutine file.

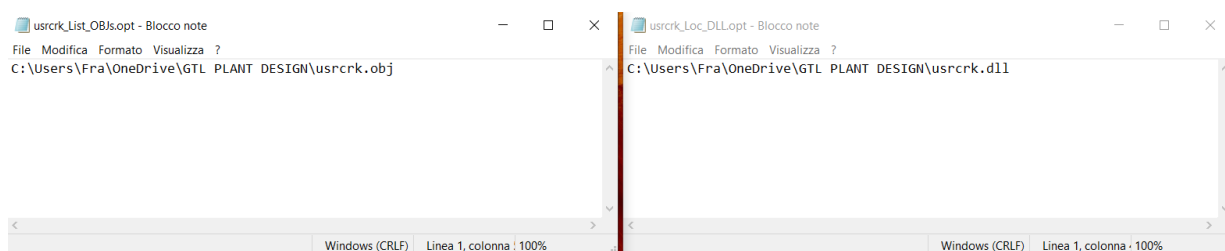


Figure A.5. Text files reporting location of .opt and .dll files

Finally, in the Aspen Plus simulation under *Run > Settings > Engine Files > Miscellaneous Files > Linker options*, the direction of the .opt file containing the location of the .dll file (Fig. A.2 on the right) must be given. Again only the name of the file must be written if .dll and the ASPEN .apw file are in the same directory.

At this time, enter the same name of the subroutine linked at the Reactions | Subroutine sheet and run to process the code into the current simulation.

Customize Aspen Plus V10

Welcome to Aspen Plus V10 Simulation Window.

```
C:\ProgramData\AspenTech\Aspen Plus V10.0>cd C:\Users\Fra\OneDrive\GTL PLANT DESIGN
```

```
C:\Users\Fra\OneDrive\GTL PLANT DESIGN>aspcomp uscrk
```

```
C:\Users\Fra\OneDrive\GTL PLANT DESIGN>asplink [dlopt uscrk_List_OBJS.opt] uscrk
```

```
Linking uscrk.dll; sending messages to uscrk.ld  
uscrk.dll created.
```

```
C:\Users\Fra\OneDrive\GTL PLANT DESIGN>
```

Figure A.6. Compiling and linking steps in the Aspen Plus Simulation Engine Window.

A.4 Fischer-Tropsch Fortran code

```

SUBROUTINE USRFT (SOUT,  NSUBS,  IDXSUB,  ITYPE,  NINT,
2          INT,  NREAL,  REAL,  IDS,  NPO,
3          NBOPST,  NIWORK,  IWORK,  NWORK,  WORK,
4          NC,  NR,  STOIC,  RATES,  FLUXM,
5          FLUXS,  XCURR,  NTCAT,  RATCAT,  NTSSAT,
6          RATSSA,  KCALL,  KFAIL,  KFLASH,  NCOMP,
7          IDX,  Y,  X,  X1,  X2,
8          NRALL,  RATALL,  NUSERV,  USERV,  NINTR,
9          INTR,  NREALR,  REALR,  NIWR,  IWR,
*          NWR,  WR,  NRL,  RATEL,  NRV,
1         RATEV)

C
C   IMPLICIT NONE
C
C   DECLARE VARIABLES USED IN DIMENSIONING
C
C   INTEGER NSUBS, NINT, NPO,  NIWORK, NWORK,
+       NC,  NR,  NTCAT, NTSSAT, NCOMP,
+       NRALL, NUSERV, NINTR, NREALR, NIWR,
+       NWR
C
C   DECLARE ARGUMENTS
C
C   INTEGER IDXSUB(NSUBS), ITYPE(NSUBS), INT(NINT),
+       IDS(2), NBOPST(6,NPO), IWORK(NIWORK),
+       IDX(NCOMP),  INTR(NINTR), IWR(NIWR),
+       NREAL, KCALL, KFAIL, KFLASH, NRL,
+       NRV
C   REAL*8 SOUT(1),  WORK(NWORK),
+       STOIC(NC,NSUBS,NR), RATES(NC),
+       FLUXM(1),  FLUXS(1),  RATCAT(NTCAT),
+       RATSSA(NTSSAT),  Y(NCOMP),
+       X(NCOMP),  X1(NCOMP),  X2(NCOMP)
C   REAL*8 RATALL(NRALL), USERV(NUSERV),
+       REALR(NREALR), WR(NWR),  RATEL(1),
+       RATEV(1),  XCURR
C
C   DECLARE LOCAL VARIABLES

C   INTEGER NCP, NCO
C   PARAMETER(NCP=70)
C   PARAMETER(NCO=40)
C   INTEGER IMISS, I, J, DMS_KCCIDC, ICO, IH2, IH20, ICO2,
+       IC_P(NCP), IC_O(NCO)
C   REAL*8 REAL(NREAL), RMISS, T, P,
+       VFRAC, BETA, VVAP, VLIQ, VLIQS
C   REAL*8 CATMASS, BED_VOID, XLEN, DIAM, AXCRD
C   REAL*8 K1, K2, K3, K4, k5, k5M, k60, k6E0, K7,
+       ALPHA(NCP), DE, ADSORP, ALPH, ALP, B(1),
+       ALPHTERM, AREA, CAT_RHO
C   REAL*8 PCO, PH2, PH20
C   REAL*8 KF_P(NCP), DRIVE_P,
+       KF_O(NCO), DRIVE_O
C
C INCLUDE COMMON BLOCKS

```

```

#include "ppexec_user.cmn"
    EQUIVALENCE (RMISS, USER_RUMISS)
    EQUIVALENCE (IMISS, USER_IUMISS)
#include "dms_plex.cmn"
    EQUIVALENCE (B(1), IB(1))
C
C..R-Plug reactor configuration features

#include "rplg_rplugr.cmn"
    EQUIVALENCE (CATMASS, RPLUGR_CATWT)
    EQUIVALENCE (BED_VOID, RPLUGR_BED_VOID)
    EQUIVALENCE (XLEN, RPLUGR_UXLONG)
    EQUIVALENCE (DIAM, RPLUGR_UDIAM)
    EQUIVALENCE (AXCRD, RPLUGR_AXPOS)
C
C.....Reactor (or pressure-relief vessel or stage) operation conditions...

#include "rxn_rprops.cmn"
    EQUIVALENCE (T, RPROPS_UTEMP)
    EQUIVALENCE (P, RPROPS_UPRES)
C
C BEGIN EXECUTABLE CODE
C
C Reactor section area and reactor catalyst density

AREA = (3.14D0/4.D0)*DIAM**2
CAT_RHO = CATMASS/(AREA*XLEN)
C
C Locate chemical component indexes (for FT reactant and products)
C on ASPEN Properties Components/Specifications/Sheet

ICO = DMS_KCCIDC('CO')
IH2 = DMS_KCCIDC('H2')
IH2O = DMS_KCCIDC('H2O')

IC_P(1) = DMS_KCCIDC('CH4')
IC_O(1) = 0
IC_P(2) = DMS_KCCIDC('C2H6')
IC_O(2) = DMS_KCCIDC('C2H4')
IC_P(3) = DMS_KCCIDC('C3H8')
IC_O(3) = DMS_KCCIDC('C3H6')
IC_P(4) = DMS_KCCIDC('C4H10')
IC_O(4) = DMS_KCCIDC('C4H8')
IC_P(5) = DMS_KCCIDC('C5H12')
IC_O(5) = DMS_KCCIDC('C5H10')
IC_P(6) = DMS_KCCIDC('C6H14')
IC_O(6) = DMS_KCCIDC('C6H12')
IC_P(7) = DMS_KCCIDC('C7H16')
IC_O(7) = DMS_KCCIDC('C7H14')
IC_P(8) = DMS_KCCIDC('C8H18')
IC_O(8) = DMS_KCCIDC('C8H16')
IC_P(9) = DMS_KCCIDC('C9H20')
IC_O(9) = DMS_KCCIDC('C9H18')
IC_P(10) = DMS_KCCIDC('C10H22')
IC_O(10) = DMS_KCCIDC('C10H20')
IC_P(11) = DMS_KCCIDC('C11H24')
IC_O(11) = DMS_KCCIDC('C11H22')
IC_P(12) = DMS_KCCIDC('C12H26')
IC_O(12) = DMS_KCCIDC('C12H24')

```

```

...
IC_P(40) = DMS_KCCIDC('C40H82')
IC_O(40) = DMS_KCCIDC('C40H80')
IC_P(41) = DMS_KCCIDC('C41H84')
IC_P(42) = DMS_KCCIDC('C42H86')
IC_P(43) = DMS_KCCIDC('C43H88')
IC_P(44) = DMS_KCCIDC('C44H90')
IC_P(45) = DMS_KCCIDC('C45H92')
IC_P(46) = DMS_KCCIDC('C46H94')

...
IC_P(68) = DMS_KCCIDC('C68H138')
IC_P(69) = DMS_KCCIDC('C69H140')
IC_P(70) = DMS_KCCIDC('C70H142')

C
C Kinetic and equilibrium (real) parameters from
C ASPEN Simulation Reactions/Subroutine sheet
C
k1 = REALR(1)*EXP(-REALR(2)/T/8314.472)
k2 = REALR(3)*EXP(-REALR(4)/T/8314.472)
k3 = REALR(5)*EXP(-REALR(6)/T/8314.472)
k4 = REALR(7)*EXP(-REALR(8)/T/8314.472)
k5 = REALR(9)*EXP(-REALR(10)/T/8314.472)
k5M = REALR(11)*EXP(-REALR(12)/T/8314.472)
k60 = REALR(13)*EXP(-REALR(14)/T/8314.472)
k6E0 = REALR(15)*EXP(-REALR(16)/T/8314.472)
k7 = REALR(17)*EXP(-REALR(18)/T/8314.472)
DE = REALR(19)

C
C Partial pressures used for computing chain growth probability (ALPHA)
C for each product component

PCO = Y(ICO)*P
PH2 = Y(IH2)*P
PH20 = Y(IH20)*P

C
C Chain growth probability for each hydrocarbon product molecule

ALPHA(1) = k1*PCO/(k1*PCO+k5M*PH2)
ALPHA(2) = k1*PCO/(k1*PCO+k5*PH2+k6E0*EXP(2*(-DE)/T/8314.472))
DO 100 I = 3, NCO
  ALPHA(I) = k1*PCO/(k1*PCO+k5*PH2+k60*EXP(I*(-DE)/T/8314.472))
100 CONTINUE

C
DO 150 I = NCO+1, NCP
  ALPHA(I) = k1*PCO/(k1*PCO+k5*PH2)
150 CONTINUE

C
C Adsorption term

ALPHTERM = 1
ALP = 1
DO 200 I = 1, NCP
  ALP = ALP*ALPHA(I)
  ALPHTERM = ALPHTERM + ALP
200 CONTINUE

C
+ ADSORP = 1+(K7*PH2)**0.5+((K7*PH2)**0.5)*(1+1/K4+1/(K3*K4*PH2)+
  PH20/(K2*K3*K4*PH2**2))*(ALPHTERM)

C
C Kinetic factor of each hydrocarbon product molecule

```

```

KF_P(1) = k5M*ALPHA(1)
KF_P(2) = k5*ALPHA(1)*ALPHA(2)
KF_O(1) = 0.D0
KF_O(2) = k6E0*EXP(2*(-DE)/T/8314.472)*ALPHA(1)*ALPHA(2)
ALPH = ALPHA(1)*ALPHA(2)
DO 300 I = 3, NCO
    ALPH = ALPH*ALPHA(I)
    KF_P(I) = k5*ALPH
    KF_O(I) = k60*EXP(I*(-DE)/T/8314.472)*ALPH
300 CONTINUE
DO 350 I = NCO+1, NCP
    ALPH = ALPH*ALPHA(I)
    KF_P(I) = k5*ALPH
350 CONTINUE
C
C   Driving force factor

DRIVE_P = (K7**0.5)*(PH2**1.5)
DRIVE_O = (K7*PH2)**0.5
C
C   Rate calculation for each hydrocarbon product component

DO 400 I = 1, NC
    RATES(I) = 0.D0
400 CONTINUE
DO 500 I = 1, NCP
    J = IC_P(I)
    RATES(J) = (KF_P(I)*DRIVE_P/ADSORP)*CAT_RHO*AREA
500 CONTINUE
DO 600 I = 2, NCO
    J = IC_O(I)
    RATES(J) = (KF_O(I)*DRIVE_O/ADSORP)*CAT_RHO*AREA
600 CONTINUE
C
C   Rate calculation for each reactant (CO and H2) and water

RATES(ICO) = 0
DO 700 I = 1, NCP
    RATES(ICO) = RATES(ICO) - I*RATES(IC_P(I))
700 CONTINUE
C
DO 750 I = 1, NCO
    RATES(ICO) = RATES(ICO) - I*RATES(IC_O(I))
750 CONTINUE
C
    RATES(IH2) = 0
DO 800 I = 1, NCP
    RATES(IH2) = RATES(IH2) - (2*I+1)*RATES(IC_P(I))
800 CONTINUE
C
DO 850 I = 1, NCO
    RATES(IH2) = RATES(IH2) - (2*I)*RATES(IC_O(I))
850 CONTINUE
C
RATES(IH2O) = - RATES(ICO)

END SUBROUTINE USRFT

```


A.5 Hydro-cracking Fortran code

```
C      User Kinetics Subroutine for RCSTR, RPLUG, RBATCH, PRES-RELIEF,
C      RADFRAC and RATEFRAC (USER type Reactions)
C
      SUBROUTINE USRCRK (SOUT,  NSUBS, IDXSUB,  ITYPE, NINT,
2         INT,  NREAL, REAL,  IDS,  NPO,
3         NBOPST, NIWORK, IWORK,  NWORK, WORK,
4         NC,  NR,  STOIC,  RATES, FLUXM,
5         FLUXS, XCURR, NTCAT,  RATCAT, NTSSAT,
6         RATSSA, KCALL, KFAIL,  KFLASH, NCOMP,
7         IDX,  Y,  X,  X1,  X2,
8         NRALL, RATALL, NUSERV,  USERV, NINTR,
9         INTR,  NREALR, REALR,  NIWR,  IWR,
*        NWR,  WR,  NRL,  RATEL, NRV,
1        RATEV)
C
C
      IMPLICIT NONE
C
      INCLUDE COMMON BLOCKS
C
#include "ppexec_user.cmn"
      EQUIVALENCE (RMISS, USER_RUMISS)
      EQUIVALENCE (IMISS, USER_IUMISS)
C
#include "dms_plex.cmn"
      EQUIVALENCE (B(1), IB(1))
C
C.....RPLUG...
#include "rplg_rplugr.cmn"
      EQUIVALENCE (CATMASS, RPLUGR_CATWT)
      EQUIVALENCE (BED_VOID, RPLUGR_BED_VOID)
      EQUIVALENCE (XLEN, RPLUGR_UXLONG)
      EQUIVALENCE (DIAM, RPLUGR_UDIAM)
C
C.....REACTOR (OR PRES-RELIEF VESSEL OR STAGE) PROPERTIES...
#include "rxn_rprops.cmn"
      EQUIVALENCE (T, RPROPS_UTEMP)
      EQUIVALENCE (P, RPROPS_UPRES)
      EQUIVALENCE (VFRAC, RPROPS_UVFRAC)
      EQUIVALENCE (BETA, RPROPS_UBETA)
      EQUIVALENCE (VVAP, RPROPS_UVVAP)
      EQUIVALENCE (VLIQ, RPROPS_UVLIQ)
      EQUIVALENCE (VLIQS, RPROPS_UVLIQS)
C
C
C      DECLARE VARIABLES USED IN DIMENSIONING
C
      INTEGER NSUBS, NINT, NREAL, NPO,  NIWORK, NWORK,
+         NC,  NR,  NTCAT, NTSSAT, NCOMP,
+         NRALL, NUSERV, NINTR, NREALR, NIWR,
+         NWR, NRV, NRL
C
C      DECLARE ARGUMENTS
C
      INTEGER IDXSUB(NSUBS), ITYPE(NSUBS), INT(NINT),
```

```

+      IDS(2), NBOPST(6,NPO), IWORK(NIWORK),
+      IDX(NCOMP), INTR(NINTR), IWR(NIWR),
+      KCALL, KFAIL, KFLASH
REAL*8 SOUT(1), WORK(NWORK), REAL(NREAL),
+      STOIC(NC,NSUBS,NR), RATES(NC),
+      FLUXM(1), FLUXS(1), RATCAT(NTCAT),
+      RATSSA(NTSSAT), Y(NCOMP),
+      X(NCOMP), X1(NCOMP), X2(NCOMP)
REAL*8 RATALL(NRALL), USERV(NUSERV),
+      REALR(NREALR), WR(NWR), RATEL(1),
+      RATEV(1), XCURR
C
C  DECLARE LOCAL VARIABLES
C
INTEGER IMISS, I, J, K, DMS_KCCIDC, IH2, IC02,
+      NCMIN, NCMINISO, NCMAX, L_GAMMA
REAL*8 RMIN, XMIN, Z1, Z2
PARAMETER(NCMIN=1)
PARAMETER(NCMINISO=4)
PARAMETER(NCMAX=70)
INTEGER INC(NCMAX), IISOC(NCMAX), TEMP, TEMP1, TEMP2, COMP,
+      COMP0, TEMP0, TEMP01, TEMP02
INTEGER KPHI, KDIAG, KER
REAL*8 RMISS, FLOW, B(1)
REAL*8 T, P, VFRAC, BETA, VVAP, VLIQ, VLIQS
REAL*8 DIAM, XLEN, BED_VOID, AXCRD, CATMASS
REAL*8 AREA, CAT_RHO
REAL*8 KISO(NCMAX), EISO(NCMAX), KEQ(NCMAX),
+      KLN(NCMAX), KLISO(NCMAX),
+      KF_ISO(NCMAX), DRIVE_ISO(NCMAX),
+      KCR(NCMAX), ECR(NCMAX),
+      KF_CR(NCMAX), DRIVE_CR(NCMAX),
+      RATE_ISO(NCMAX), RATE_CR(NCMAX),
+      ADSORP, DLOG, DEXP
REAL*8 PHIL(1), DPHIL(1), PHIV(1), DPHIV(1),
+      Z(1)
+      INTEGER KH, KS, KG, KV, KBASE
REAL*8 PHIP(1), DPHIP(1), H(1), DH(1), S(1), DS(1), G(1), DG(1),
+      V(1), DV(1), PHILL(1), DPHILL(1)
REAL*8 FUG(NC), ACT, FUG1(NC)
C
C  BEGIN EXECUTABLE CODE
C
C  Locate chemical component indexes (hydro-cracking reactants and products)
C  on ASPEN Properties Components/Specifications/Sheet

IH2 = DMS_KCCIDC('H2')

C  Alkane indexes

INC(1) = DMS_KCCIDC('CH4')
INC(2) = DMS_KCCIDC('C2H6')
INC(3) = DMS_KCCIDC('C3H8')
INC(4) = DMS_KCCIDC('C4H10')
INC(5) = DMS_KCCIDC('C5H12')
INC(6) = DMS_KCCIDC('C6H14')
INC(7) = DMS_KCCIDC('C7H16')
INC(8) = DMS_KCCIDC('C8H18')
INC(9) = DMS_KCCIDC('C9H20')
INC(10) = DMS_KCCIDC('C10H22')

```

```

INC(11) = DMS_KCCIDC('C11H24')
...
INC(68) = DMS_KCCIDC('C68H138')
INC(69) = DMS_KCCIDC('C69H140')
INC(70) = DMS_KCCIDC('C70H142')

C   Iso-alkanes indexes (starting from iso-butane 'ISO-C4')

DO 10 I=1,NCMINISO-1
    IISOC(I) = 0
10 CONTINUE

IISOC(4) = DMS_KCCIDC('ISO-C4')
IISOC(5) = DMS_KCCIDC('ISO-C5')
IISOC(6) = DMS_KCCIDC('ISO-C6')
IISOC(7) = DMS_KCCIDC('ISO-C7')
IISOC(8) = DMS_KCCIDC('ISO-C8')
IISOC(9) = DMS_KCCIDC('ISO-C9')
IISOC(10) = DMS_KCCIDC('ISO-C10')
IISOC(11) = DMS_KCCIDC('ISO-C11')
...
IISOC(67) = DMS_KCCIDC('ISO-C67')
IISOC(68) = DMS_KCCIDC('ISO-C68')
IISOC(69) = DMS_KCCIDC('ISO-C69')
IISOC(70) = DMS_KCCIDC('ISO-C70')
ICO2 = DMS_KCCIDC('CO2')

C
C   Initialize fugacity and reaction rate vectors

DO 30 I = 1, NC
    FUG(I) = 0.D0
    RATES(I) = 0.D0
30 CONTINUE

DO 35 I=1,NCMAX
    RATE_CR(I) = 0.D0
    RATE_ISO(I) = 0.D0
35 CONTINUE

C   Call SHS_PACK (utility subroutine) for identifying the components actually
    present (for which flow rate is different from zero)

CALL SHS_CPACK(SOUT,NCOMP,IDX,Z,FLOW)

C
C   Call PPMON_FUGLY (physical property monitor) for calculating fugacity
coefficient
C   for each component in the mixture

KDIAG = 4
KPHI = 1
CALL PPMON_FUGLY(T,P,X,Y,NCOMP,IDX,NBOPST,KDIAG,KPHI,PHIL,DPHIL,
+               KER)

C   Calculate fugacity for each component in the mixture

COMP = 0
DO 50 I = 1,NCOMP
    COMP = IDX(I)
    TEMP = 0
    TEMP1 = 0

```

```

TEMP2 = 0
IF (COMP.EQ.IH2) THEN
  FUG(COMP) = PHIL(I)*X(I)*P
ENDIF
J = 0
DO 60 J = NCMIN,NCMINISO-1
  TEMP = INC(J)
  IF (COMP.EQ.TEMP) THEN
    FUG(COMP) = PHIL(I)*X(I)*P
  ENDIF
60 CONTINUE
J = 0
DO 70 J = NCMINISO,NCMAX
  TEMP1 = INC(J)
  TEMP2 = IISOC(J)
  IF ((COMP.EQ.TEMP1).OR.(COMP.EQ.TEMP2)) THEN
    FUG(COMP) = PHIL(I)*X(I)*P
  ENDIF
70 CONTINUE
50 CONTINUE
C
C Reactor section area and reactor catalyst density

AREA = (3.14D0/4.D0)*DIAM**2
CAT_RHO = CATMASS/(AREA*XLEN)
C
C Kinetic and equilibrium parameters as function of carbon number

DO 80 I = NCMIN,NCMINISO
  KISO(I) = 0.D0
  EISO(I) = 0.D0
  KEQ(I) = 0.D0
  KCR(I) = 0.D0
  ECR(I) = 0.D0
  KLN(I) = 10.3D0*EXP(0.4D0*I)
  KLISO(I) = 0.D0
80 CONTINUE
I = NCMINISO
KISO(I) = 3.88D0*(I**7.7D0)*1.D17/3.6D3
EISO(I) = 1.D3*((2.23D0*LOG(1.D0*I))*1.D4+1.2D5)
KLISO(I) = 20.D0*EXP(0.1D0*I)
KEQ(I) = 1.24D0*I**2-1.15D0*I*1.D-2+5.2D3

DO 90 I = NCMINISO+1,NCMAX
  KISO(I) = 3.88D0*(I**7.7D0)*1.D17/3.6D3
  EISO(I) = 1.D3*((2.23D0*LOG(1.D0*I))*1.D4+1.2D5)
  KEQ(I) = 1.24D0*I**2-1.15D0*I*1.D-2+5.2D3
  KCR(I) = 1.52D0*(I**7.63D0)*1.D16/3.6D3
  ECR(I) = (3.06D0*LOG(1.D0*I)+8.75)*1.D4*1.D3
  KLN(I) = 10.3D0*EXP(0.4D0*I)
  KLISO(I) = 20.D0*EXP(0.1D0*I)
90 CONTINUE
C
C Adsorption term

ADSORP = 1
DO 100 I = NCMIN,NCMINISO-1
  ADSORP = ADSORP + KLN(I)*FUG(INC(I))
100 CONTINUE
DO 110 I = NCMINISO,NCMAX

```

```

        ADSORP = ADSORP + KLN(I)*FUG(INC(I)) + KLISO(I)*FUG(IISOC(I))
110 CONTINUE
        ADSORP = FUG(IH2)*ADSORP
C
C      Kinetic factor and driving force for n-alkanes and iso-alkanes

        DO 120 I = NCMIN,NCMINISO
            KF_ISO(I) = 0.D0
            DRIVE_ISO(I) = 0.D0
            KF_CR(I) = 0.D0
            DRIVE_CR(I) = 0.D0
120 CONTINUE
        KF_ISO(4) = KISO(4)*EXP(-EISO(4)/T/8314.472)
        DRIVE_ISO(4) = FUG(INC(4))-FUG(IISOC(4))/KEQ(4)
        DO 130 I = NCMINISO+1,NCMAX
            KF_ISO(I) = KISO(I)*EXP(-EISO(I)/T/8314.472)
            DRIVE_ISO(I) = FUG(INC(I))-FUG(IISOC(I))/KEQ(I)
            KF_CR(I) = KCR(I)*EXP(-ECR(I)/T/8314.472)
            DRIVE_CR(I) = FUG(IISOC(I))
130 CONTINUE
C
C      Isomerization rate for n-alkanes (paraffins) and cracking rate for iso-alkanes

        DO 140 I = NCMINISO, NCMAX
            RATE_ISO(I) = (KF_ISO(I)*DRIVE_ISO(I)/ADSORP)*CAT_RHO*AREA
            RATE_CR(I) = (KF_CR(I)*DRIVE_CR(I)/ADSORP)*CAT_RHO*AREA
140 CONTINUE
C
C      Paraffin reaction rates

        DO 150 I = NCMIN, NCMINISO
            J = INC(I)
            RATES(J) = 0.5*RATE_CR(5)
150 CONTINUE
        RATES(INC(3)) = RATES(INC(3)) + 2*RATE_CR(6) + RATE_CR(7)

        DO 160 I = NCMINISO,NCMAX
            J = INC(I)
            RATES(J) = RATES(J) - RATE_ISO(I)
160 CONTINUE
C      Iso-alkane reaction rates

        RATES(IISOC(4)) = RATE_ISO(4) + 2*RATE_CR(8)
1      + RATE_CR(9) + RATE_CR(7)
        DO 170 I = NCMINISO+1,NCMAX
            J = IISOC(I)
            IF(I.LT.NCMAX/2) THEN
                RATES(J) = RATE_ISO(I) - RATE_CR(I) + 2*RATE_CR(2*I)
1      + RATE_CR(2*I-1) + RATE_CR(2*I+1)
            ELSEIF(I.EQ.NCMAX/2) THEN
                RATES(J) = RATE_ISO(I) - RATE_CR(I) + 2*RATE_CR(2*I)
1      + RATE_CR(2*I-1)
            ELSEIF(I.GT.NCMAX/2) THEN
                RATES(J) = RATE_ISO(I) - RATE_CR(I)
            ENDIF
170 CONTINUE
C      Reaction rate for hydrogen

```

```
RATES(IH2) = 0.D0
DO 180 I = NCMINISO+1, NCMAX
  RATES(IH2) = RATES(IH2) - RATE_CR(I)
180 CONTINUE
C
  END SUBROUTINE USRCRK
```

REFERENCES

PAR. 1

- *IPCC*, 2001: Climate Change 2001: Mitigation, Contribution of Working Group III to the Third Assessment Report of the Intergovernmental Panel on Climate Change, Cambridge University Press, Cambridge, UK. 752 pp, ISBN: 0521015022.
- *IPCC*, 2000: Emissions Scenarios, a Special Report of IPCC Working Party III, Summary for Policy Makers, 20 pp.
- *IPCC*, 2004: Special Report on Carbon dioxide Capture and Storage, Sources of CO₂, 104 pp.
- *IPCC*, 2018: Special Report on the impacts of global warming of 1.5 °C , Summary for Policy Makers, 32 pp.
- *IEA GHG*, 2000b: Greenhouse Gas Emissions from Major Industrial Sources - III, Iron and Steel Production, PH3/30, September, 130 pp.
- *IEA GHG*, 2002a: Building the Cost Curves for CO₂ Storage, Part 1: Sources of CO₂, PH4/9, July, 48 pp.
- *IEA GHG*, 2002b: Opportunities for Early Application of CO₂ Sequestration Technology, Ph4/10, September, 91 pp.

PAR. 2

- de Klerk A., Synthetic Liquids Production and Refining. *ACS Symposium Series*, 2011a; 1084; 215-235.
- Bourbonneux G., "Production d' hydrogène" in "Procédés de transformation" from P. Leprince, Technip, 1998.
- Gall D., Gibson E.J., Hall C.C., *Journal of Applied Chemistry*, 1952; 2(7); 371-380.
- Suppes G.J., Terry J.G., Burkhart M.L., Cupps M.P., Compression-ignition fuel properties of Fischer-Tropsch syncrude. *Ind. Eng. Chem. Res.*, 1998; 37; 2029–2038.

- Calemma V., Gambaro C., Parker Jr W.O., Carbone R., Giardino R., Scorletti P., *Catalysis Today*, 2010; 149; 40–46
- de Klerk A., Fischer-Tropsch Refining. Weinheim: *Wiley-VCH Verlag*, 2011.
- Baird M.J., Schehl R.R., Haynes W.P., F-T processes investigated at the Pittsburgh Energy Technology Center since 1944, *Ind. Engng. Chem. Prod. Res. Dev.*, 1980; 19; 175-191.
- Nawaz Z., Naveed S., Ahmed R.S., Nawaz S., Liquid Fuels and Hydrocarbons from Coal “Innovative way to future energy frontiers” , 5th International Multidisciplinary Conference (by Science International), at Lahore, 2015; 5; 1-35.
- Dry M.E., in *Catalysis Science and Technology*, J.R. Anderson and M. Boudart (eds.), Springer Verlag, 1981; 1; 159.
- M.E. Dry, *Applied Catalysis A: Gen.*, 1996; 138; 319.
- Dry, M. E., High quality Diesel via the Fischer-Tropsch Process - a Review. *Journal of Chemical Technology and Biotechnology*, 2001; 77; 43-50.
- Dry M. E., Fischer-Tropsch Synthesis - Industrial. In: I. T. Horváth, ed. Encyclopedia of catalysis. Hoboken, N.J: Wiley-Interscience, 2010.
- Khodakov A.Y., Chu W., Fongarland P., *Chemical Reviews*, 2007; 107; 1692.
- De Klerk A., Fischer-Tropsch process, *Kirk-Othmer Encyclopedia of Chemical Technology*. Copyright John Wiley & Sons, 2013; 25;
- Krishna R., De Swart J. W., Ellenberger J., Martina G. B., Maretto C. , Gas holdup in slurry bubble columns: Effect of column diameter and slurry concentrations. *AIChE J.*, 1997; 43; 311-316.
- Paturzo L., Basile A., Drioli E., High temperature membrane reactors and integrated membrane operations. *Rev Chem Eng* 2002; 18; 511.
- Moulijn J.A., Kreutzer M.T., Nijhuis T.A., Kapteijn F., *Advances in Catalysis*, 2011; 54; 249.
- Kreutzer M.T., Kapteijn F., Moulijn J.A., Heiszwolf J.J., *Chemical Engineering Science*, 2005; 60; 5895.
- Guettel R., Turek T., Comparison of different reactor types for low temperature Fischer-Tropsch synthesis: a simulation study. *Chem Eng Sci*, 2009; 64; 955–964.
- Saeidi S., Nikoo M., Mirvakili A., Recent advances in reactors for low-temperature Fischer-Tropsch synthesis: process intensification perspective. *Reviews in Chemical Engineering*, 2005; 31(3); 209-238.
- Wang Y., VanderWiel D.P., Tonkovich A.L.Y., Gao Y., Baker E.G., US Patent, 6558634 B1, 2003.

- Jarosch K., Leviness S., Tonkovich L. A., Fitzgerald S., Yang B., Mcdaniel J., Improved Fischer-Tropsch Economics Enabled by Microchannel Technology, 2011.
- Chambrey S., Fongarland P., Karaca H., Piche S., Griboval-Constant A., Schweich D., Luck F., Savin S., Khodakov A.Y., *Catalysis Today*, 2011; 171; 201.
- Knochen J., Guettel R., Knobloch C., Turek T., *Chemical Engineering and Processing*, 2010; 49; 958.

PAR. 3

- Sie S., Krishna R., Fundamentals and selection of advanced Fischer-Tropsch reactors. *Applied Catalysis A: General*, 1999; 186; 55-70.
- Maitlis P. M., de Klerk A., Greener Fischer-Tropsch Processes for Fuels and Feedstocks. *Weinheim: Wiley-VCH Verlag*, 2013.
- Maitlis P. M., Zanotti V., *Chem. Commun.*, 2009, 1619–1634.
- Dry M.E., *Journal of Molecular Catalysis*, 1982; 17; 133.
- Dry, M. E., Chapter 3 - Chemical concepts used for engineering purposes. In: A. Steynberg, M. E. Dry, Fischer-Tropsch Technology. *Amsterdam: Elsevier*, 2004.
- Steynberg A., Dry M. E., Davis B. H., Breman B. B., Chapter 2 - Fischer-Tropsch Reactors. In: A. Steynberg & M. E. Dry, eds. Fischer-Tropsch Technology. *Amsterdam: Elsevier*, 2004.
- Dry M.E., *Fischer Tropsch synthesis over iron catalysts*, 1990; 7(1-4); 241-251.
- De Smith E., Weckhuysen B.M., *Chem. Soc. Rev.*, 2008; 37; 2758-2781.
- Van de Loodstrecht J., Botes F.G., Ciobica I.M., Ferreira A., Gibson P., Moodley D.G., Saib A.M., Visagie J.L., Weststrate C.J., Niemantsverdriet J.V. (Hans), *Fischer-Tropsch synthesis: Catalysts and Chemistry*, 2013; Cap. 7.20; 522-554.
- Steynberg A.P., *Introduction to Fischer-Tropsch technology*, 2004; 152; 1-63;
- Dry E.M., Hoogendoorn J.C., *Catal. Rev.*, 1981; 23; 265-278.
- Davis B.H., *Chem. Today*, 2003; 84(1-2); 83-98.
- Bromfield, T. C.; Visagie, R. Chromium Oxide Incorporation into Precipitated Iron-Based Fischer-Tropsch Catalysts for Increased Production of Oxygenates and Branched Hydrocarbons. Patent WO 2005049765A1, 2005.
- Diehl F., Khodakov A. Y., *Oil Gas Sci. Technol.*, 2009; 64; 11–24.
- Bezemer G. L., Bitter J. H., Kuipers H., Oosterbeek H., Holewijn J. E., Xu X. D., Kapteijn F., van Dillen A. J., de Jong K. P. J., *Am. Chem. Soc.*, 2006; 128; 3956–3964.

- Rytter E., Skagseth T. H., Eri S., Sjastad A. O., *Ind. Eng. Chem. Res.*, 2010; 49; 4140–4148.
- Feller A., Claeys M., van Steen E. J., *Catal.*, 1999; 185; 120–130.
- Tan K. F., Chang J., Borgna A., Saeys M. J., *Catal.*, 2011; 280; 50–59.
- Khodakov A. Y., Chu W., Fongarland P., *Chem. Rev.*, 2007; 107; 1692–1744.
- Beuther H., Kobylinski T. P., Kibby C. L., Pannell R. B., *Synthesis Gas Conversion Using Ruthenium-Promoted Cobalt Catalyst Prepared by Non-aqueous Impregnation*. US Patent 4585798A, 1986.
- Xiong H. F., Motchelaho M. A. M., Moyo M., Jewell, L. L., Coville N. J. J., *Catal.*, 2011; 278; 26–40.
- Saib A. M., Borgna A., de Loosdrecht J. V., van Berge P. J., Niemantsverdriet J. W., *Appl. Catal. A: Gen.* 2006; 312; 12–19.
- Iglesia E., Soled S. L., Fiato R. A., Via G. H. J., *Catal.*, 1993; 143; 345–368.
- Leviness S. C., Mart C. J., Behrmann W. C., Hsia S. J., Neskora D. R., *Slurry Hydrocarbon Synthesis Process with Increased Catalyst Life*. Patent WO 9850487A1, 1998.
- H. A. J. van Dijk, *The Fischer–Tropsch synthesis: A mechanistic study using transient isotopic tracing*, Ph.D Thesis, Technische Universiteit Eindhoven, Eindhoven, 2001.
- F. G. Botes, *Energy Fuels*, 2007; 21; 1379–1389.
- J. Gaube and H. F. Klein, *Appl. Catal., A*, 2010; 374(1–2); 120–125.
- Novak S., Madon R.J., Suhl H., *Journal of Catalysis*, 1982; 77; 141.
- Kuipers E.W., Scheper C., Wilson J.H., Vinkenburg I.H., Oosterbeek H., *Journal of Catalysis*, 1996; 158; 288.
- Iglesia E., Reyes S.C., Madon R.J., *Journal of Catalysis*, 1991; 129; 238.
- Iglesia E., Soled S.L., Fiato R.A., Via G.H., *J. Catal.*, 1993; 143; 345–368.
- Masuku C. M., Shafer W. D., Ma W., Gnanamani M. K., Jacobs G., Hildebrandt D., Glasser D., B. H. Davis, *Journal of Catalysis*, 2012; 287; 93–101.
- van der Laan G.P., Beenackers A.A.C.M., *Industrial & Engineering Chemistry Research*, 1999; 38; 1277.
- Kuipers E.W., Vinkenburg I.H., Oosterbeek H., *Journal of Catalysis*, 1995; 152; 137.
- Botes F. G., *Kinetic and Selectivity Modelling of the Iron-Based Low-Temperature Fischer–Tropsch Synthesis*, PhD Thesis, Technische Universiteit Eindhoven, 2008.
- James O.O., Chowdhury B., Mesubi M.A., Maity S., *RSC Advances*, 2012; 2; 7347–7366.
- Susu A. A., *Chemical kinetics and heterogeneous catalysis*, CJC Press, Lagos, 1997.

- Cheng J., Hu P., Ellis P., French S., Kelly G., Lok C. M., *J. Phys. Chem. C*, 2008; 112; 6082–6086.
- Storsæter S., Chen D., Holmen A., *Surface Science*, 2006; 600; 2051.
- Shi B., Davis B.H., *Applied Catalysis A: General*, 2004; 277; 61.
- Maitlis P.M., Quyoum R., Long H.C., M.L. Turner, *Applied Catalysis A: General*, 1999; 186; 363.
- Ciob|ca I.M., *The Molecular Basis of the Fischer Tropsch Reaction*, Ph.D Thesis, Technische Universiteit Eindhoven, 2002.
- Storch H.H., Golubic N., Anderson R.B., *The Fischer-Tropsch and Related Syntheses*, John Wiley & Sons, New York, 1951.
- Pichler H., Schulz H., *Chemie Ingenieur Technik*, 1970; 42; 1162.
- Zhuo M., Tan K.F., Borgna A., Saeys M., *The Journal of Physical Chemistry C*, 2009; 113; 8357.
- Yates I.C., Satterfield C.N., *Energy & Fuels*, 1992; 6; 308.
- Lögberg S., Lualdi M., Järås S., Walmsley J.C., Blekkan E.A., Rytter E., Holmen A., *Journal of Catalysis*, 2010; 274; 84.
- Olewski T., Todici B., Nowicki L., Nikacevic N., Bukur D. B., Hydrocarbon selectivity models for iron-based Fischer–Tropsch catalyst, *Chemical Engineering Research and Design*, 2015, 95, 1.
- Claeys M, Van Steen E, Basic Studies, *Stud. Surf. Sci. Catal.* 2004; 152; 601-680.
- 3.1-3.2: Fontenelle A, Fernandes FA, Comprehensive polymerization model for Fischer-Tropsch synthesis, *Chemical Engineering technology*, 2011; 34(6); 963-971.

CAP. 4

- Coonradt H. L., Garwood W. E., Mechanism of Hydrocracking. Reactions of Paraffins and Olefins. *Ind. Eng. Chem.*, 1964; 3; 38-45.
- Bouchy C., Hastoy G., Guillon E., Martens J. A., Fischer-Tropsch Waxes Upgrading via Hydrocracking and Selective Hydro-isomerization. *Oil and Gas Science and Technology Review*, 2009; 71; 227-241.
- Ndimande C., Ideal Hydrocracking Catalyst For The Conversion Of FT Waxes To Diesel, University of Cape Town, 2004.

- Calemma V., Gambaro C., Parker W. O., Carbone, R. Giardino R., Scorletti P., Middle Distillates from Hydrocracking of FT Waxes: Composition, Characteristics and Emissions. *Catalysis Today*, 2009; 149, 40-46.
- Dufresne P., Bigeard P. H., Billion A., New Developments in Hydrocracking: Low Pressure High-Conversion Hydrocracking. *Catalysis Today*, 1987; 1; 367-384.
- Eilers J., Posthuma S. A., Sie S. T., The Shell Middle Distillate Synthesis Process (SMDS). *Catalysis Letters*, 1990; 7; 253-270.
- Dry M. E., The Fischer-Tropsch process: 1950-2000. *Journal of Chemical Technology and Biotechnology*, 2002; 71; 227-241.
- Weisz P.B., Swegler E.W., Stepwise Reaction on Separate Catalytic Centers Isomerization of Saturated Hydrocarbons. *Science*, 1957; 126; 31-32.
- Mills G., Heinemann H., Milliken T., Oblad A., (Hydroforming Reactions) Catalytic Mechanism. *The Journal of Industrial and Engineering Chemistry*, 1953; 45; 134-137.
- Kumar H., Mechanistic Kinetic Modelling Of The Hydrocracking Of Complex Feedstocks, PhD Tesys, Texas A&M University, 2006; 11.
- Baltanas M.A., Vansina H., Froment G.F., Hydroisomerization and hydrocracking. 5. Kinetic analysis of rate data for n-octane. *Industrial & Engineering Chemistry Product Research and Development*, 1983; 22; 531-539.
- Scherzer J., Gruia A. J., Hydrocracking Science and Technology. Marcel Dekker, Inc.: New York, 1996.
- Guisnet, M.; Alvarez, F.; Giannetto, G.; Perot, G., Hydroisomerization and Hydrocracking of n-Heptane on the Zeolites. Effect of the Porosity and of the Distribution of Metallic and Acid Sites. *Catalysis Today*, 1987; 1; 415-426.
- Laxminarasimhan C. S., Verma R. P., Ramachandran P. A., Continuous lumping model for simulation of hydrocracking. *AIChE Journal*, 1996; 42 (9); 2645-2653.
- Baltanas M. A., Vanraemdonck K. K., Froment, G. F., Mohedas, S. R., Fundamental Kinetic Modeling of Hydroisomerization and Hydrocracking on Noble- Metal-Loaded. Rate Parameters for Hydroisomerization. *Industrial & Engineering Chemistry Research*, 1989; 28 (7); 899-910.
- Feng W., Vynckier E., Froment G. F., Single-Event Kinetics of Catalytic Cracking. *Industrial & Engineering Chemistry Research*, 1993; 32 (12); 2997-3005.
- Clymans P. J., Froment G. F., Computer-Generation of Reaction Paths and Rate-Equations in the Thermal-Cracking of Normal and Branched Paraffins. *Computers & Chemical Engineering*, 1984; 8 (2); 137-142.

- Martens G. G., Marin G. B., Martens J. A., Jacobs P. A., Baroni G. V., A Fundamental Kinetic Model for Hydrocracking of C-8 to C-12 Alkanes on Pt/US-Y Zeolites. *Journal of Catalysis*, 2000; 195 (2); 253-267.
- Pellegrini A., Gamba S., Calemma S., Bonomi S., Modelling of hydrocracking with vapour-liquid equilibria, *Chemical Engineering Science*, 2008; 63; 4285-4291.

CAP. 5

- ASPEN Physical Property Methods and Models, ver. 10.1-0.
- ASPEN Physical Property Data, ver. 10.1-0.
- ASPEN Plus v10 Help.
- ASPEN Plus User Models, ver. 7.0, 2008.
- Soave G., Equilibrium Constants for Modified Redlich-Kwong Equation-of-state, *Chem. Eng. Sci.*, 1972; 27; 1196 – 1203.
- Zwolinski B.J., Wilhoit R.C., Handbook of Vapor Pressures and Heats of Vaporization of Hydrocarbons and Related Compounds, API 44-TRC Publications in *Science and Eng., Thermodynamics Res. Center*, Dept. of Chemistry, Texas A&M University, College Station, TX, 1971.
- Marano J.J., Holder G.D., *Ind. Eng. Chem. Res.*, 1997; 36; 1895-1907.
- Kudchadker A.P., Zwolinski B.J., *J. Chem. Eng. Data*, 1966; 11; 253–255.
- Kreglewski A., Zwolinski B.J., *J. Phys. Chem.*, 1961; 65; 1050–1052.
- Flory P. J., Orwoll R. A., Vrij A., Statistical Thermodynamics of Chain Molecule Liquids. I. An Equation of State for normal Paraffin Hydrocarbons. *J. Am. Chem. Soc.*, 1964; 86; 3507-3514.
- Pellegrini L.A., Gamba S., Soave G.S., *Fluid Phase Equilibria*, 2009; 276; 133–141
- Soave G.S., *Fluid Phase Equilib.*, 1998; 143; 29–39.
- Kurata M., Isida S., Theory of Normal Paraffin Liquids. *J. Chem. Phys.* 1955; 23; 1126-1131.
- Sanchez I. C., Lacombe R. H., An Elementary Molecular Theory of Classical Fluids. Pure Fluids. *J. Phys. Chem.* 1976; 80; 2352-2362.
- Tsonopoulos C., Heidman J.L., High-pressure vapor–liquid equilibria with cubic equations of state. *Fluid Phase Equilibria*, 1986; 29; 391–414.
- Soave G., Pellegrini L.A., Gamba S., *Fluid Phase Equilibria*, 2010; 299; 285–293.
- Choudary V.R., Mondal K.C., *Applied Energy*, 2006; 83; 1024-1032.

- Lox E.S., Froment G.F., *Industrial & Engineering Chemistry Research*, 1993; 32; 71.
- Lox E.S., Froment G.F., *Industrial & Engineering Chemistry Research*, 1993; 32; 61.
- Selvatico D., Lanzini A., *Fuel*, 2016; 186; 544-560.
- Todic B., Ma W., Jacobs G., Davis B.H., Bukur D.B., *Catalysis Today*, 2014; 228; 32.
- Cheng J., Hu P., Ellis P., French S., Kelly G., Lok C.M., *Journal of Catalysis*, 2008; 257; 221.
- Cheng J., Song T., Hu P., Lok C.M., Ellis P., French S., *Journal of Catalysis*, 2008; 255; 20.
- Nguyen C.M., De Moor B.A., Reyniers M.F., Marin G.B., *The Journal of Physical Chemistry C*, 2011; 115; 23831.
- Pellegrini L.; Locatelli S.; Rasella S.; Bonomi S.; Calemma V., Modeling of Fischer-Tropsch Products Hydrocracking. *Chem. Eng. Sci.* 2004; 59; 4781.
- Pellegrini L.; Bonomi S.; Gamba S.; Calemma V.; Molinari, D. The "All Components Hydrocracking Model" . *Chem. Eng. Sci.* 2007a; 62; 5013-5020.
- Pellegrini L.; Bonomi S.; Gamba S.; Calemma V.; Molinari, D., Modelling of hydrocracking with vapour-liquid equilibrium. *Chem. Eng. Sci.* 2008; 63; 4285-4291.
- Froment G.F., Kinetics of the hydroisomerization and hydrocracking of paraffins on a platinum containing bifunctional Y-zeolite. *Catalysis Today*, 1987; 1; 455-473.
- Sie T.S., Acid-catalyzed cracking of paraffinic hydrocarbons. Evidence for the protonated cyclopropane mechanism from hydrocracking/hydroisomerization experiments. *Industrial & Engineering Chemistry Research*, 1993; 32; 403-408.
- Martens, J.A., Jacobs, P.A., Weitkamp, J., Attempts to rationalize the distribution of hydrocracked products. I. Qualitative description of the primary hydrocracking modes of long chain paraffins in open zeolites. *Applied Catalysis*, 1986; 20; 239-281.
- Reid R., Prausnitz J.M., Poling B.E., *The Properties Of Gas And Liquids*, McGraw-Hill, 1987.